Spring 2018

Non-Invasive Picosecond Pulse System for Electrostimulation

Ross Aaron Petrella
Old Dominion University, rpetr005@odu.edu

NON-INVASIVE PICOSECOND PULSE SYSTEM FOR ELECTROSTIMULATION

by

Ross Aaron Petrella
B.S. May 2014, Virginia Commonwealth University

A Dissertation Submitted to the Faculty of
Old Dominion University in Partial Fulfillment of the
Requirements for the Degree of

DOCTOR OF PHILOSOPHY

BIOMEDICAL ENGINEERING

OLD DOMINION UNIVERSITY
May 2018

Approved by:

Shu Xiao (Director)

Dean Krusienski (Member)

Shirshak Dhali (Member)

Patrick Sachs (Member)

ABSTRACT

NON-INVASIVE PICOSECOND PULSE SYSTEM FOR ELECTROSTIMULATION

Ross Aaron Petrella
Old Dominion University, 2018
Director: Dr. Shu Xiao

Picosecond pulsed electric fields have been shown to have stimulatory effects, such as calcium influx, activation of action potential, and membrane depolarization, on biological cells. Because the pulse duration is so short, it has been hypothesized that the pulses permeate a cell and can directly affect intracellular cell structures by bypassing the shielding of the membrane. This provides an opportunity for studying new biophysics. Furthermore, radiating picosecond pulses can be efficiently done by a compact antenna because the antenna size is comparable to the pulse width. However, all of the previous bioelectric studies regarding picosecond pulses have been conducted in vitro, using electrodes. There is not yet a device which can non-invasively deliver picosecond-pulsed electric fields to neurological tissue for therapeutic applications. It is unclear whether a radiated electric field at a given penetration depth can reach the threshold to cause biological effects.

In this dissertation, a picosecond- pulsed electric field system designed for the electrosimulation of neural cells is presented. This begins with the design of an ultra-wideband biconical dielectric rod antenna. It consists of a dielectrically loaded V-conical launcher which feeds a cylindrical waveguide. The waveguide then transitions into a taper, which acts like a lens to focus the energy in the tissue target. To describe the antenna delivery of picosecond pulses to tissues, the initial performance was simulated using a 3-layer tissue model and then a human head model. The final model was shown

to effectively deliver pulses of 11.5 V/m to the brain for a 1 V input. The spot size of the stimulation is on the order of 1 cm. The electric field was able to penetrate to a depth of 2 cm, which is equal to the pulse width of a 200 ps pulse. The antenna was constructed and characterized in free space in time domain and in frequency domain. The experimental results have a good agreement with the simulation.

The ultimate biological application relies on adequate electric field. To reach a threshold electric field for effective stimulation, the antenna should be driven by a high voltage, picosecond-pulsed power supply, which, in our case, consists of a nanosecond charging transformer, a parallel-plate transmission line, and a picosecond discharging switch. This transformer was used to charge a parallel-plate transmission line, with the antenna as the load. To generate pulses with a rise time of hundreds of picoseconds, an oil switch with a millimeter gap was used. For the charging, a dual resonance pulse transformer was designed and constructed. The novel aspect of this transformer is has a fast charge time. It was shown to be capable of producing over 100 kV voltages in less than 100 ns. After the closing of the peaking switch and the picosecond rise time generation, the antenna was able to create an electric field of 600 V/cm in the air at a distance of 3 cm. This field was comparable to the simulation. Higher voltage operation was met with dielectric breakdown across the insulation layer that separates the high voltage side and the ground side.

Before the designed antenna is used in vivo, it is critical to determine the biological effect of picosecond pulses. This is especially important if we focus on stimulatory effects, which require that the electric field intensity be close to the range that the antenna system can deliver. Toward that end, neural stem cells were chosen to study

for the proliferation, metabolism, and gene expression. Instead of using the antenna, the electrodes were used to deliver the pulses to the cells. In order to treat enough cells for downstream analyses, the electrodes were mounted on a 3-D printer head, which could be moved freely and could be controlled accurately by programming. The results show that pulses on the order of 20 kV/cm affect the proliferation, metabolism, and gene expression of both neural and mesenchymal stem cells, without reducing viability.

In general, we came to the conclusion that picosecond pulses can be a useful stimulus for a variety of applications, but the possibility of using antennas to directly stimulate tissue functions relies on the development of a pulsed power system, high voltage insulation, and antenna material.

This dissertation is dedicated to my parents Ralph and Laura Petrella.

ACKNOWLEDGMENTS

Along my journey, I have received help from many people whom I would like to personally acknowledge. First is my adviser, Dr. Shu Xiao. Thank you for your guidance, your instruction, and our many discussions. You have made my experience one of joy in discovery. I also extend my deepest appreciation to my committee members Dr. Dean Krusienski, Dr. Shirshak Dhali, and Dr. Patrick Sachs for sharing their insight and for their interest in my work.

Next, I would like to acknowledge my colleagues in the Pulse Power and Antenna Lab as well as in the Molecular Diagnostics Lab, especially Khiem Huynh, Dr. Peter Mollica, and Martina Zamponi. Thank you for your help over many long hours. Finally, I would like to thank all of those people who loved and supported me along the way. This includes Vance Petrella, Rebecca Petrella, and Shani Levit.

NOMENCLATURE

V	Electric Potential, V
I	Current, A
PEF	Pulsed Electric Field, (No Units)
psPEF	Picosecond Pulsed Electric Field, (No Units)
E	Electric Field, V/m
C	Capacitance, F
L	Inductance, H
k	Coupling Coefficient, (No Units)
ω	Angular Frequency, Rad/s
f	Frequency, Hz
λ	Wavelength, m
τ	Charge Time, s

TABLE OF CONTENTS

Page

LIST OF TABLES

Table Page

LIST OF FIGURES

CHAPTER 1

1. INTRODUCTION: FOUNDATIONS OF PICOSECOND ELECTRIC FIELDS

The biomedical applications of picosecond pulsed electric fields (psPEF) can be thought of as two related areas of study. First is the biological response to psPEF. The extent to which the pulses affect the cell depends on a number of parameters, including the pulse amplitude, the frequency, the repetition rate, and the cell type. As such, this is still an ongoing area of investigation.

The second area of study is in designing the psPEF delivery systems. Currently, all of the biological experiments are being been done in vitro, using electrodes, whereby the electric field intensity is determined by the electrode configuration. One of the novel aspects of psPEF is that they can potentially be delivered non-invasively in vivo using an antenna. To this end, reflector-type antennas, which focus in the near field, have been examined. As of yet, they have been unable to generate field strengths sufficient to induce biological effects.

This dissertation will address both aspects of picosecond-pulse electric fields. To explore the potential for non-invasive psPEF stimulation, a biconical dielectric rod antenna was designed and simulated by a time-domain electromagnetic solver. Next, it was constructed and characterized for the performance. To drive such an antenna will require the construction of a high-voltage pulsed power supply. For this, a dual resonance pulse transformer was designed and constructed. The novel aspect of this transformer design is the speed of the charging time, which allows for increased repetition rates as well as reduced insulation. In order to use the antenna for its designed purpose, the electric field at which psPEF are capable of stimulating intracellular changes in cells was studied. The changes in proliferation, metabolism, and gene expression of neural stem cells were assessed. Although this in vitro study was done with needle electrodes, it provides a case study for which the effective electric field was determined.

1.1 PICOSECOND PULSED ELECTRIC FIELD EFFECTS

Pulsed electric fields have been studied for their biological effects. Generally, these effects fall into one of three categories. The first is the charging of the cell membrane. Cell membranes have an inherent voltage potential; applying an external

electric field can modify that potential by accumulating charges across the cell membrane. The membrane on the cathode-facing side becomes depolarized, and the anode-facing side becomes hyperpolarized. This depolarization is the foundation for activating neural action potential, which can be caused even by nsPEF, as shown in the frog peripheral nerves [1]. The next effect that PEF can have on cells is that it directly affects charged molecules. The charges will align with the electric field direction and. if they are mobile enough, they will be pulled towards the electrode with a speed determined by the mobility and the electric field [2]. The third effect is a dielectrophoretic force that applies to the dipolar (or multipolar) structures when the electric field is nonuniform or when the dielectric properties of biomolecules are inhomogeneous. One well-studied effect caused by electrical pulsing, for example, is membrane permeabilization. This is a result both of membrane charging and of the reorientation of the polar heads of phospholipids, which can lead to membrane poration. There are two forms of electroporation. Reversible electropration is the formation of pores in the membrane which can close after pulsing. The viability of the cells is not adversely impacted. This has led to applications in drug [3] and gene delivery, which are preferable to viral delivery methods [4]. On the other hand, irreversible electroporation is designed to create permanent pores in the membrane that are large enough to kill the cell. This has been found application in cancer treatment [5] and in food processing [6]. The extent to which any of these three effects occurs is dependent on the strength, duration, and repetition of the pulsed electric field.

An emerging area in bioelectrics research is in picosecond-pulsed electric fields (psPEF). psPEF has the potential to be much different than previous pulsing regimes. According to a cell-circuit model, pulsed electric fields on the order of milliseconds or microseconds target a cell's outer membrane and exert little influence on the intracellular membranes and organelles. However, as the pulse duration decreases into the picosecond regime, the effects on the outer membrane are reduced and the effects on intracellular bodies and membranes ought to become more pronounced [7]. This is because the pulse rise time of the pulses is much faster than the charge time of the plasma membrane, meaning that the electric field can begin to penetrate the membrane into the cytoplasm [8].

Initial experiments with psPEF were intended to determine the potential for cytotoxicity, specifically in cancer cell lines. For example, one study showed that applying 800 ps pulses at an electric field of 150 kV/cm required approximately 18, 000 pulses in order to cause 50% B-16 cell death [8]. Using HeLa cells, the application of 800 pulses at a frequency of 3 Hz with varying electric field strength (100-600 kV/cm) and pulse number (100-3000) [9], the cells exposed to the highest voltage and number of pulses had the greatest drop in viability. Most interestingly, the cells were found to die by apoptosis or by programmed cell death and not through the formation of irreversible membrane pores [10]. The rate of cell death after psPEF has been empirically determined to follow a scaling law [11]:

$$S = S\left(E\tau N^{1/2}\right) \quad (1)$$

where S describes the observed biological effect, E is the electric field amplitude, τ is the pulse duration, and N is the number of pulses. There is a biophysical rationalization for this equation. An initial approach was to consider a critical voltage; however, this shouldn't be considered, since the duration of the pulse affects membrane the voltage necessary to cause cell death. Rather, the charge distribution across the membrane should be considered. Because the pulse duration is shorter than the charge time of the membrane, the dielectric properties of the membrane, rather than the resistive values, describe the charge. For a capacitor operating in such a condition, the charge density is given by $\sigma_\varepsilon = \varepsilon E$ where $\tau = \frac{\varepsilon}{\sigma}$, showing a linear relationship between the electric field, the time, and the charge. For a condition in which there are multiple pulses, the $N^{1/2}$ dependence is described by the random orientation of the electric field vector across the membrane. The cumulative field vector for random electric field vectors with equal amplitude but random directions is given by $E = N^{1/2} E_0$ [12]. The importance of this law is that it describes the conditions under which picosecond pulses are likely to cause cell death. As the duration of the pulse decreases, the amplitude of the pulse must similarly increase. This leads to very high electric fields and the requirement of very large numbers of pulses in order to offer an observable effect.

As >100 kV/cm electric fields are likely to cause air breakdown and are impossible-to-be-delivered in an antenna system, lower electric fields needed to be considered for non-invasive applications. To make cells more susceptible to pulsed

electric fields, heating was introduced in the treatment, in addition to psPEF. When Hepa 1-6 cells were heated above 37˚C, there was a synergistic effect that caused a greater cell death at a lower electric field [13]. And there are other potential mechanisms to lower the electric field threshold, including the incorporation of cationic peptides which place additional charges on the cell membrane [14]. Another option is the use of metallic nanoparticles. These could possibly create an electric field enhancement on the cell membrane and reduce the resistivity of the media [15]. It should be noted that neither peptides nor nanoparticles have been confirmed for psPEF applications.

The connection between electricity and neural activity has been well established by Hodgkin and Huxley [16]. Their circuit description of the neuronal action potential consists of a voltage source, variable resistors, and capacitors. The conductance values change based on the probability of an open or closed Na^+ of K^+ channel. When the circuit is solved using Kirchoff's voltage law, the resulting equation is [16]:

$$I = g_{Na} m^3 h (V_m - V_k) + g_k n^4 (V_m - V_{Na}) + g_l (V_m - V_l) \quad (2)$$

where g_{Na} is the sodium conductance, m is the sodium activation, h is the sodium inactivation, g_k is the potassium conductance, n is the potassium activation, and g_l is the leakage conductance. This equation shows that the application of an external electric source (an electric field or a current injection) can modulate the electrical conductance of a neuron.

Experiments were done to assess the ability of psPEF to modulate the membrane voltage and ionic currents. When one hundred pulses at a repetition rate of 500 Hz and a field strength of 20 kV/cm are applied to cultured neurons, changes in Na^+ and K^+ channels result in the firing of a neuron action potential [17]. This is an interesting finding, because the picosecond stimulus is two orders of magnitude faster than the biological response. With higher intensity pulses, as low as a one picosecond pulse was sufficient to activate voltage-gated calcium channels. The application of a single 500 ps, 190 kV/cm pulse to a GH3 cell was sufficient to significantly increase the cytosolic free Ca^{+2} (an important and all-encompassing cell signaling molecule) [18]. Some of these effects can be long lasting with respect to the stimulus. The increase in the ion conductance in NG108 cells lasted for at least 30 s after pulse exposure [19].

One of the prevailing theories about psPEF is that they are capable of inducing intracellular effect. This idea comes from a cell-circuit model, which is shown in Fig. 1 [8]. If an input pulse on the order of milliseconds to microseconds is applied, the majority of the voltage drop occurs on the cell's outer membrane, and little influence is exerted on the intracellular membranes and organelles.

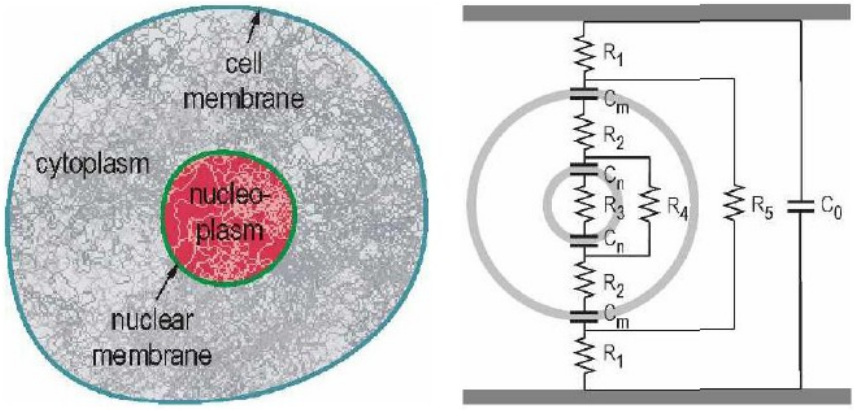

Fig. 1 The cell as a circuit[8]. The cell and nuclear membrane are depicted as a capacitors and the cytoplasm is a resistive element.

As the duration of the input pulse is decreased into nanosecond and picosecond time, the voltage on the outer membrane is reduced and there is a significant voltage on the intracellular bodies and membranes. This occurs because the rise time for picosecond pulses is much faster than the charge time of the plasma membrane. Additionally, picosecond pulses can influence the cell in the dielectric phase in which the cytosol behaves, not as a resistor but as a capacitor. When considering the distribution of dielectric constants throughout a cell, it is likely that the largest electric field will be found in the outer membrane. This, however, doesn't mean that the intracellular organelles are shielded by the membrane. Still, they are more likely affected by the external electric field than longer pulses, provided that the psPEF is of high magnitude.

Despite the possibility of psPEF producing more pronounced intracellular effects, there have been limited studies completed in this area. Most of the information about the sub-cellular effects of psPEF has been inferred from experiments with high field applications. In one study using 500 ps, 190 kV pulses, the change in the cytosolic Ca^{2+}

concentration was suggested to be by the opening of voltage-gated ion channels and not by cell membrane pores [18], since the Ca^{2+} signal was eliminated when the channels were blocked. In a separate study, HeLa cells, pulsed for 800 ps at 250 kV/cm, were found to die through mitochondrial-mediated apoptotic pathways [10]. While the origin of the apoptotic pathway is unclear (extra-cellular membrane charging, intra-cellular membrane charging, or protein modification), picosecond pulses were able to exert some intracellular mitochondrial stress.

Because psPEF is shorter than the membrane charging time constant and the cytosol relaxation time constant, it could also allow for the study of ultrafast biological processes. In this case, macromolecules in an aqueous environment could be affected by psPEF before the charges were redistributed, i.e., before the shielding takes place. It is likely that protein, for example, can be affected in its conformational changes or even in folding. Protein binding may also be influenced by psPEF, since it is known to occur in less than 1 ns [20]. In this light, there may be an undiscovered electrical stimulation paradigm that longer pulses (μs-ms) are not capable of.

1.2 ANTENNAS FOR PICOSECOND STIMULATION OF TISSUE

Perhaps the greatest potential of studying psPEF is the possibility for non-invasive delivery. psPEF offers a huge advantage over slower pulses whose deliveries are restricted to electrodes. Electrode configurations are inherently invasive because the electric field is established between parallel metal plates or rods. The field declines rapidly outside the electrodes, typically according to the inverse of distance square ($1/r^2$). Antennas, on the other hand, designed for the expressed purpose of launching electromagnetic waves into space, emit a wave that decreases as the inverse of distance ($1/r$). Sometimes, electromagnetic focusing by a reflector, a lens or a beam forming can cause a local field enhancement. Using an antenna would allow for the stimulation of deep tissue or of tissues located in inaccessible areas, such as the brain. This allows for more in vivo applications.

There are several reasons why psPEF are well-suited for antenna applications. First, it is because the antenna is electrically small. An antenna radiates energy at frequencies in which the total length of the antenna is greater than the wavelength.

Similarly, in the time domain, the antenna radiates pulses whose pulse spatial width is smaller than the antenna's aperture [21]. By reducing the pulse width, the antenna can become smaller and more efficient. To radiate pulses of picosecond rise time, 300 ps for example, the antenna size can be made small, with a typical length of 10 cm, which becomes manageable in a laboratory setting. Small antennas also mean that the wave travels inside the antenna structure will not decline too fast before the wave detaches the antenna; therefore, the target can have an exposure to a higher field. The next advantage is the high-resolution focusing. The spatial distribution of the pulse can be small for picosecond pulses. For example, in brain white matter that has a dielectric permittivity of 37, the spatial width of a 200 ps pulse is 1 cm [21]. Finally, picosecond pulses allow for the use of high power pulses. Very high power pulses can be applied (up to 200 kV) without causing air breakdown or other dielectric failure [22].

There have been previous attempts to design antennas to radiate pulse electric fields for biological applications. One approach was to use a reflector-type antenna such as the prolate spheroid impulse radiating antenna (IRA) designed by Baum [4]. The antenna has two focal points, one for the source and another for the target in the near field. At the first focal point, there is a source which launches an electromagnetic wave into a dish which reflects the wave. By constructive interference, the reflected waves converge at the second focal point in the tissue. A construction of an IRA can be seen in Fig. 2.

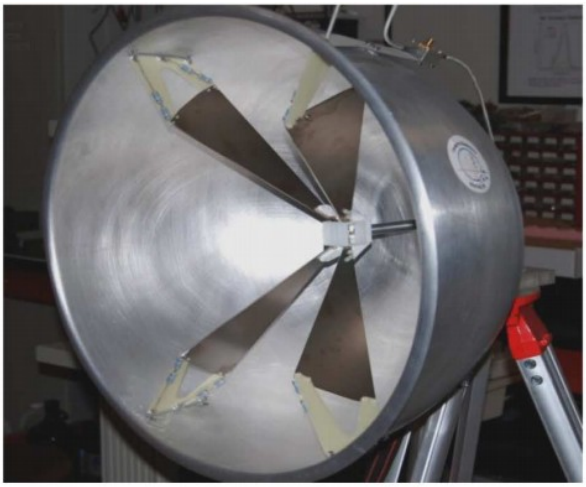

Fig. 2 Prolate spheriod antenna for the stimulation of neural tissue. The antenna is fed by a coaxial cable which is split to feed four arms [11].

In general, the reflector antenna consists of three components: a feed, a reflector, and a balun. The feed consists of four conical arms which launch a spherical transverse electromagnetic (TEM) wave. Alternatively, the arms can be an elliptical horn or biconical wires [23]. Resistors can be placed at the end of the feeding section to absorb the low frequency components. At the reflector, the launched wave is redirected to form an inhomogeneous spherical TEM wave. It is designed to have constructive interference in the near field at the second focal point. The transient electric field at the target consists of several components. The major components consist of a prepulse, which is proportional to the original pulse at the feed, and an impulse, which is proportional to the time derivative of the pulse [24]. In general, for a large field to be radiated, a low antenna impedance and a high input voltage are preferred. The purpose of the balun is to act as an impedance transformer, which interfaces a 50 Ω power supply with a 200 Ω antenna. To make the balun wideband, it is constructed of parallel coaxial cables. Beyond the original design, there have been some improvements. By incorporating a dielectric lens, an enhanced focal point in simulated brain tissue can be achieved [25]. Also, by incorporating a second launching section, there can be an improved electromagnetic field distribution [26].

There have been several challenges with the impulse radiating antenna design concept which have made it not used in biological experiments. First, the pulse magnitude decreases from the first focal point and is proportional to the inverse of distance. More specifically, attenuation of the pulse is governed by the inverse law. This states that the field strength is reduced by a factor of 1/r, with r being the distance from the antenna. Once the pulse reaches the tissue surface, the field drops markedly. Next, the pulses are transmitted in air, causing a large reflection loss at the air-tissue interface. In a simulation of an air-launched wave on tissue, there was a -5 dB transmittance at the skin [27]. This is due to the fact that tissue has a large dielectric constant compared to air. Finally, if the focal point is deep in the tissue, the field becomes low due to the attenuation in tissue and is much lower than the electric field thresholds required for biological effects. These difficulties make the antenna hard to use directly on targets. It was estimated that a source of MV is necessary to drive the antenna, in order for it to

deliver an effective electric field (20 kV/cm) to a targeted area 8 cm in depth in the brain. All of these factors, combined, mean that the electric field produced by these antennas is not great enough to induce any biological effects. To date, no high voltage antenna experiment has successfully been done on biological samples. The delivery of psPEF by antennas has yet to be realized.

While the prolate spheroidal-impulsed antenna is the only high power, high voltage antenna designed specifically for psPEF in vivo stimulation of biological tissue, there have been other lower power pulsed antennas. One such antenna is the ultra-wideband transverse electromagnetic horn. It is a directional antenna with a narrow beam width and it has potential applications in pulse hyperthermia, which is the heating of tissue to temperatures >42˚C in order cause cell death or to make them more succeptable to other cytotoxic agents [28] . Another antenna is Vivaldi antenna. It is a planar antenna with high gain and directivity. It is also ultra-wideband in nature, and it is capable of efficiently radiating picosecond pulses. Vivaldi antennas have been suggested for use in both both hyperthermia [29] and medical imaging [30].

The challenge with these antenna types is that they are unable to support the high electric fields necessary for picosecond pulse stimulation. In the case of the TEM horn, there is no insulation to hold off high voltages. For planar antennas like the Vivaldi antenna, the dielectric strength of the circuit board is a limiting factor. As a result, their application relies on creating an antenna array which utilizes constructive interference in order to have a biological effect. Currently, prototype arrays are being constructed for clinical applications [31].

1.3 TOPIC OF THE DISSERTATION

In the previous experiments, it has been shown that psPEF can exert a biological effect; however, there is not yet an efficient delivery system. In this dissertation, I aim to demonstrate a system that radiates psPEF to stimulate a neurological tissue, e.g., brain, noninvasively. The central question is, “Are picosecond-pulsed electric fields capable of non-invasively stimulating neurological tissue – and, if so, what does that mean for the design of an antenna?” This dissertation is organized into four parts:

Part 1. Explore near-field picosecond-pulsed delivery to shallow targets in the brain using a dielectric rod antenna and an anatomical human brain model. Antennas which launch the pulses into air result in much of the energy being reflected by the skin [32]. By coupling the antenna to the skin through a dielectric rod, I aim to increase the electric field transmittance to levels sufficient for neural stimulation.

Part 2. Develop a pulsed power supply and drive the antenna. To drive the antenna will require a high-voltage pulse power supply in the form of a dual resonance pulse transformer. In theory, dual resonance pulse transformers have no maximum resonance frequency [33]. However, practically, parasitic inductance and capacitance diminish performance. By using a novel geometry, the linearly integrated primary, I hypothesize the reduction of parasitic parameters, allowing for nanosecond charge times.

Part 3. Determine the ability of a picosecond pulsed electric field to non-invasively interact with a neurological tissue for electrical stimulation. When the biconical dielectric rod antenna is used for neural stimulation, the electric field will interact with a variety of cell types. Here the ability of psPEF to induce changes in viability, proliferation, metabolism, and gene expression of cells present in a neural environment will be determined.

Part 4. Evaluate the ability of the antenna in Part 1 to be used in an in vivo application. By comparing the electric field effects seen in Part 3 with the computational electromagnetic antenna simulations in Part 1, the feasibility of an *in vivo* antenna-based applicator will be discussed.

The results from these experiments will aim to 1) explore the design and construction of an antenna-based medical device for neural modulation, 2) discover new intracellular effects of psPEF, and 3) demonstrate possibilities for future psPEF antenna-based therapies. The long term aim of this study is to understand the electromagnetic pulse exposure conditions which can alter cellular activity for therapeutic purposes, with the ultimate goal of developing an antenna-based medical device for neural stimulation.

CHAPTER 2

2. BICONICAL DIELECTRIC ROD ANTENNA

A dielectrically loaded ultra-wideband rod antenna has been studied as a pulse delivery method to subcutaneous tissues, specifically neurological tissue. This choice was made based on the following considerations: 1) the dielectric antenna allows for the compression of the psPEF inside the antenna structure; therefore, a small antenna structure can support the propagation and radiation of psPEF; 2) because the antenna is small in size, the decrease in the electric field before it makes contact with the target will not be as large as that caused by a large antenna, so it is more likely for the field to remain at an adequate level to cause any biological effects; and 3) because the dielectric antenna makes contact with tissue, a more efficient energy coupling can be achieved if the antenna's material has a close dielectric property to the targeted tissue.

The performance of the antenna was examined with respect to: 1) the electric field orientation in the target tissue; 2) the electric field gradient (The electric field decreases as the wave penetrates, but the field at the skin and skull should not be excessively large compared to that in the target zone, so that damage can be avoided); 3) the spot size of the field confinement; 4) the magnitude of the electric field in the brain tissue.

Simulation results applying a 100 ps Gaussian pulse show that it allows us to generate critical electric field for biological effects, such as brain stimulation, in the range of several centimeters. In this instance, the electric field in the brain was 11.5 V/m for a 1 V input. In order to reach the critical electric field for biological effects, which is approximately 20 kV/cm at a depth of 2 cm, the input voltage needs to be 175 kV. The electric field spot size in the brain at this position is approximately 1 cm^2.

In order to verify the accuracy of the simulation, the biconical antenna has been constructed and tested using a commercially available dielectric material (TPL composite with an $\varepsilon_r = 7.3$) in both frequency and time domain. The return loss, or S11, of the antenna describes the frequency response. The antenna had three major resonances (1.73, 2.2, and 2.8 GHz) which corresponded to the simulated S11. In addition, the time results in free space with a moderate voltage (5 kV) confirmed the accuracy of the simulation. These results set the foundation for high-voltage experiments on the complete antenna system and for the delivery of pulses to biological tissue.

2.1 ELECTROMAGNETIC WAVES IN TISSUE

The propagation of narrowband electromagnetic waves in tissue has previously been studied for applications in medical imaging [34]. These studies demonstrate the relationship between frequency, penetration depth, and focusing. In general, an increase in frequency leads to higher resolution focusing. Also apparent is that increasing the excitation frequency leads to higher losses in the form of heat at the skin. The higher frequency elements are absorbed by the skin and do not penetrate into the tissue. This creates an inherent design tradeoff between focusing and penetration depth in the tissue. As the focusing increases by increasing the frequency, the penetration decreases, due to the dielectric properties of tissue. Ultimately, for a given narrowband antenna, there is an optimal frequency to produce the greatest focusing ability while maintaining low skin absorption. For example, in a breast model, the optimal frequency is approximately 3 GHz [35].

To improve on the narrowband findings, ultra-wideband signals or pulses were investigated for their penetration depth and for their ability to focus in tissue. The rationale is that ultra-wideband signals combine the best features of multiple narrowband signals. The low frequency components allow for penetration into the tissue. The high frequency components allow for high resolution focusing. This concept was demonstrated in a computational comparison of narrowband and ultra-wideband signals. The results indicate that the UWB signal consistently showed less scattering and fewer hotspots than the narrowband model [35]. However, it should be noted that not all ultra-wideband pulses have the same effect on tissue. For example, square wave pulses were found to be more effective at penetrating tissue than Gaussian signals [36]. The frequency distribution of the signal is important in determining its propagation. By optimizing the ultra-wideband signal, it may be possible to further improve penetration and focusing.

When an electromagnetic pulse is incident on the antenna-tissue boundary, there are three factors which determine the reflectance (or transmittance) of the radiation. These are 1) the polarization of the electric field, 2) the angle of incidence, and 3) the difference of the dielectric permittivity.

Since the goal of the proposed antenna is to maximize the electric field within the tissue, the conditions with the lowest reflection (Γ) should be selected. The first consideration is the angle of incidence. Utilization of the Brewster angle would seem to be an excellent design choice, but this only applies to narrowband signals and not to broadband pulses. This leaves an incident angle of 0˚ as the best choice. A TEM wave can be either TE or TM polarized. The TE polarization has a lower reflection coefficient and makes for a better selection. In addition, the TE polarization is preferable because the E vector is independent of incident angle, and this setup closely resembles the electric field orientation used for in vitro experiments with electrodes. The impact of the angle of incidence and the polarization is demonstrated in Fig. 3.

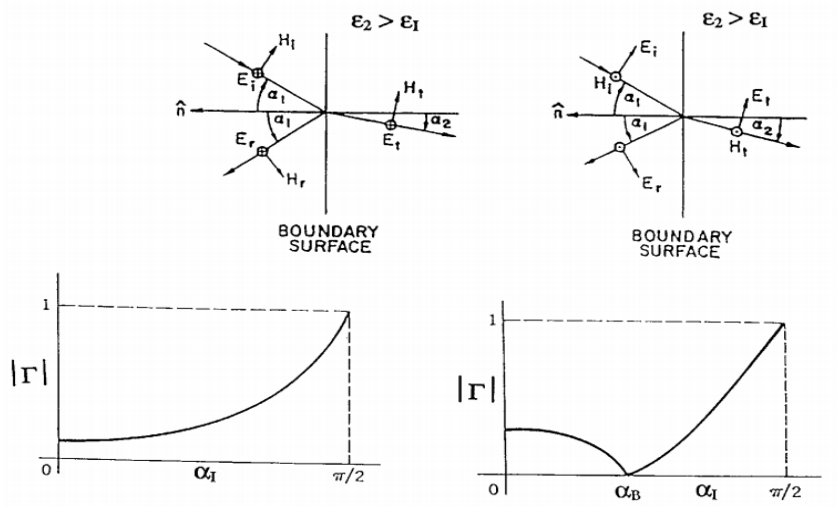

Fig. 3 The effect of polarization and angle on transmittance[37]. The TE mode is preferred because it has the highest transmittance and the electric field vector does not change across the dielectric boundary. The Brewster angle is not applicable for ultra-wideband applications.

In biological studies, the most important factor in describing electric field propagation is the dielectric permittivity. A transmitting antenna sends an EM wave towards the sample under test. If the material is continuous in its electrical properties, the wave will continue unimpeded. If there is any sort of material discontinuity, there will be a reflection with some energy going back towards the source. The amount of energy

reflected can be described by the reflection coefficient seen in (3). It shows that the larger the discontinuity, the more energy that will be reflected.

$$\Gamma = \frac{Z_2 - Z_1}{Z_2 + Z_1} = \frac{\sqrt{\varepsilon_2} - \sqrt{\varepsilon_1}}{\sqrt{\varepsilon_2} + \sqrt{\varepsilon_1}} \tag{3}$$

To understand why this is critical for biomedical applications, the permittivity of various biological materials is shown in Fig. 4. The dielectric constants are much greater than air. For an antenna launching the wave directly into air, there could be an expected 73% reflection at the skin ($\varepsilon_{r\_skin} = 40$).

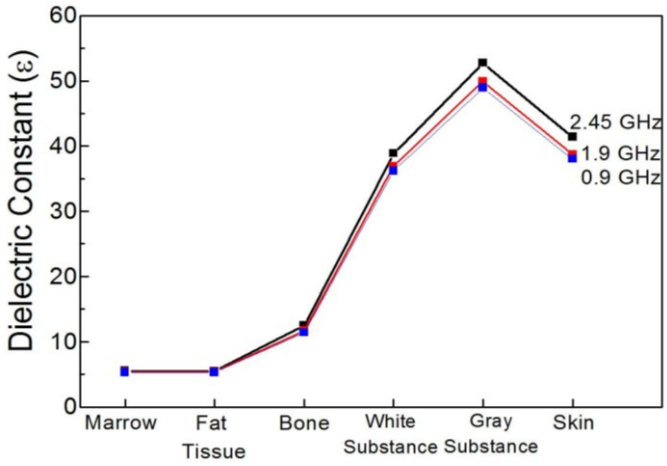

Fig. 4 Dielectric constants of tissue. The dielectric properties vary with tissue type and frequency.

The description of the reflection as a function of dielectric permittivity (3) is a simplified analysis. It only applies to an ideal, homogenous material whose size is much larger than the pulse spatial width (no interaction with other material types). This is not the case in biological models.

The dielectric relaxation of biological tissues, which represents the change in dielectric constant of material under a transient electric field, has been empirically derived [38]. This data was then fit to a first-order Debye model. It is a complex permittivity as a function of frequency [35]:

$$\varepsilon_r(\omega) = \varepsilon_\infty + \frac{\varepsilon_s - \varepsilon_\infty}{1 + j\omega\tau} - j\frac{\sigma_s}{\omega\varepsilon_0} \tag{4}$$

where ε is the permittivity at infinite frequency, ε_s is the static permittivity, τ is the relaxation constant, σ_s is the static conductivity, and ε_0 is the free space permittivity. The terms can be thought to represent an equivalent circuit with a real and imaginary part in series. There are other models that can be used to describe the tissue dielectric properties. Most notable is the Cole-Cole model. This is considered to be a more accurate model, especially over large frequency ranges; however, it can only implemented at a high computational cost [39]. Within the frequency range of this paper (0-5 GHz), the Debye model balances accuracy with computational cost.

One of the challenges of biological models is dealing with the dielectric discontinuities between tissue types. There is no standard way of accounting for changes in dielectric properties. Previously, three models have been suggested [35]. These are a uniform model which considers only an averaged tissue dielectric, a piecewise linear model which assumes distinct tissue types but with an averaged tissue at the interface, and a biomodal model which assumes distinct tissue types with sharp transitions between the tissue types. In this simulation, the bimodal model was selected, since it is the most conservative model with the greatest reflection losses and scattering at tissue boundaries.

2.2 AN IN VIVO BICONICAL DIELECTRIC ROD ANTENNA DESIGN

Biconical dielectric rods, sometimes referred to as “polyrods” due to their construction out of polyethylene, have long been studied for their uses in millimeter wave communications [40]. They have been noted for their high gain, narrow beam width, and low side lobes, making them ideal for end-fire applications. In general, they consist of three sections: the feed or wave launching section, the dielectric wave guide, and the wave emitting section.

The feed section couples the antenna to the power supply and establishes the wave within the dielectric. When the wave enters the feed, there is a change in impedance, so it must be designed to reduce reflections. In the case where there is a difference in permittivity between the material of the feed and the antenna, the change in impedance is accompanied by a slowing of the wave ($v = \frac{1}{\sqrt{\varepsilon\mu}}$). Additionally, any discontinuity in the

geometry of the guided metallic component creates opportunities for unintended scattering.

The waveguide section acts to isolate the feed section from the radiation section and to establish the hybrid wave. The intent behind isolation is to allow for evanescent modes to decay while preserving frequencies of interest. See Appendix A for a discussion on evanescent waves. For good isolation (from the feed and the evanescent wave), the recommended length of the rod is 6λ [41]. The $HE_{11,}$ or the hybrid mode, is the fundamental mode. It has no cutoff frequency, and the energy is concentrated in the center of the dielectric. Both the electric and the magnetic field vectors are normal to the direction of propagation. The diameter of the rod ought to be at least $\lambda/\sqrt{\varepsilon_r}$ [40].

In the radiation section is the interface between the antenna, and the free space and its taper determine the radiation pattern. If the intent of the antenna is to be used in the end-fire mode or focused in the near field, the propagation can be described by Snell's Law. If a more sophisticated pattern is necessary, the complexity of the taper must also increase. While the effective diameter of the rod is greater than or equal to λ, the energy is confined to the rod. When material is removed and the diameter of the rod is no longer greater than λ, the energy is radiated. As a result, the longer wavelength (lowest frequency) components begin to radiate at the beginning of the taper, and the higher frequency components remain guided until the size of the rod becomes less than one wavelength [42].

At first, the biconical dielectric rod antennas known as polyrods were designed to be narrowband, although it was the circular waveguide feed that determined the bandwidth [41]. The rod itself was broadband and could support hybrid (HE11) mode propagation. There have been several techniques for constructing a desired radiation pattern. Tapering the body along the length the rod reduces the side lobes and can minimize standing waves caused by reflection at the terminal taper [43]. Additionally, the antenna can be fed with a conical horn in order to improve the gain [42]. These antennas have applications in microwave communications systems.

By changing the feed structure, the dielectric rod antenna could be used in wideband applications. The most prominent design is by Chen [44] for applications in ground penetrating radar. In this antenna, the feed section consists of two dielectrically

loaded conical plates fed by a coaxial cable. Interestingly, they elected to extend the conical feed section into the cylindrical waveguide section using an exponentially tapered resistive film. This was used to avoid antenna ringing on the arm. The film helped to ensure broadband operation, but did so at the price of reduced efficiency [45]. It should be noted that there are other techniques for feeding a wideband dielectric rod antenna, although the antenna is no longer biconical. This includes a biconical dipole combined with a reflector [46] or a helix [47].

The Chen design has been modified for biomedical imaging applications [48]. By using dielectrics, the antenna can be placed in contact with the skin, which eliminates the need for a coupling liquid. Also, dielectrics allow multiple antennas within an array to be closely spaced without high levels of crosstalk. This improves the image construction for small tumors.

The structure of the antenna is shown in Fig. 5. The impulse source is connected to the apex of the wave launching section, so a TEM wave is formed and is further guided to the wave emitting section by the dielectric wave guide. Throughout the antenna, the same dielectric material is used. Unlike a typical antenna that points to the free space, this antenna makes direct contact with a tissue through the dielectric cone in its wave emitting section. There is no air gap between the antenna and the tissue.

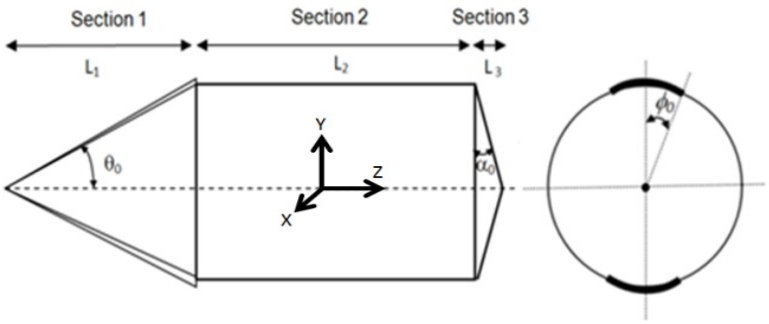

Fig. 5. A biconical antenna that is loaded with a dielectric. The antenna consists of three sections (launching, waveguide, and emitting). The geometry is defined by three angles and three lengths. [21]

In Section 1, the wave is launched by a conical waveguide centered on the y axis and is characterized by two angles: θ_0 and ϕ_0. In Section 2, the waves emitted from the

launching section are guided by a dielectric rod to the emitting section. In Section 3, the waves are detached from the antenna and propagate in the +z direction.

In the wave launching section (Section 1), two triangular metal plates are bent in a conical shape to symmetrically cover part of the dielectric cone. This part of the antenna is defined by two angles: the apex angle θ_0 and the azimuth angle ϕ_0. Such an antenna was studied by Shen et al. [49]. The characteristic impedance of the wave launching section is:

$$Z_0=\frac{Z_c}{2\sqrt{\epsilon_r}}\frac{K(\cos\phi_0)}{K(\sin\phi_0)} \quad (5)$$

where

$$K(\sin\phi_0)=\int_0^{\pi/2}\frac{d\beta}{\sqrt{1-\sin^2\phi_0\sin^2\beta}},$$

$$K(\cos\phi_0)=\int_0^{\pi/2}\frac{d\beta}{\sqrt{1-\cos^2\phi_0\sin^2\beta}},$$

Z_c is the free space impedance (377 Ω) and ε_r is the dielectric permittivity of the dielectric. For the dielectric we studied, Aluminum Nitride ceramic (ε_r =7.3), the characteristic impedance is shown in Fig. 6. This allows us to identify the angle of ϕ_0 for a given impedance.

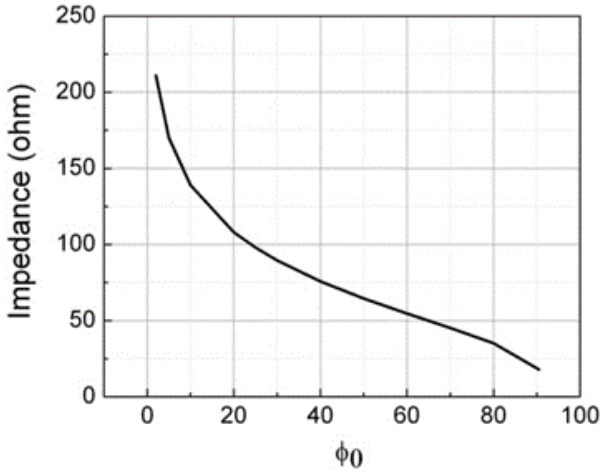

Fig. 6. The characteristic impedance of the AlNi antenna [21]

The important features of an infinitely long version of this antenna (only the wave launching section) are: 1) frequency independence (important for wide-band pulses), 2) uniform azimuthal directivity, and 3) TEM mode excitation. However, we have to consider an antenna with a finite length, which can be as short as a few centimeters. The

scattering of the electromagnetic waves at the end of the conical transmission line will, in this case, cause pulse ringing or pulse broadening at the target. This corresponds to the increase in pulse duration at the target. This may be unfavorable for radar or communication applications, but for biological applications, it may be useful since the threshold electric fields for biological effects generally are reduced as the pulse duration increases, thus easing the requirement of the pulsed power system.

Dielectric wave guides are commonly used for guiding high frequency electromagnetic waves, such as millimeter waves and light waves. While many modes of waves can propagate in the cylindrical wave guide, the fundamental mode (lowest) is HE_{11} mode, for which the cutoff frequency is very low. As such, wideband signals are favored [50]. Outside the waveguide, an evanescent wave propagates with the speed of light in free space, but the field intensity decreases exponentially in radial direction from the waveguide surface. So the wave energy is mostly confined in the dielectric wave guide.

The radius (R) and the length of the dielectric wave guide (L) should ensure the clear separation of the wave directly reaching the end of the wave guide from that scattered off at the discontinuity between the conical wave guide and the dielectric wave guide.

When determining the diameter of the rod, a rule of thumb is that the radius R should be greater than the pulse spatial width:

$$R > \frac{t_p c_0}{\sqrt{\varepsilon_r}} \qquad (6)$$

where t_p is the pulse duration. This means that the pulse reflected from the rod-air interface will be temporally separated from the existing pulse on the axis. The axis is the location of the highest power density, and consequently the pulse is defined mainly by the waves on the axis. For small radius rods, the reflection adds to the existing pulse temporally, creating distorted waveforms. This distortion is pronounced for low frequency waves or for long pulses. Therefore, the radius essentially determines the low frequency limit of the antenna.

As far as the length of the dielectric wave guide L concerns, it should satisfy (Fig. 5):

$$\left(\frac{R}{\sin\theta_0} + \sqrt{R^2 + L^2} - \frac{R}{\tan\theta_0} - L\right)\frac{\sqrt{\varepsilon_r}}{c_0} > t_p \qquad (7)$$

This condition ensures that the pulse will not be broadened once it reaches the end of the wave guide. Waves scattered off at the discontinuity at the interface from the dielectric rod to the air also contribute to the pulse duration if they reach the end of the wave guide at the same time and cause a broadening of the pulse.

At the intersection of the conical wave launching section with the cylindrical wave guide (Section 2), the incident waves should, ideally, be reflected toward the axis of the cylindrical wave guide. This can be achieved by using the concept of total internal reflection. The critical angle for total internal reflection is:

$$\beta_0 = \sin^{-1}\left(\frac{1}{\sqrt{\varepsilon_r}}\right) \qquad (8)$$

with ε_r being the relative permittivity of the dielectric and with β_0 being the complementary angle to the apex angle (Fig. 7).

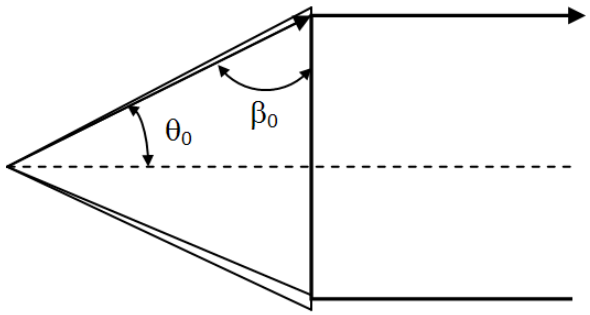

Fig. 7 The critical angle for total internal reflection applies to the wave when it is guided by a conical wave guide. [21]

When Eq. 4 is applied to dielectrics with large permittivity, the result is a relatively small β_0 and consequently a large θ_0. For example, $\beta_0 = 21°$ for $\varepsilon_r = 7.3$. Such a configuration, in which the wave launching section is rather short, is undesirable. This is because the waves propagating at angles $\theta < \theta_0$ in the wave launching section will arrive at Section 2 earlier than those where θ is close to θ_0 (see Fig.4, dashed line). Consequently, at the interface of Section 1 and Section 2, the wave front is still spherical. In order to preserve the pulse shape of the incident pulse in the cylindrical wave guide, the incident waves in Section 2 should ideally be planar waves. However, this can only

be achieved by using a small slope launcher (large β_0 and small θ_0), which resembles, to some degree, two parallel plates.

It seems that keeping the wave launching section short (large θ_0) offers certain advantages, such as low losses due to scattering and high axial electric fields in the rod. However, that needs to be balanced against the distortion of the waves. Considering the importance of preserving the pulse shape in the antenna, it might be still preferable to use a wave launcher with a small apex angle.

The electric field radiated from the wave launcher can be obtained from aperture theory [51]. Given the coordinate system seen in Fig. 1, the tangential component of the electric field on the aperture plane is known [49], and the radiated field at a point on the axis is:

$$\left(\overrightarrow{R_0}, t\right) = \mathrm{E}_0\{\alpha_{y,y}^{(1)} \frac{a^2}{R_0 c} \frac{\partial}{\partial t} f\left(t - \frac{R_0}{c}\right) + \alpha_{y,y}^{(2)} \frac{a^2}{{R_0}^2} f\left(t - \frac{R_0}{c}\right) \quad (9)$$

where R_0 is the distance of an observer on the axis from the aperture center. The input pulse has a time dependence of f(t), but for the observer, the pulse has a propagation delay of $t - R_0/c$. For the near field, this delay is negligible. The field depends on both the input pulse voltage and the time derivative of the pulse. Specifically, for the field term near the antenna, f(t) is dominant, and the time derivative term $\partial f(t)/\partial t$ is dominant for the field far from it. The coefficients $\alpha^{(1 \text{ or } 2)}{}_{y,y}$ depict the integral of the tangent electric fields over the aperture plane. In general, homogenous unidirectionally-aligned "currents" resulting from a uniform illumination produce larger coefficients, and hence larger electric fields. In this case, a low impedance conical wave launcher (correspondingly large ϕ_0) is preferable for radiating waves at high intensity. The aperture size preferably is comparable to the observing distance, so the ratios of $\alpha^{(1 \text{ or } 2)}{}_{y,y}$ over R_0 or ${R_0}^2$ are not small, which means that the ratio of L/R should not be too large.

The purpose of the third section of the antenna is to radiate the electric field into the tissue. Applying the ray theory, the dielectric taper refracts the incident waves and directs them towards the apex. In this way, the terminal taper acts like an axicon with a majority of the energy entering the tissue near the apex.

The impinging ray should be reflected at the surface of the cone and then should exit from the cone apex. This requires the angle of the cone to be α_0, the critical angle for total internal reflection (Fig. 8):

$$\alpha_0 = \sin^{-1}\left(\frac{1}{\sqrt{\varepsilon_r}}\right) \tag{10}$$

This ensures that the rays that are in parallel with the axis reach the cone apex and radiate into the tissue. For fields scattered off at the end of the wave launcher, the incident angle, α, can be larger than α_0. They are still totally reflected, but the overlying beams create focal points inside the cone, rather than reach the cone apex. When α is smaller than α_0, refraction occurs, and the transmitted wave departs the cone and becomes spread around the cone apex. This causes a widening of the focal spot in the tissue.

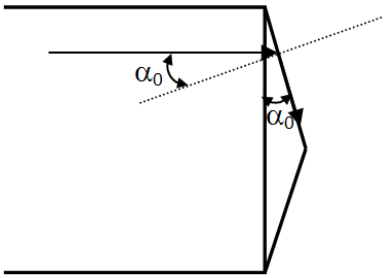

Fig. 8 Snell's Law describes the conical emitting section [21]

Prior to constructing the biconical dielectric rod antenna, each element of the antenna was studied separately. This began with the conical wave guide or the launching section of the antenna.

First, modeling and simulation was used to study the propagation of the electric field from the conical antenna through three layers of biological tissues. This was done with the aid of the 3D EM simulation software, Computer Simulation Technology (CST) Microwave Studio. Underlying the software is a finite difference time domain algorithm (FDTD). This solves a discretized, differential form of both Ampere's Law and Faraday-Maxwell's Law, based on a forward Euler method. The FDTD algorithm is suitable for this simulation. This is because it solves directly for E and H, which are the components

of interest. It also solves the equations in the time domain, which allows for a single simulation to account for all of the frequency components of the input signal. The greatest weakness of this approach is that it uses a uniform, square grid. This causes the model to become a staircase at curves in the model. For a biological model with many amorphous curves, this makes the grid technique undesirable. A very dense grid is necessary to mitigate this effect. For this reason, CST implements a non-uniform grid in order to enhance resolution at sharp or rounded edges [52]. The use of non-rectangular grids, such as trapezoids, is limited [53].

The model consisted of an applicator antenna and a target. First is the antenna. This consisted of the combination of a hollow outer and a solid inner cone. The outer cone was modeled as a perfect electrical conductor, and was split in two. Across the ensuing gap, the pulse (1 V peak, Gaussian, 0-5 GHz) was applied. The inner cone was a solid, dielectric material of $\varepsilon_r = 7.3$. The height of the cone was 40 mm and diameter was 20 mm.

The target of the pulses was a three-layer rectangular prism. The layers were 3mm of skin, 6mm of bone, and 16 mm of brain tissue. The electrical properties of the tissue were third order fits to the biological data [38]. The model showing the antenna model and various dielectrics can be seen in Fig. 9.

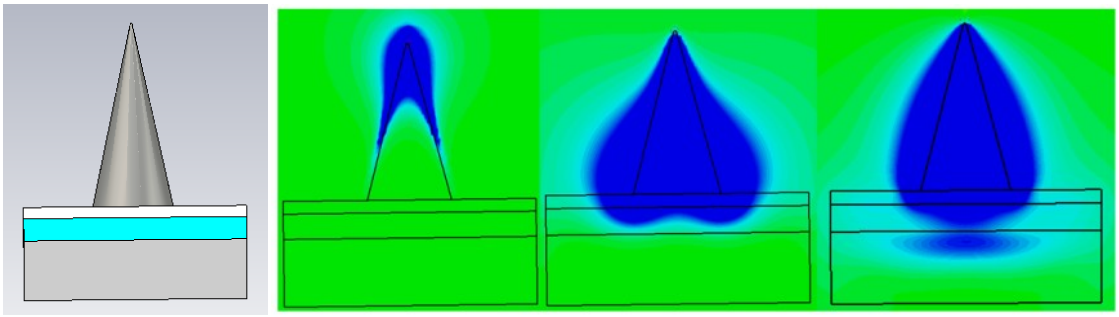

Fig. 9 Conical antenna on a three layer tissue target

The transient plot shows that the electric field propagates through the three layer target with little attenuation. The magnitude of the electric field 10 mm below skin surface was 16.4 V/m for a 1 V input and was concentrated in the area directly below the antenna. Additionally, the pulse waveform at the brain tissue was similar to that of the input pulse, suggesting that the waveform was governed by the voltage transient, V(t).

The results of the simulation demonstrate the possibility of creating an antenna to deliver electric pulses to shallow subcranial targets with high penetration depth and resolution. However, this antenna is not suitable for the final design. The metallic components make direct contact with the skin, which at high voltage could be dangerous. There is also strong electric field at the tips of the antenna which is not the intended function of the device.

Validating the model and the design of the conical wave emitting section is a critical step. This is because the mesh density of the simulation is lowest at the cone apex where the pulse originates. This is the most likely source of error in the simulation, which could potentially propagate throughout the data set. Thus, confirming the simulation results at this juncture lead to more certainty in the later simulation results.

Ideally, the antenna would be tested on artificial tissue stimulants of skin, bone, and brain with a receiving antenna embedded in the tissue for measuring electric fields at various positions, similar to that described in [5]. While this experiment is still under preparation, we report on the validity of the modeling results by constructing a conical antenna and measuring the electric field in free space. The conical antenna was designed as 200 Ω and only has Section 1, i.e., the wave launcher. The two triangular metal plates that make up the wave launching section were adhesive copper foil with an azimuth angle $\phi_0 = 2.5°$. The antenna had AlN ($\varepsilon_r = 7.3$) as the dielectric material and was constructed with a base diameter of 20 mm and height of 36 mm. The antenna was driven by a FID pulse generator (FID) through a 1:4 balun (50 Ω: 200 Ω). It was mounted in the upright direction. To measure the field on the vertical axis, a Prodyn AD-80(R) D-dot sensor was used. The setup is shown in Fig. 10. We note that the sensor is a differential probe that has a ground plane which was aligned to the mid-plane of the conical antenna. The effective area of the D-dot sensor is in the emissive probe with an area of 3×10^{-4} m^2. The probe was aligned with the axis of the conical antenna. By adjusting the vertical position, the field distribution in the free space could be measured. The signal was integrated on the oscilloscope to obtain the electric field.

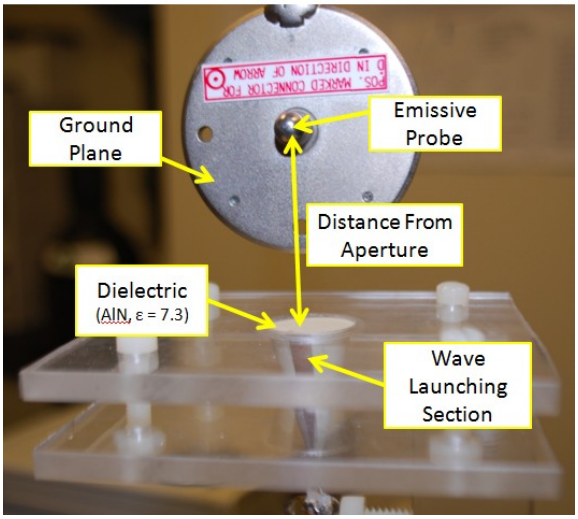

Fig. 10 The experimental setup of the conical section in free space showing the conical antenna and the D-dot receiver (Prodyn AD-80 (R)). [21]

The measured electric field and the simulated result are shown in Fig. 11. The two waveforms are almost identical at times of less than 2.7 ns, but a difference occurs afterwards. This is due to the wave scattering on the holder and desk, which is not included in the simulation. Fig. 12 shows the results obtained from Eq. 9 (analytical) as well as from the simulation and from the measurements. The three results are very close, except at the distance of less than 40 mm; here, the measurement results are slightly lower than the modeled and calculated values. In this case, the error could be caused by the finite size of the effective biconical area of the probe. The field across the probe is not homogenous when the probe is close to the antenna aperture. As the distance from the antenna aperture increases, such distortion becomes diminished, so the results are almost identical to the simulation and the analytical results. Overall, the results of these experimental studies indicate that the results obtained for the human voxel model can serve as a guide for the future experiments in tissue.

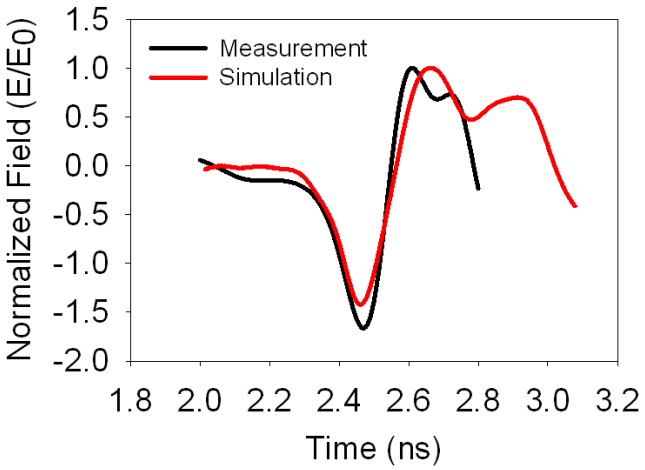

Fig. 11 Measured and simulated transients of the conical launching section [21]

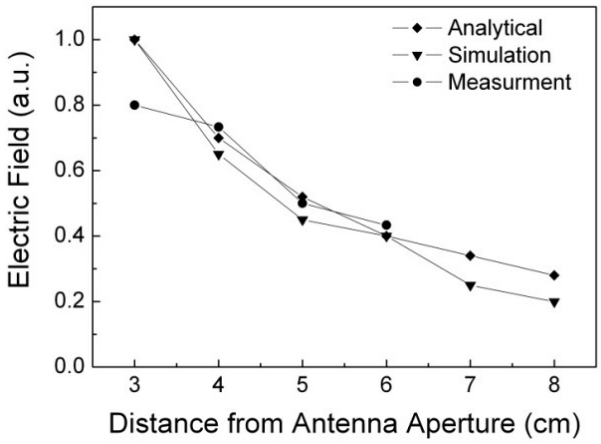

Fig. 12 Attenuation of the electric field as a function of distance from the aperture for a 200 Ω conical antenna. Measurement results, simulated results and the analytical results from Eq.9 are shown. [21]

Having established the simulation and construction of the conical launching section, the cylindrical waveguide was added in series. The same three-layer tissue model and feed signal was used to determine the propagation of electric field with the combined conical-rod configuration. In this simulation, the goal was to observe the confining of the electric field to the center of the cylindrical rod and to transmit an electric field into the tissue at approximately the same levels as seen in the cone-only model. The transient results of the simulation can be seen in Fig. 13.

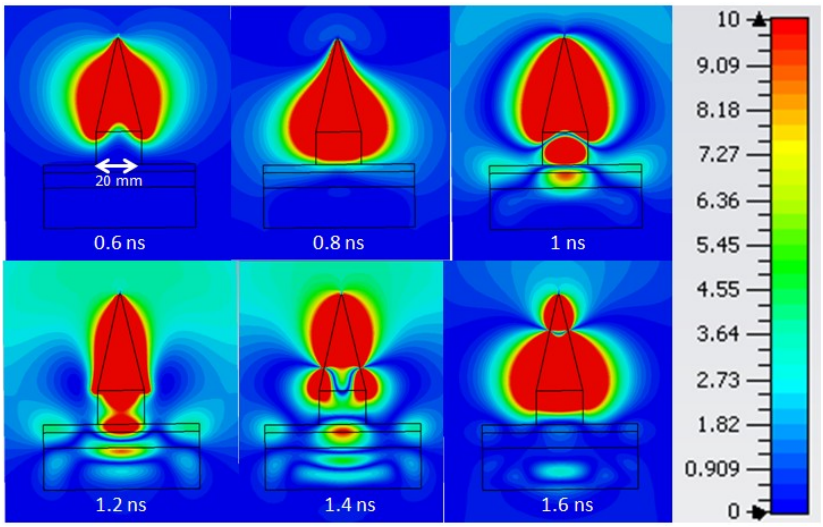

Fig. 13 The combined cone-rod antenna transient on a three-layer tissue model

At 0.6 ns, the electric field transverses down the cone, until it meets the rod at 0.8 ns. At this point, there is scattering at the tips of the conical section. Looking at 1 ns, the field is propagating, independent of the conical launcher and into the tissue. This is indicative of the formation of the HE11 mode in the rod. At 1.2 ns, the field meets the brain tissue with a magnitude of approximately 10 V/m for a 1 V input. The peak field is directly along the axis of the rod. The electric field attenuation, through the three-layer model, has an approximately log-linear relationship, which is dependent on tissue type. This can be seen in Fig. 14, where there is a discernible change when the field encounters a new tissue type.

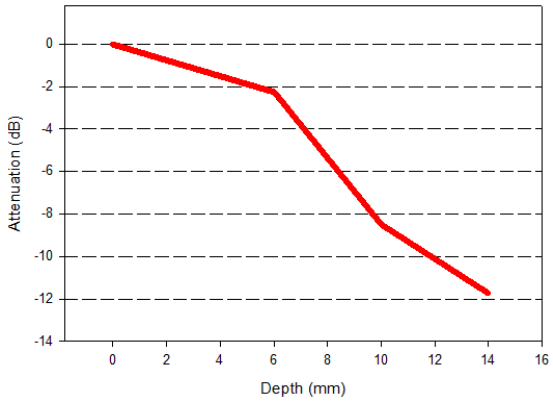

Fig. 14 Attenuation as a function of depth in the cone-rod three layer model

For the proof of concept of the biconical dielectric rod antenna, there was a simulation of the conical launching section, validation of the launching section in free space, and a simulation of the combined launcher and rod. All of these results were in accordance with the design formulas and criteria. This set the foundation for the study of the entire biconical dielectric rod antenna. Additionally, the tissue type is not limited to neurological tissue but can also be used for superficial targets such as skin or tissues in culture. For such targets, the terminal conical end may not be required, since the results should approximate those completed with just the conical launcher and the rod.

The wave launcher (Section 1) was designed to use with a commercially available nanocomposite material ($\varepsilon_r = 7.3$) from TPL Inc., and to have an impedance of 50 Ω. Using these criteria, the azimuth angle ϕ_0 was determined to be 62.95°, according to Eq.1 and Fig. 6. For a pulse width of 100 ps, the diameter of the rod, which equals the base diameter of the wave launcher, can be determined from Eq. 2, as R > 1.11 cm. As a result, a radius of 1.5 cm was chosen. For $\theta_{0,}$ we chose an angle of 29°. The length of Section 2 was set to be twice the value of R: 3 cm. Finally, the angle of the cone α_0 in antenna's Section 3 was calculated to be 21°. These parameters were used as the initial values for the CST model, but were, in the following, optimized using CST studio's Trust Region Framework optimization algorithm. The goal of the optimization was to maximize the electric field inside the brain tissue at a depth of 20 mm.

At the apex of the cone, the pulse with Gaussian waveform and an amplitude of 1 V was applied (0-5 GHz). The antenna was applied to a CST partial head voxel model with a resolution of $1\times1\times1$ mm^3. The target was organized into layers composed of 1 mm of skin, 5 mm of fat, 8 mm of bone, 1-10 mm of optical nerve, and at least 50 mm of intermingled grey and white matter. Their respective electrical properties were provided by a first-order Debye approximation of Gabriel-Gabriel's experimental results [38].

There were three parameters for the model optimization. These were the rod diameter (R), the rod length (L), and the taper angle (α). The final geometry can be seen in Fig. 6. The dielectric rod had a radius of 30 mm and a height of 35 mm. For the wave emitting section, the angle α was 10°.

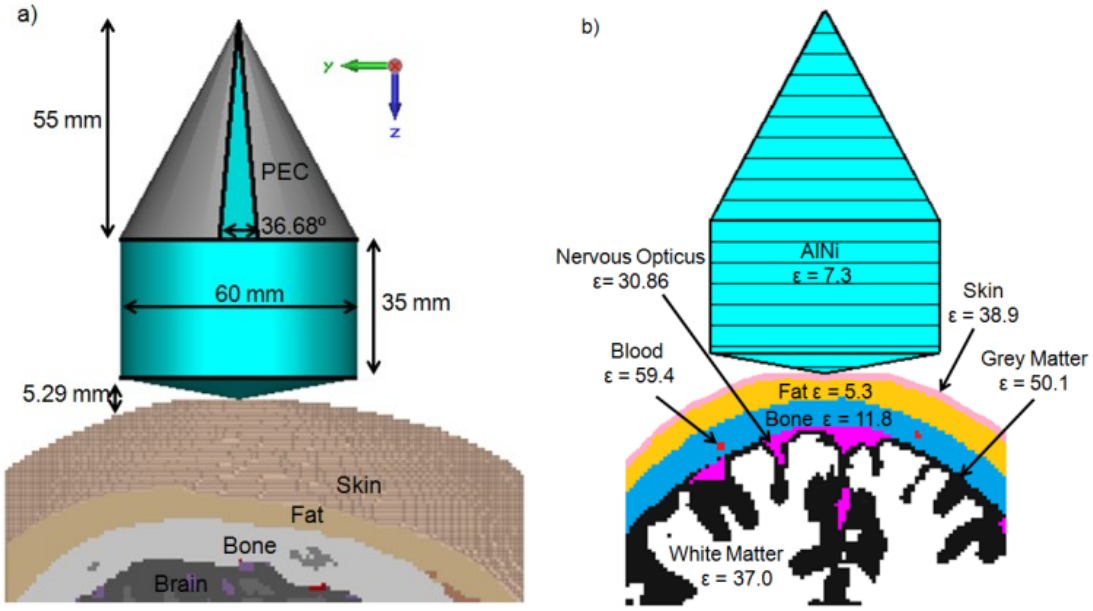

Fig. 15. The CST model showing a) the dimensions and b) the material permittivity [21]

The transient results show that a wave launched from the apex is guided to the emitting section, as shown in several snapshots (Fig. 16). The electric field travels down the wave launching section in a spherical wave form at 0.75 ns. The pulse is scattered at the joint between Section 1 and Section 2. Three scattered waves can be clearly observed at 1 ns: a reflected wave which bounces back to the source, an evanescent wave on the rod surface, and the waves confined in the rod. The last part refracts into the brain tissue at 1.25 ns and reaches the brain tissue at 2 cm depth at 1.5 ns.

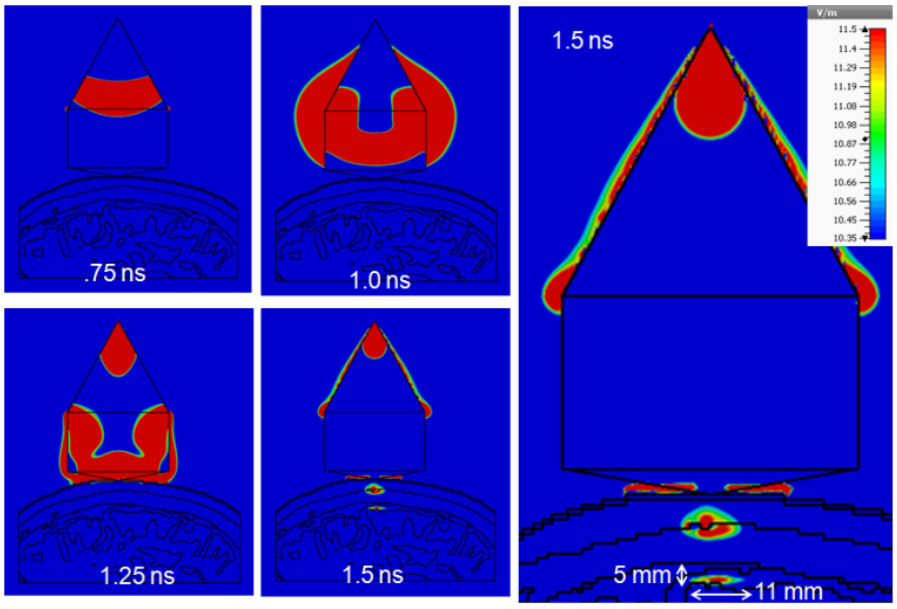

Fig. 16. The transient propagation of the electric field through the brain [21]

The performance of the antenna was assessed in terms of the electric field orientation, the spot size, and the magnitude. The electric field orientation at the 2-cm deep layer can be seen in Fig.8. The electric fields were clamped at the values greater than 90% of the maximum value in the brain tissue for an easy observation. In general, the field was oriented in the -y direction. It was confined to the area projected straight down from the apex of the dielectric rod. Inside the brain tissue, the electric field lines are approximately linear and run parallel to the skin-wave launcher interface. The maximum fields are concentrated in the area directly underneath the center of the wave launcher. It is desirable to have such linearly oriented fields in the confined region. This is a similar field structure to that obtained with the parallel plate electrodes and it allows us to compare results obtained in vitro with those expected by this antenna.

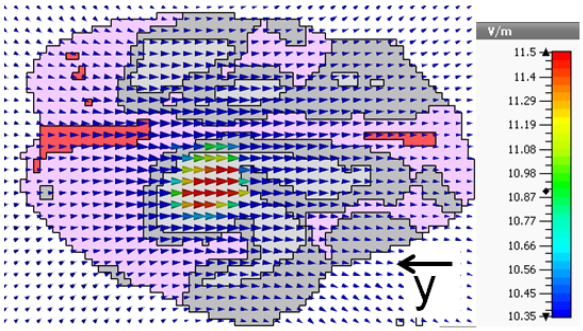

Fig. 17 The electric field orientation and magnitude inside the brain. The electric field is linearly oriented inside the brain tissue. The size of the arrow indicates the intensity of the electric field. [21]

If we define the stimulation spot size as the area that has the electric field value greater than 90% of the peak value, the thickness and width of the stimulation spot can be estimated to be 5 mm by 11 mm (Fig. 16). At the surface, the spot size is on the order of the diameter of the waveguide and it shrinks until reaching 11 mm in width in the brain tissue (2 cm deep). This field concentration is caused by the tissue attenuation, since the electric field is highest at the center and it remains that way at deeper regions in the brain (Fig. 18).

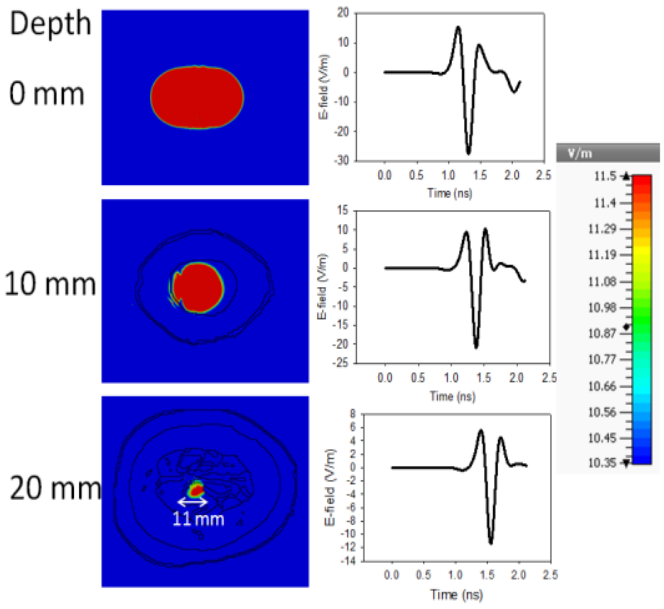

Fig. 18 The spatial electric field and transient at three cross sections of the brain. The field decreases in both magnitude and size with increasing depth. [21]

The peak values of the pulse waveforms are plotted versus depth (Fig. 19). It shows that, as the depth increases, the peak electric field decreases. The electric field in the brain tissue is approximately 42% of that at the skin surface. In terms of absolute field, the peak field in the brain is 11.5 V/m for a 1 V input. This implies that skin tissue may need to tolerate a field level 2-3 times that of a brain tissue. Using 20 kV/cm as a threshold for a biological effect [17], a 175 kV pulse power supply would be required.

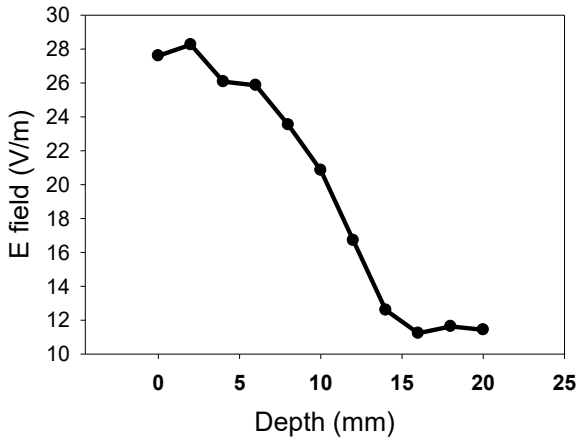

Fig. 19. The electric field maximum with depth in the brain [21]

In a simulation, electric pulses in the hundred picosecond range were successfully delivered to the subcutaneous region of the brain using a conical dielectrically loaded antenna. The antenna makes a direct contact to the tissue, without an air gap, thus reducing the large reflection losses due to the difference in the permittivity of air and tissue. For the dielectrically loaded antenna ($\varepsilon = 7.3$), the electric field at a depth of 20 mm (inside brain tissue) was shown to be 11.5 V/m for a 1V input. In order to stimulate tissue, the critical electric field needs to be on the order of 20 kV/cm, as found in our previous study [17]. This critical field corresponds to an input voltage of 175 kV. This voltage is achievable with current pulsed-power systems. The spot size in the brain is estimated to be 5 mm × 11 mm × 11 mm and is better than that created by other neural stimulation modalities, specifically repetitive transcranial magnetic stimulation (rTMS) [54]. For this spot volume, the electric field at the skin is 2.4 times greater than the field in the brain tissue. The model used in this study was validated by comparing the modeling results with experimental results. The results obtained in free space suggest that the antenna simulation is reliable and that it can provide a solid ground for the necessary experiments to confirm the utility of the complete dielectrically loaded antenna in biological tissue.

It should be noted that the antenna is not limited to neurological applications. For example, it can be used to target skin, fat, muscle, or bone. Potential therapies could include wound healing or regeneration. To demonstrate this concept, the same dielectric rod which was previously applied to the brain was simulated on a three dielectric layer model consisting of skin, fat, and muscle tissue with a thickness of 1 mm, 2 mm, and 10 mm, respectively. The main result of the simulation can be seen in Fig. 20.

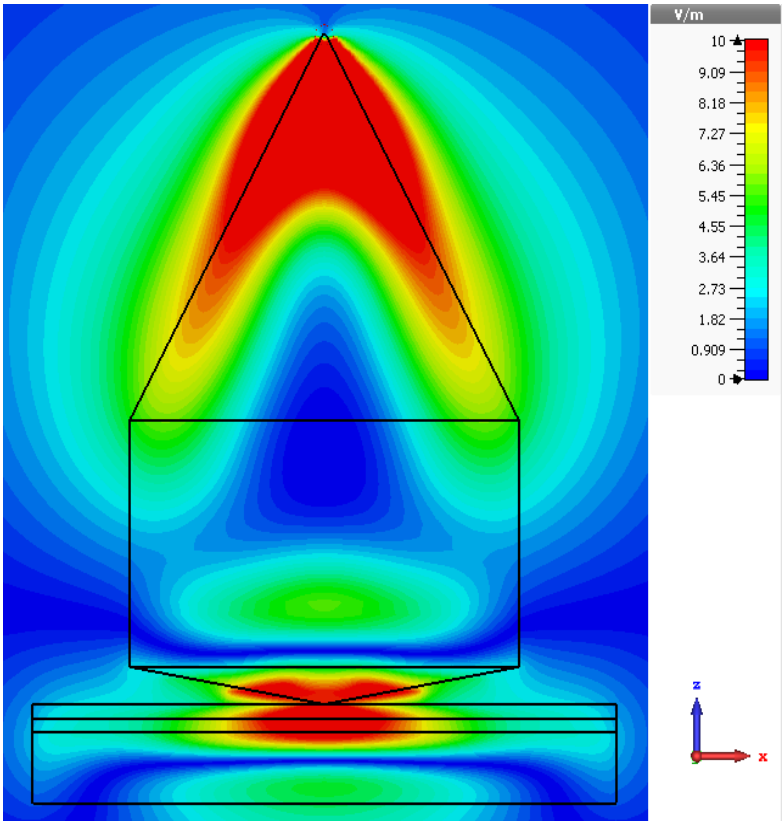

Fig. 20 Antenna on a three layer model

The electric field is concentrated to the center of the rod, and the maximum electric field is at the apex of the emitting section. While the field was weaker than the brain model, these results could be greatly improved if the antenna geometry was optimized for surface stimulation. The principal change would be adjusting the angle of the emitting section to focus on the surface.

2.3 ANTENNA CONSTRUCTION AND CHARACTERIZATION

The dielectric rod antenna was constructed from a proprietary nanocomposite material with $\varepsilon_r = 7.3$, developed custom by TPL Inc (Albuquerque, NM) for the purpose of applying picosecond pulses to brain tissue. The launching section was constructed using copper tape and was designed to have an impedance of 50 Ω, in accordance with [49]. It was machined to the dimensions shown in Fig. 15.

CST Microwave Studio was used to simulate the antenna in free space without the presence of tissues. For the transient simulations, the antenna was stimulated with the normalized waveform of an FID 5-P pulse generator, since this is the pulse generator that will be used to verify the simulation. The pulse has a rise time of approximately 200 ps and a full width at half maximum of 640 ps. The Fourier transformation shows that the signal is dominated by the low frequency components and has a peak frequency component at 0.17 GHz (see Fig. 21).

Radiating the peak frequency with this antenna is impossible, since the rod diameter needs to be 0.65 m in order to confine most of the energy in the rod. However, radiating electromagnetic waves at 1.7 GHz or at any higher frequencies becomes possible, since the diameter in this case is reduced to 0.065 m, which is close to the 0.06 m that the antenna rod was finally designed to be. Certainly, one could choose a dielectric that has dielectric constant larger than 7.3, allowing for confining the field at low frequencies with the same antenna diameter.

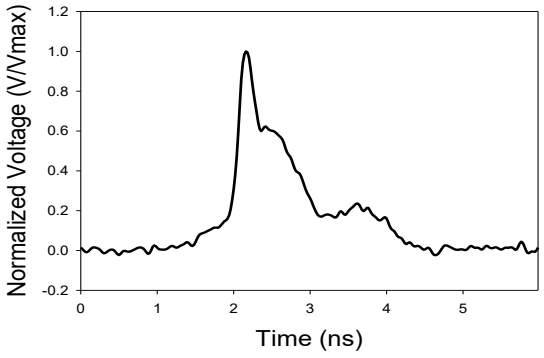

(a)

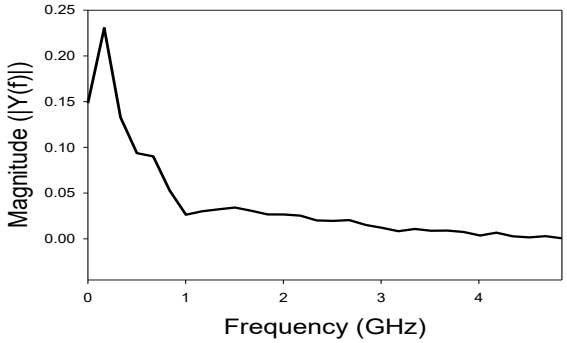

(b)

Fig. 21 Recordings of the a) FID pulse generator and b) the signal FFT [55]

To analyze the radiation pattern in the near field, the propagation of the pulse was examined (Fig. 22). Here, the antenna cross-section was oriented in the position as shown in Figure 1. This view was selected to show the electric field propagating off the conductor in the launching section. The color contour was clamped to the maximum electric field at the tip of the conical launching section (±16 V/m).

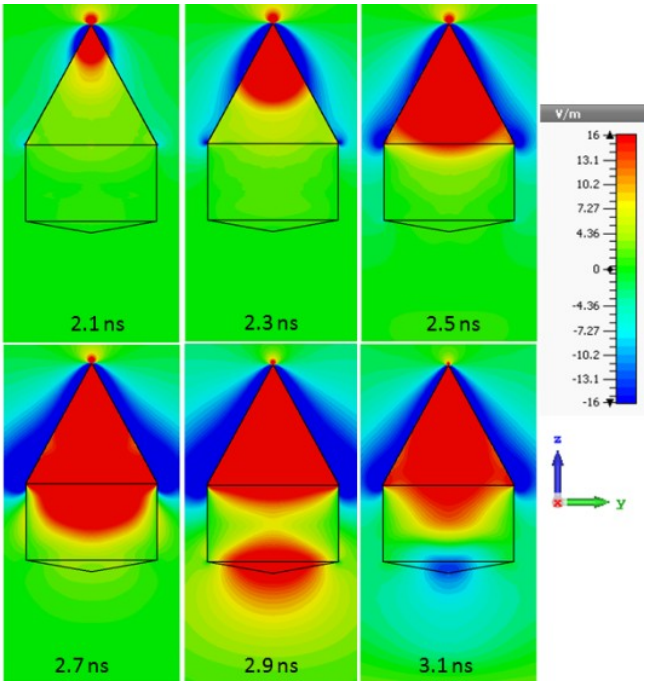

Fig. 22 Transient of the antenna in airstarting from the launching section and ending in air. Upon exiting the launching section, the spatial electric field strength (V/m) is confined to the rod. The sign of the electric field in the scale indicates the direction of the field in the y plane (+y: positive direction; -y: negative direction). [55]

At 2.1 ns, the input pulse is at the peak across the apex of the launching section and establishes a spherical wave front that propagates down the conical waveguide. The wave reaches the end of the conical emitting section at approximately 2.5 ns. At 2.7 ns, the pulse has already entered the cylindrical waveguide and the wave begins to separate from the lunching section. There is also an evanescent wave outside the rod. At 2.9 ns, the pulse has exited the antenna. Here, the wave refracts at the dielectric-air interface, the

electric field is confined to the rod cross section, and the maximum is at the tip of the conical emitting section. At 3.1 ns, there is a reversal of polarity at the tip of the emitting section. This creates a biphasic pulse in the near field.

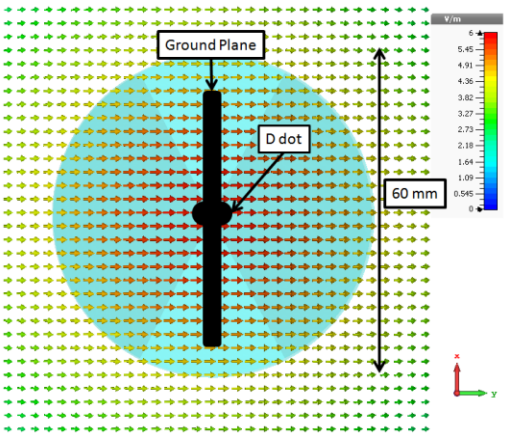

Fig. 23 Simulation of electric field measurements with a D dot probe [55]

After the wave radiates from the antenna, the electric field, at the distance of 4 cm, is shown in Figure 4. The electric field, in general, is linearly directed and is aligned in the same direction throughout the plane. Such field direction is beneficial for measurement using a linear dipole. It is also helpful for potential biological testing, since the field orientation is similar to that of the electrode-based experiments.

The radiation pattern in the far field is shown in Fig. 24. Along the x-z plane, the electric field is symmetrical about the center of the rod. There are two lobes. First is the main lobe that extends in the direction of the emitting section. Here, the peak electric field is located at 180°, the direction of the tip of the terminal emitting section. The -3 dB beam width along the main lobe is 58.8°. The side lobes are due to an evanescent wave propagating along the dielectric rod. There is also a back lobe, which is caused by the radiation directly from the wave launching section. Here, the antenna is a symmetrical radiator. The backward radiation can be prevented by adding a balun to the antenna, which was not included in the simulation. In the near field, this radiation is not as important as in the far field. The forward radiation becomes dominant. One can easily dampen the backward radiation by submerging the antenna in a medium with a high dielectric loss tangent, allowing the radiation only emitting towards the target.

Alternatively, in the y-z orientation, there is no defined lobe that extends in the direction of the emitting section. Instead, the electric field flares out to the sides. This is primarily due to the electric field along the outside of the conical wave launching section, although there are contributions from an evanescent wave. However, because of the length of the dielectric rod, there is a separation between this field and the target at the end of the emitting section. These flares aren't apparent at the tip of the emitting section in the near field.

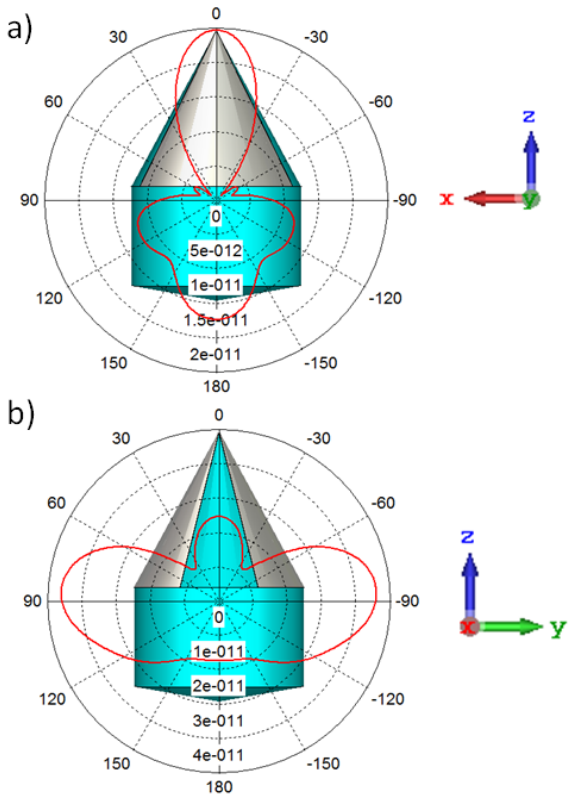

Fig. 24 The far field radiation pattern (V/m) at a distance of 1 m In (a) the x-z plane is shown and (b) shows the y-z plane. [55]

The antenna simulation was experimentally verified in both frequency and time domain. In the frequency domain, S11 was measured using a vector network analyzer (Key Sight N9926A) from 30 kHz to 4 GHz for comparison with the simulation results. A close agreement can be seen in Fig. 25. The results show that the antenna is wideband in nature. The S11 is <-5 dB for all the frequencies above 1 GHz. At frequencies of 1.73, 2.2, and 2.8 GHz, S11 is especially small. These frequencies, respectively, correspond to

the resonances that occur across the rod diameter, the height of the launching section, and the height of the combined waveguide and emitting section. It is noted that there is a strong return loss (>-5 dB) for the signals below 1.0 GHz. However, an effective antenna to radiate these low frequency components needs to be physically large, so that its geometry can be comparable to the wavelength. Using the pulse in Figure 2 as an example, which contains a peak frequency of 0.17 GHz, the diameter of a prolate spheroidal antenna needs to be 1-2 meters. Such an antenna is too large for the intended purpose, since it will create a large field distribution on the head surface. It also suffers a series of problems, as discussed in Introduction, resulting in a low field on the target. On the other hand, a dielectric rod antenna, despite its strong mismatch and low radiation efficiency at low frequency, can effectively send high frequency components to a biological target, since it also has a short distance to the target and a better coupling to the tissue. It is the high frequency components that determine the ultimate focality in the tissue. In the previous simulation results, a prolate spheroidal antenna that had a 0.5 meter diameter created a peak field of 2 V/m on the head surface when it was driven by a voltage of 1 V [21], whereas a dielectric rod antenna created a field of 28 V/m for the same driving voltage. So it is an obvious improvement. Nonetheless, the dielectric rod antenna is in general not efficient, and therefore, a high voltage source (>100 kV) has to be employed to drive the antenna in order to reach the threshold to cause biological effects.

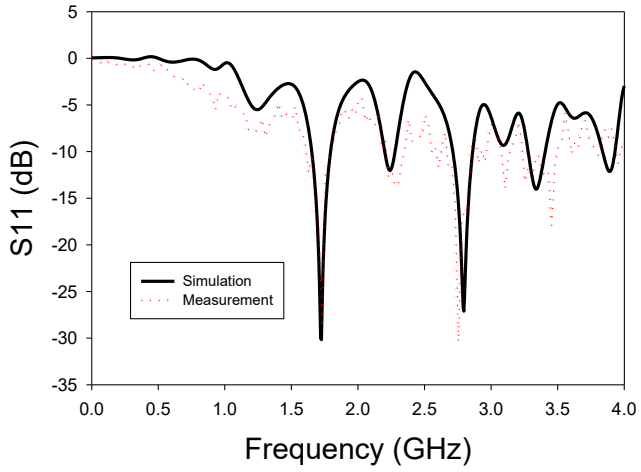

Fig. 25 Return loss (S11) of the antenna both simulated and measuredBoth show that the antenna has three major resonances at 1.73, 2.2, and 2.8 GHz. [55]

In the time domain, the electric field was measured on the axis using a Prodyn Ad-80(R) D-dot sensor with an effective area of 3×10^{-4} m. The probe elements were aligned with the center of the conical plates. The ground plane of the probe was centered at the terminal taper. The pulse was recorded at a distance of 4 cm from the tip of the launching section. The measurement in Fig. 26 shows that the pulse is primarily biphasic. The positive part of the electric field has a duration equivalent to the input pulse. Additionally, the decreasing electric field is in sync with the fall time of the input pulse. Thus, the time derivative of the input pulse is dominant.

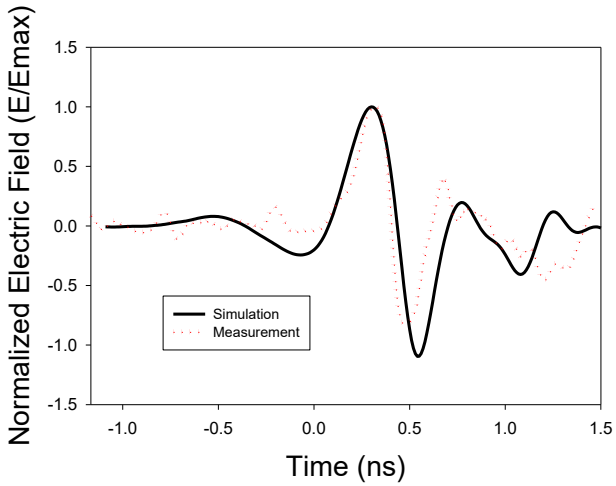

Fig. 26 Simulated and measured electric field transient at 4 cmfrom the tip of the emitting section. Both the simulated and the measured signal have the same transient. [55]

CHAPTER 3

3. DUAL RESONANCE PULSE TRANSFORMER POWER SUPPLY

To drive the biconical dielectric rod antenna requires a high voltage pulse power supply capable of reaching over 100 kV, with a pulse duration on the order of several hundred picoseconds. The general strategy for designing such a power supply relies on several distinct switching stages in which the duration of the pulse becomes compressed with each switch. It begins with a DC power supply which is switched into the microsecond time domain, usually with a voltage gain. The microsecond circuit is switched into a transfer capacitor with nanosecond charging. Finally, a peaking switch is responsible for producing picosecond pulses. Such a scheme is outlined in [56]. The critical component is the transformer that needs to constrain the charging time of the parallel-plate line to be as short as possible. This is because the peaking switch breaks down at a higher voltage for a shorter pulse application, which allows for a high-voltage transient to be fed to the antenna section.

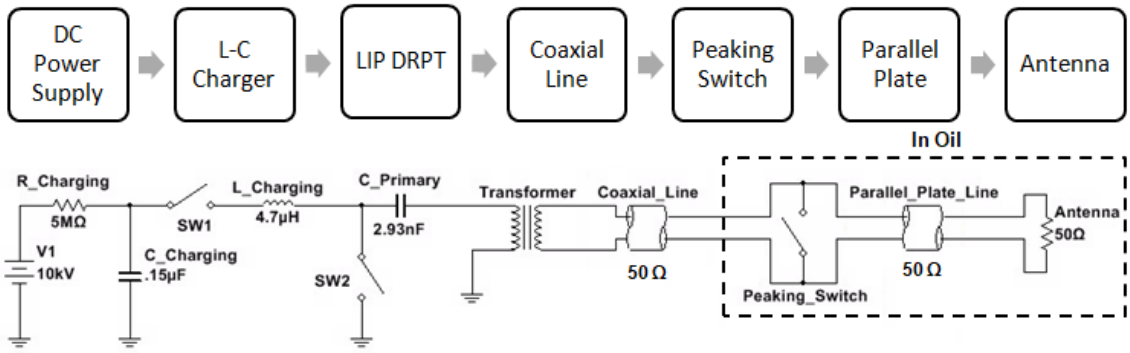

Fig. 27 Block and circuit diagram of the combined system [55]

There are three common circuit topologies for converting high voltage DC to a pulse power supply. The most common setup is the Marx Generator [57]. In this circuit, capacitors are charged in parallel and are discharged in series though a spark gap switch. The result is a gain which is equal to the number of capacitor stages. However, the challenge with this design is that it requires the synchronization of many spark gap switches. These switches are prone to misfiring and have a limited lifetime. Additionally, the repetition rate of the Marx Generator is limited by the recovery time of all of the switches. A lesser known circuit is the Vector Inversion Generator. This circuit consists of a rolled parallel plate transmission line

with a single switch across one of the transmission lines. When the switch closes, the electric field vector across the fast transmission line reverses orientation, leading to a gain proportionate to the number to turns. The result is a triangular pulse. While the Vector Inversion Generator has been used to create oscillations in the radio frequency range [58], it has not yet been utilized to create picosecond-pulsed power supplies. The final type of pulse generator is the air core dual resonance pulse transformer (DRPT). DRPTs are used in charging capacitive loads such as pulse forming lines. Free from saturation, and linear in performance, they have applications in very high voltage modulators as well as in electron and ion beam accelerators. DRPTs are low cost, compact, and simple to build. They require only one switch for operation, and they can be constructed into the megavolt range [59]. They have been used to charge an ultra-wideband radiator and create picosecond pulses for high power impulse radiation [56].

In this chapter, a DRPT system which charges in the biconical dielectric rod antenna will be demonstrated. The significance of the transformer is that it charges in the nanosecond time domain. By having the transformer charge in nanoseconds, the transfer switch, which is present in slower transformers [56], can be removed from the system. In addition, a faster transformer has implications for the system construction. The dielectric strength of materials increases with a decreasing pulse width. This allows for a fast DRPT to have reduced insulation and even operation in air, whereas a slower DRPT would have to be submerged in dielectric-insulating oil. Finally, the transformer will be integrated with the antenna through a parallel plate transmission line with an integrated peaking switch. The antenna's electric field will be recorded in air.

3.1 THE DUAL RESONANCE CIRCUIT

A DRPT's circuit topology consists of a primary capacitor C_1, a primary inductor L_1, a secondary capacitor C_2, and a secondary inductor L_2. The two inductors are coupled, in order to produce a step-up in voltage. The circuit begins with a DC power supply which charges C_1. When the switch is closed, it produces a step voltage, represented by V/s in the Laplace domain. There is an LC resonance that occurs in the primary circuit, which is passed to the secondary circuit. The general schematic can be seen in Fig. 28.

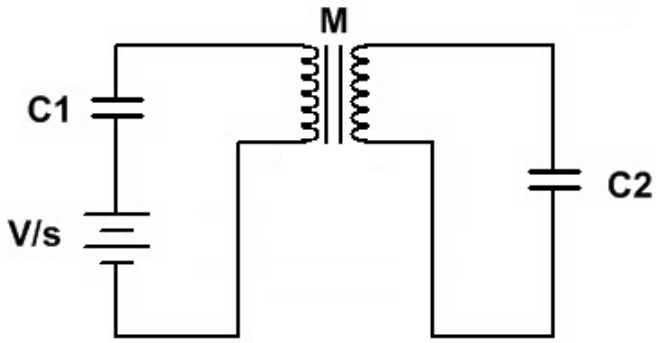

Fig. 28. The DRPT circuit model in the Laplace domain [60]

Critical to the operation of the circuit is the dual resonance condition. It says that the product of the primary values must equal that of the secondary values ($L_1C_1 = L_2C_2$). This ensures that the two discrete circuits resonate in sync. The gain, or the maximum value of the voltage, is described by the square root of the ratio of the inductance or capacitor values [61]:

$$\frac{V_o}{V} = \sqrt{\frac{L_2}{L_1}} = \sqrt{\frac{C_1}{C_2}} \tag{11}$$

For DRPTs, this is considered to be an estimate. The gain presented is for the ideal case, where the transformer is both perfectly resonant and has no resistive losses or losses in magnetic flux. In a slow-charging resonance frequency system, it is possible to achieve a voltage gain of $0.9\sqrt{\frac{L_2}{L_1}}$ [62]. However, it is unlikely to have gain of $0.9\sqrt{\frac{L_2}{L_1}}$ in an ultrafast low inductance system. A gain of (0.6-0.7) $\sqrt{\frac{L_2}{L_1}}$ was considered realistic for this setup.

While the air core transformer (and, by extension, the DRPT) has no frequency limitations (i.e., any pulse length is theoretically possible), it is not used widely in the sub-microsecond range. This is because of design tradeoffs inherent in the dual resonance mode. In order to get a faster pulse for a realistic load capacitance (and maintain the gain), the transformer inductances must become smaller. To achieve a pulse rise time under 100 ns, our primary inductance needed to be <100 nH. At this value, excess inductance present in the capacitor bank, connecting wire, and switch preceding the primary winding made the design

difficult. This is because the inductance in the primary circuit was no longer dominated by the inductor L_1. The stray inductance L_{stray} is on the same order as L_1; it reduces the gain and disrupts the resonance characteristics. The primary method of mitigating the effect L_{stray} is by using novel geometries to create low inductance paths. One such geometry has been a super low inductance primary ring [61]. This design was able to produce an uncoupled resonant frequency of 2.01 MHz and a pulse rise time of 200 ns [61]. By employing a linearly integrated primary (LIP), we created a compact geometry that features a low inductance capacitor bank and low inductance paths.

The discrete circuit model is practical and is accurate for describing the operation of the DRPT. The equivalent circuit can be seen in Fig. 28. In order to describe the temporal evolution, the ideal dual resonant case is presented. This neglects any losses due to the resistance of the coil windings and assumes a zero inductance path. The capacitors in the primary have no equivalent series inductance and are connected by ideal wires. The only inductance present in the circuit is contained in L_1 and L_2.

By applying Kirchhoff's voltage law, the time evolution of the voltage across the load capacitor C_2 can be described [63].

$$V_o = \frac{Vk}{C_2\sqrt{L_1L_2}}\frac{\cos(\omega_b t)-\cos(\omega_a t)}{\omega_a^2-\omega_b^2} \tag{12}$$

where $\omega_a^2, \omega_b^2 = \frac{1}{2(1-k^2)}\left(\frac{1}{L_1C_1}+\frac{1}{L_2C_2}\right) \pm \frac{1}{2(1-k^2)}\sqrt{\left(\frac{1}{L_1C_1}+\frac{1}{L_2C_2}\right)^2 - \frac{4(1-k^2)}{L_1C_1L_2C_2}}$ and $k = \frac{M}{\sqrt{L_1L_2}}$.

The resulting waveform is determined by the difference between the oscillations in the primary and secondary circuits [63]. The optimal coupling coefficient, k, is determined by $k_n = \frac{2n-1}{2n^2-2n+1}$ where n is a positive integer representing the sequential voltage excursion [64]. Because the first voltage swing (n=1, k =1) will not reach the maximum in the air core transformer due to poor coupling, the maximum voltage is seen on the second voltage excursion (n = 2, k = 0.6). Tuning k is done by controlling the magnetic flux between the primary and secondary. This is strongly influenced by the distance between the coils.

A more practical method can be used to the design the desired waveform. This is done by focusing on the times of the first and second voltage peaks and the maximum theoretical gain. The location of the first and second voltage peak are [62]:

$$\tau_1 = \frac{\pi\omega}{2} \text{ and } \tau_2 = \frac{3\pi\omega}{2} \quad (13)$$

where ω is the uncoupled resonant frequency in the dual resonant mode $\left(\omega = \frac{1}{\sqrt{L_1 C_1}} = \right.$ *1L2C2*.

3.2 AN ULTRAFAST CHARGE TIME PULSE TRANSFORMER

The design criteria for this system is a desired uncoupled resonant frequency of 8 MHz, a maximum theoretical gain of 5.75 V/V, and a capacitive load of 200 pF. Applying these criteria, combined with values of off-the-shelf capacitors and the dual resonance condition, the discrete circuit values seen in Table 1 were produced. This is the basis for the construction of the system.

Table 1. Design parameters for an 8 MHz resonance frequency

Component	Value
C1	6.6 nF
L1	60 nH
L2	2 μH
C2	200 pF

To confirm the analytical analysis, a transient analysis was conducted using a SPICE program (National Instrument's Multisim). The circuit is shown in Fig. 29. This circuit adds parasitic effects not seen in the ideal model (Fig. 28). The additional inductors in this circuit represent L_{stray}. The source of this inductance comes from estimated equivalent series inductance of the capacitor bank, spark gap, and connecting wire in the circuitry. The resistances were numerical estimates of the copper plates used to connect components and the wire used to form the inductors.

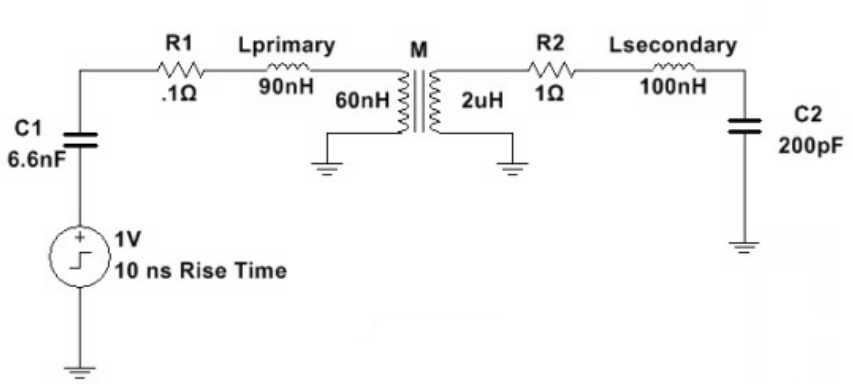

Fig. 29 Distributed circuit model with parasitic components [60]

The application of a 1 V peak, 10 ns rise time step function represents the discharge of a charged capacitor in the Laplace domain. This simulation produced the transient voltage across the load capacitor shown in Fig. 30. It shows dual resonance with the peak voltage on the second voltage swing. There was a gain of 3.37 V/V and a pulse rise time of 67 ns. The rise time is defined as the time between first negative peak and the first positive peak.

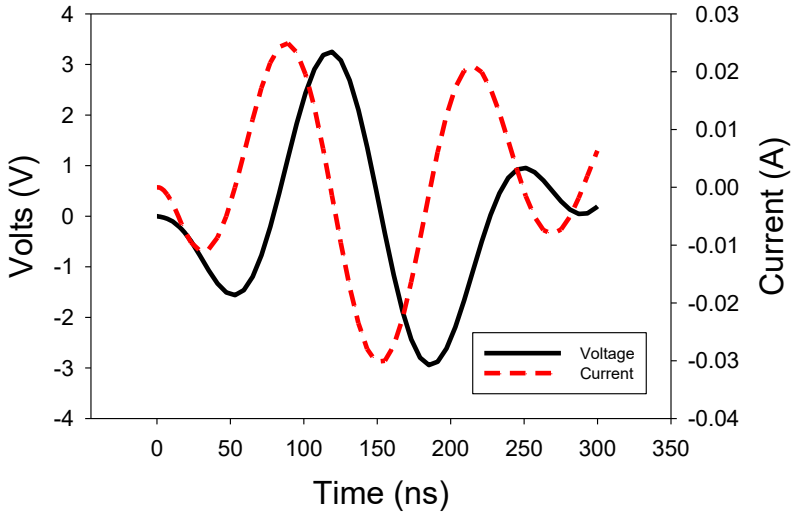

Fig. 30 SPICE model transient results of secondary voltage and current [60]

Additional modeling was done using CST Microwave Studio in order to incorporate the physical design. A transient solver using a co-simulation of both ideal

circuit elements and 3D models was used to combine the circuit models of the capacitors and power supply with a physical model of the primary and secondary inductor.

For DRPTs, there are two typical constructions. First is the spiral-strip transformer pioneered by Rohewin [59]. It consists of a single strip for the primary and multiple concentric strips for the secondary. The type is the helical wire/strip transformer [62]. This the type presented here. In this design, the primary (made of conductive strips) is wound around the secondary (made of wires). The secondary inductor is then seated inside the primary. It differs from the former type of transformer in the type of insulation used. Fig. 31 demonstrates this concept and shows the hybrid setup. The figure shows a voltage supply (the yellow block) in series with the capacitor bank and the transformer primary. Out of the transformer block, there is a port (P1) to record the response at the secondary. This is in series with the load capacitor and ground.

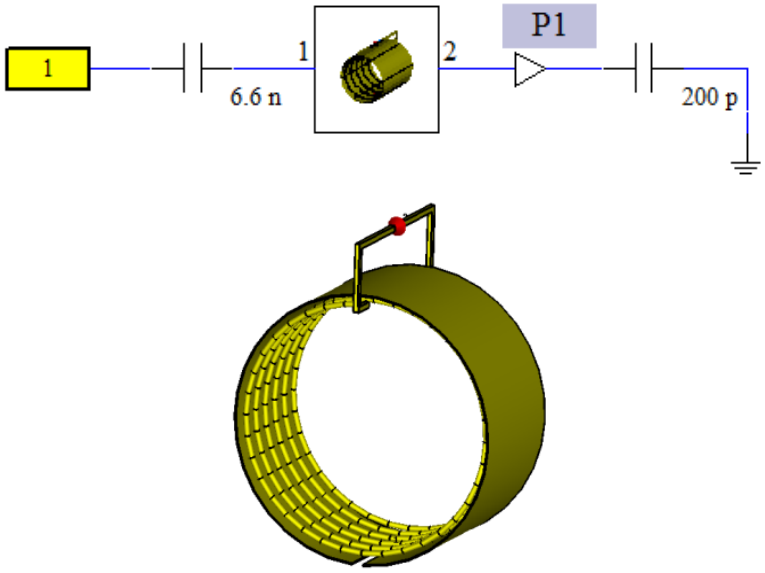

Fig. 31 CST hybrid simulation of the transformer and circuit elements [60]

Two transformers, one for low voltage (a few kV) and one for high voltage (~100 kV), were constructed and were simulated in the modeling environment. The geometry of the primary (approximately 66 nH) was designed using self-inductance formulas for a single-layer circular coil [65]. The geometry of the secondary (2 μH) was done using the formula for the self-inductance of a wire solenoid:

$$L = \frac{\mu_0 N^2 A}{l} \qquad (14)$$

where μ_0 is the permittivity of free space, N is the number of turns, A is the cross sectional area, and l is the length. The electrical properties of all of the model components were consistent with copper ($\sigma = 5.8 \times 10^7$ S/m, $\mu = 1$). See Fig. 32 for the model cross section and Table 2 for a summary of the design geometry.

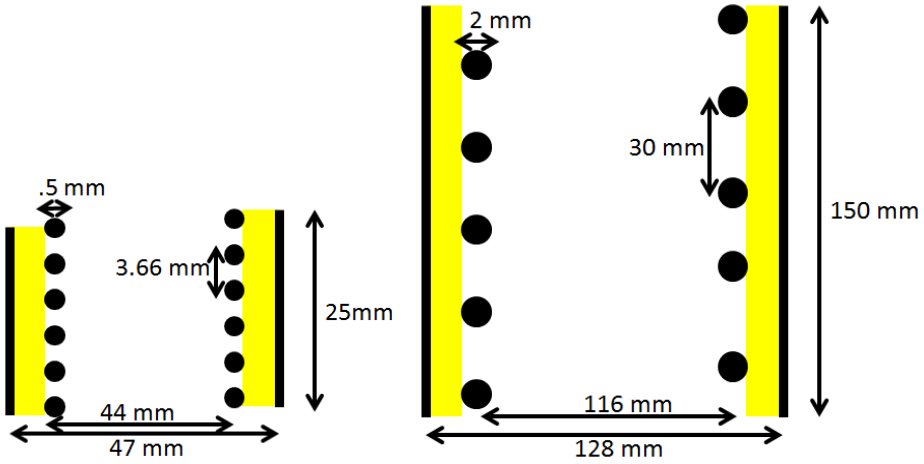

Fig. 32 Cross section of the a) low voltage and b) high voltage transformer [60]

Table 2. Summary of the 3-D model design geometry

Component	Low Voltage	High Voltage
Turns (N)	6	5
Primary Radius (mm)	23.5	64
Sheet Thickness (mm)	.2	.5
Secondary Radius (mm)	22	58
Wire Radius (mm)	.25	1
Height (mm)	25	150

For both low voltage and high voltage models, the primary capacitor bank (6.6 nF) was made to be non-ideal with a series resistance of 0.1 ohm and series inductance of

90 nH. Similarly, the secondary capacitor was non-ideal with a series resistance of 1 ohm and a series inductance of 100 nH.

By applying a voltage to the primary capacitor bank (Fig. 31), the model could be simulated. In both the low voltage and high voltage scenarios, the applied voltage was a 1 V peak, 10 ns rise time step function. The voltage and current across the primary inductor and the secondary capacitors for the high voltage transformer are seen in Fig. 33.

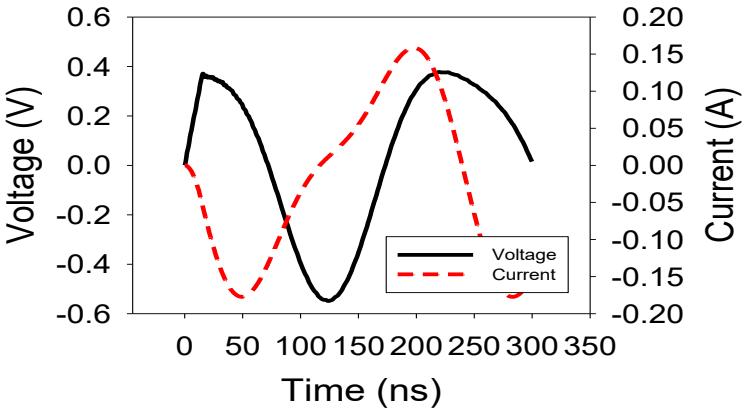

(a)

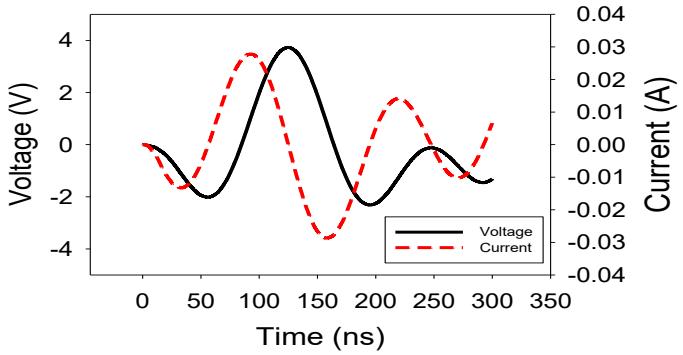

(b)

Fig. 33 Simulated voltage and current across the (a) primary and (b) secondary [60]

Both models showed a dual resonant response with qualitative and quantitative features similar to the discrete circuit model. In the low voltage scenario, the simulation yielded a voltage gain of 3.46 V/V and a pulse rise time of 58.1 ns. The high voltage simulation showed a gain of 3.73 and a pulse rise time of 68.8 ns. The slight differences

in gain and rise time can be attributed to the estimates of self-inductance and the differences in the coupling. Overall, the results of the simulation reiterated the conclusions of the SPICE model and gave credibility to the design geometries.

The spatial distributions of electric fields and current density are shown in Fig. 34 and Fig. 35. These results were obtained using the parameters for the high voltage transformer (Fig. 32 b). The electric field and current density were clamped at 20 V/m and 1A/m respectively, meaning that any value higher would be shown with the same color (in this case, red). In the side view, the electric field is mostly confined between the primary and secondary winding. The field in the center section of the winding, however, is generally lower than that in the bottom and top sections. At 80 ns, the voltage across the second winding is close to zero, resulting in a small electric field distribution throughout the transformer. This is similar to the moment of 20 ns, at which the primary pulse just starts. At 120 ns, the field reaches the maximum, which corresponds to the peak voltage of the secondary winding. This is consistent with the top view of the transformer, in which the field across the secondary winding can be better seen by the size of the red circle on the top of the transformer. The field is lower at 80 ns but reaches its peak at 120 ns. In a resonance phenomenon, the electrical energy is converted to magnetic energy or vice versa in a periodic fashion. An efficient transfer of energy occurs when the magnetic energy reaches its minimum while the electric energy simultaneously reaches its maximum. In Fig. 35, this can be clearly seen in the minimal current distribution at 120 ns, at which the secondary voltage reaches its peak.

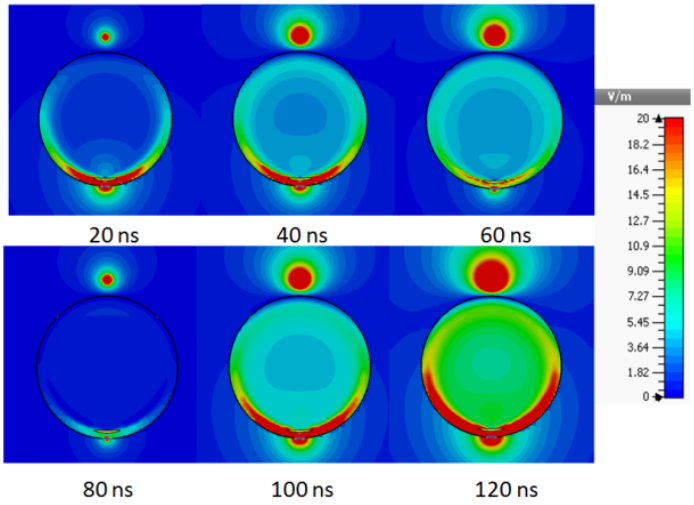

Fig. 34 Electric field transient across the transformer [60]

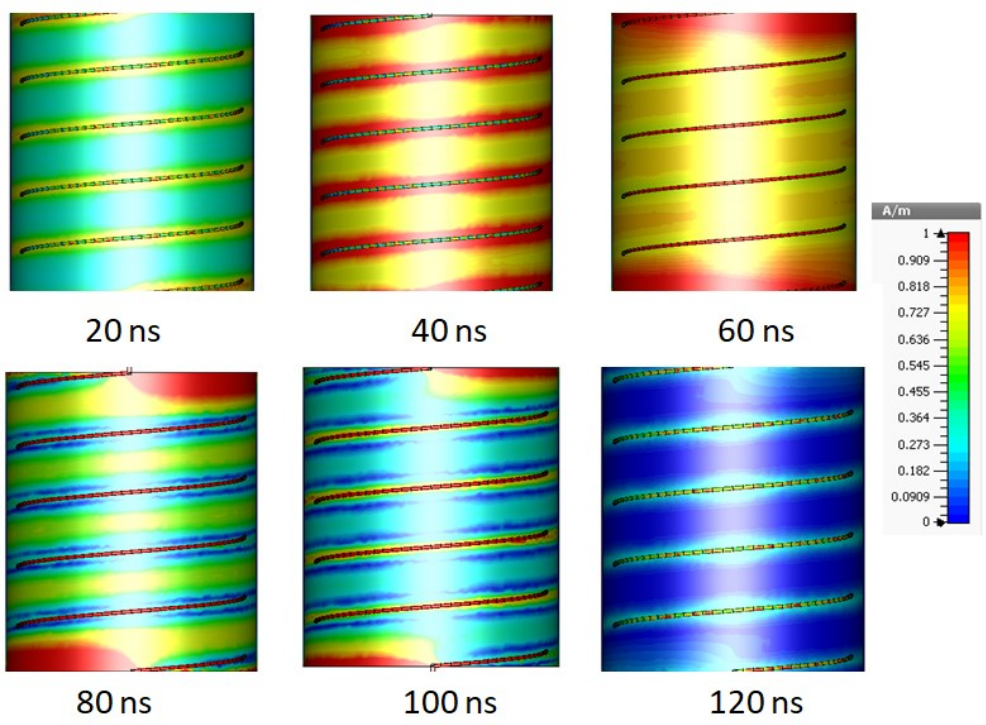

Fig. 35 Surface current distribution along the transformer windings

The DRPT was fabricated using the geometries from the CST simulation. Six turns of 1 mm diameter magnet wire were made around a PVC pipe to form the secondary winding. A sheet of polyethylene was wrapped around the secondary in order to create the desired 1.5 mm radial separation of the coils and to insulate the primary winding from the secondary. A copper strip wound around the polyethylene sheet formed the primary winding.

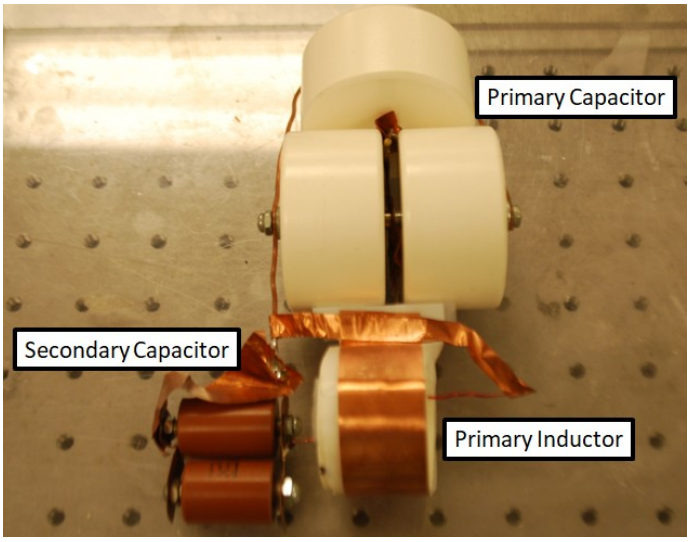

Fig. 36 Low voltage DRPT construction

The primary capacitor bank was assembled from three 2 nF capacitors (N4700, Murata) connected in parallel and directly connected to the primary winding. Since not all of the capacitors could be directly connected to the primary forming the LIP, it was important to make the design as compact as possible, in order to reduce stray inductance. The secondary capacitor comprised two 100 pF capacitors (UHV-251A, TDK) wired in parallel. This totaled 200 pF. Once fully charged, shorting the potential capacitor terminal and the primary winding produced the voltage on the secondary capacitor. For the charging voltage of 1 kV, the peak output was 3.24 kV with a rise time of 70 ns. See Fig. 37.

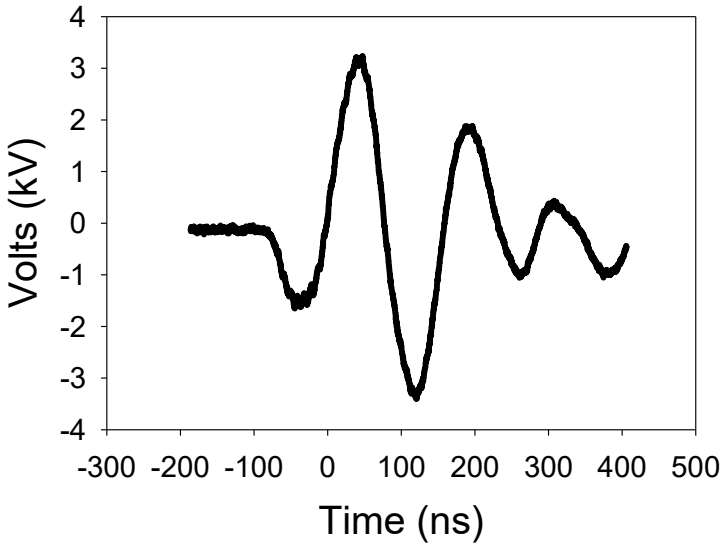

Fig. 37 Low voltage DRPT transient with a 3 kV output

Scaling up the operating voltage of the air core transformer was done by increasing the dimensions and adding extra insulation between the secondary and primary windings. The dimensions of the windings can be found in Figure 5 and in Table 2; however, there were some differences in materials. The primary winding in this case is made of stainless steel foil with a thickness of 0.2 mm. The secondary winding was formed from solid copper 2.05 mm diameter (12 gauge) wire, wound around a PVC pipe in a spiral fashion. Between the windings, a 1 mm thick Teflon sheet was wound in several layers to provide a total of 6 mm of separation and insulation. The load was formed out of a capacitor array (N4700, Murata) with a total capacitance of 200 pF. Finally, the coupling coefficient was estimated by measuring the self-inductance of the primary coil when the secondary coil was both shorted and not present. As a result, the coupling coefficient (k) was determined to be 0.54.

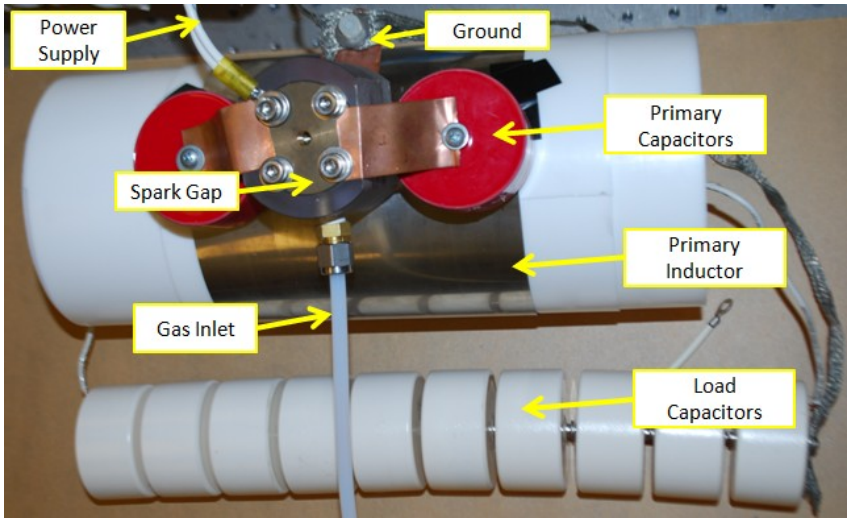

Fig. 38 High voltage DRPT construction with the LIP [60]

A salient feature of our design lies in the placement of the capacitor bank and a self-closing switch. The 3.3 nF primary capacitors (40DKD33,Vishay) and the pressurized self-breakdown switch were aligned so that they linearly integrated to the primary coil (LIP) and became part of the single-turn coil. Using this configuration, the capacitors could discharge through a common current path while minimizing the stray inductance. See Fig. 38 for the actual setup.

To charge the primary capacitor bank up to 40 kV without strict insulation in air, a resonant charging circuit was constructed with a 4.7 μH charging inductor, a 128 nF capacitor (Model 31261, Maxwell) and a mechanical switch. Due to the increased voltage in the primary capacitors, the voltage across the primary self-breakdown switch reached the breakdown value and the transfer of the energy from the primary to the secondary capacitor occurred.

To characterize the performance of the transformer, several measurements were conducted. Voltage across the spark gap in the primary winding was measured with a high voltage probe (P6015a, Tektronix). Its breakdown voltage was regarded as the initial voltage of the primary capacitor. In the secondary winding, the voltage was measured across two of the ten capacitors used to form the array using the other probe (P6015a, Tektronix). In doing so, the observed voltage was scaled down by a factor of five because of the series connection. As a result, we were able to use our voltage probe (rated for 40 kV pulse conditions). The secondary current was measured using a Pearson coil (Model

2878). All of these measurements were conducted simultaneously, and the results were recorded in a 4-channel oscilloscope (TDS3054C, Tektronix). The primary current was not measured by the Pearson coil due to the lack of space between the capacitor bank and coil. Adding such space would have added extra inductance to the current path. Figure 10 shows typical waveforms for the primary voltage, secondary voltage, and secondary current. It also shows the relation between the charging voltage of the primary capacitor and the peak of the secondary voltage.

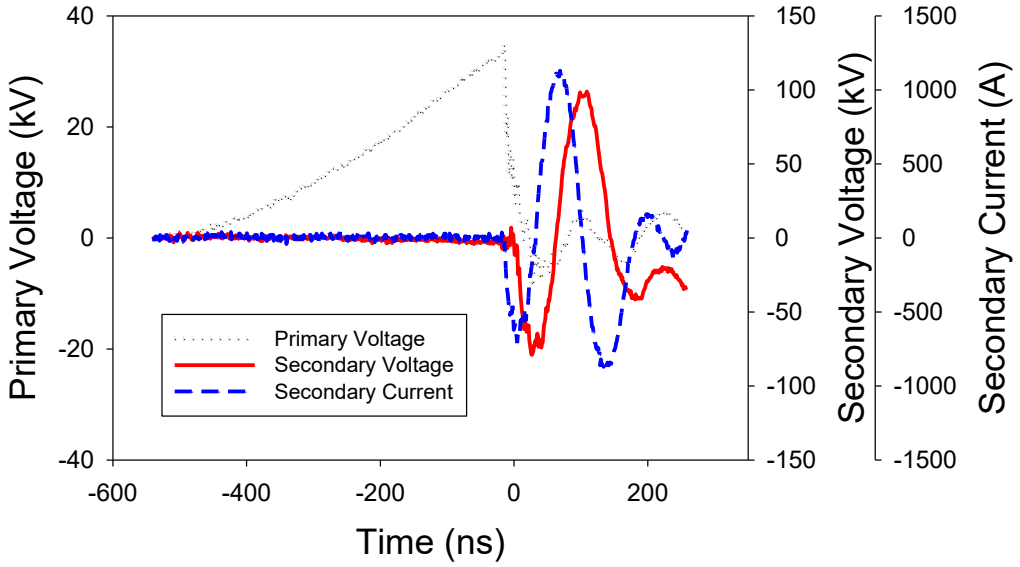

Fig. 39 Typical DRPT output showing 100 kV charging [60]

The primary voltage was tested from 11.8 kV to 41.2 kV (which is the maximum capacitor rating). This sweep of primary voltages produced approximately linearly increasing secondary voltages from 47 kV to 124 kV. This represents a range of voltage gains between 3 and 3.98, with the average gain over the set of pulses in Fig. 40 being 3.38 V/V, which correspond to an energy transfer efficiency of approximately 27%-54%.

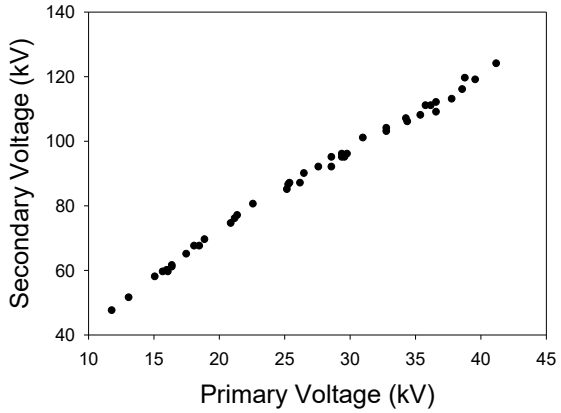

Fig. 40 The linearity of gain in the DRPT. The minimum output is 45 kV and the maximum is 130 kV. [60]

A discrete circuit model (Multisim) and a discrete circuit-electromagnetic hybrid model (CST model) were applied to design an ultrafast air core transformer. The starting point of these models was an ideal, uncoupled dual resonance model, which sets the fundamental parameters for the LC network, taking the resonance period into account. The performances rendered by these two approaches are summarized in Table 3.

Table 3. Summary of DRPT results

Method	Gain (V/V)	Rise Time (ns)
Multisim	3.37	67
CST Low Voltage	3.46	58.1
CST High Voltage	3.73	68.8
Measured Low Voltage	3.24	70
Measured High Voltage	3.38	70

Both the Multisim model and the CST model closely predict the results in voltage gain and pulse rise times seen in the experimental results. Each of the simulations brought its own advantages. The Multisim model offered rapid design capabilities and a flexibility of adjusting the stray parameters to reflect the physical model, whereas the CST model provided a remarkably accurate guide for the construction of the DRPT as well as insight into the real electromagnetic field distribution (in addition to lumped voltage and current).

Dual resonance was shown in both Multisim model and the CST model. The primary feature was the conversion of the electrical energy stored in the capacitor to the magnetic energy stored in the transformer. The manifestation was the voltage and current in the secondary winding: when the current reached its maximum, the voltage became its minimum. See Fig. 33. The alternating dominance of these two energies formed the basis of the dual resonance.

It should be noted that presence of dual resonance did not necessarily ensure maximum gain or energy transfer. In fast charging systems, the gain is strongly dependent ability of the primary circuit to transfer charge stored in C_1 into current across L_1. In an ideal LC circuit, such as that shown in Fig. 28, all of the charge stored in the capacitor is transferred to the magnetic field in the inductor. However, when L_{stray} is on the same order as L_1, much of the initial charge is stored in the capacitor is transferred to L_{stray}. This magnetic field never becomes part of the transformer and the energy is permanently lost. Some evidence of this can be seen in Fig. 33. The voltage and current in the primary contain an additional frequency component causing a distortion in the sinusoidal resonance. As a result, in low inductance primary DRPTs, the gain is highly sensitive to changes in L_{stray}. While the LIP has the lowest inductance path to date, small changes in L_{stray} can significantly improve the gain and can possibly allow for the construction of faster charging systems.

The energy transfer from the primary to the secondary winding is determined by the coupling coefficient (see (1)). This geometry was under-coupled, meaning $k < 0.6$, yet the system still exhibited both gain and dual resonance. This will be the case in all DRPTs with $k < 0.8$, suggesting high process latitude [61]. However, having a $k < 0.6$ means that the energy transfer efficiency is sacrificed. The physical explanation for this is

that the primary capacitor is not completely discharged at the instant of maximum secondary potential [66]. In slower systems, one can add a tuning inductor to experimentally correct of mismatches in k. In fast charging systems, this becomes difficult. There are both little room to add such an inductor, due to the compact nature of the LIP, and negative effects of extra inductance, such as a reduced pulse rise time.

One inherent loss to a helical strip/wire DRPT is caused by the inhomogeneous current distribution in the primary winding (shown from 20 ns to 120 ns in Figure 8 for example), which reduces the magnetic coupling between the primary and secondary windings. The current is concentrated mostly on the edges of the thin sheet, which introduces extra distributed inductance. On the other hand, the eddy current produces a magnetic flux that does not contribute to the total flux linkage across the secondary winding. This is the major drawback of the coaxial air core transformer, in which a wide thin sheet is used as the primary winding.

With the same Multisim circuit model, we were able to construct two transformers designed to operate at low voltage and at high voltage. While the two transformers' voltage gains and rise times are close, problems arise as the geometry and voltage increase. In Fig. 40, noticeable voltage losses started to occur as the primary voltage increased. When the primary voltage was 11.8 kV, the voltage gain is 3.98, but it decreased to 3.0 when the primary voltage was 41.2 kV. One explanation for this is the corona discharge occurs at the sharp edges of the top and bottom section due to the field enhancement, which acts as a resistive and capacitive network that crosses the gap between primary winding and secondary winding. Interestingly, these extra components did not show up in any of the models that were applied. Nor could they be characterized when we measured the inductances, coupling coefficient, etc. One way to overcome this problem would be to submerge the transformer in oil. Another way would be to smooth the electric field at the edges of the primary winding by adding a thicker conductor. While there can be several improvements, our results show that an air core transformer capable of >100 kV outputs while having a <100 ns rise time charging is possible, even when it is exposed in air.

A design for a helical strip/wire DRPT with an ultrafast rising pulse time and an ultra-low inductance path utilizing a linearly integrated primary (LIP) was presented. The

transformer was first designed in a discrete circuit model and then in a hybrid model which contains the physical model as well as the discrete excitation. The results showed very close agreement. The implementation of the physical model allowed us to construct a transformer that has a rising pulse time of 70 ns and gain of 3.38. Our result also shows that a 100 kV air core transformer can work in air without oil insulation. Extra care, however, needs to be taken for higher voltages.

3.3 OTHER PULSE TRANSFORMER CONSTRUCTION

Using the techniques which were previously outlined, it is possible to construct a variety of DRPTs. Some of the transformers which have been constructed can be seen in Fig. 41. The output voltages of the DRPTs go as 250 kV, 70 kV, and 100 kV with charge times of 1.5 μs, 1 μs, and 10 ns, from left to right. In general, as the charging time decreases, the gain (and thus the output voltage) increases. Additionally, the more compact the transformer, the lower peak voltage it can withstand.

Fig. 41 Dual resonance pulse transformer designs

In the initial transformer construction, the pulse initiation was done by an un-triggered spark gap switch. This is not an ideal technique, because it causes variation in the peak of the output pulse. Any variation in the first spark gap has an impact on the peaking switch which could produce premature closing or no closing at all. This is especially so for high gain transformers, since the voltage difference between subsequent

shots can be large. To mitigate this effect, a trigatron can be implemented in the primary stage. The circuit diagram can be seen in Fig. 42.

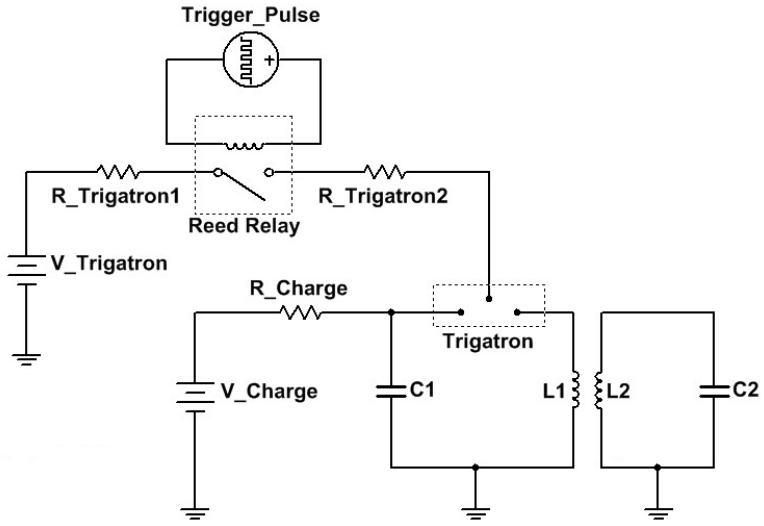

Fig. 42 Integration of a trigatron into the DRPT system

The trigatron acts as a spark gap triggered spark gap. When the high voltage Reed Relay closes, it creates a high voltage (~5 kV) pulse on the order of 20 ms. This ionizes the air within the trigatron and it allows the main spark gap switch, which is between C_1 and $L_{1,}$ to close.

3.4 COMBINED ANTENNA AND TRANSFORMER SYSTEM

Now that the the pulse power supply has been constructed, it can now be integrated with the biconical antenna. When V_o from the LIP DRPT, which also is the voltage of the transmission line, reaches the second peak, whose magnitude is the largest among all the peaks, the peaking switch closes and a fast transient is then delivered to the dielectric rod antenna to be radiated. The magnitude of the fast transient is half of V_o according to transmission line theory [33]. Having a fast rising V_o pulse is crucial for operating the peaking switch, as the voltage jitter is low when the pulse application time is short. To achieve the fast pulse condition, the primary winding was only made in a single turn but also incorporated the primary capacitor bank and switching into the primary coil. In this way, the single turn discharged through a low inductance, common current path. Keeping the stray inductance to a minimum is critical for maintaining the efficiency of the gain [61].

The primary capacitor bank ($C_{primary}$) was charged by a LC resonance circuit ($L_{charging}$ and $C_{charging}$), in which $L_{charging}$ was a 4.7 μH inductor, and $C_{charging}$ consisting of two 0.3 μF, 45 kV capacitors (37058, Maxwell) in series with a total capacitance of 0.15 μF. A 50 MΩ charging resistor was used to charge $C_{charging}$, which was isolated from $L_{charging}$ by a mechanical switch (SW1). Upon closing the mechanical switch, the primary capacitor bank ($C_{primary}$) was charged through the primary winding of the transformer.

$C_{primary}$ was made up of three 3.3 nF (40DKE33, Vishay) and one 2 nF (N4700, Murata) capacitors, where each was rated for 40 kV. Having two connected in series as a stack and having two stacks combined in parallel accounted for a total capacitance of 2.90 nF and a rated DC charging voltage of 80 kV.

To maintain the resonance condition ($L_1C_1 = L_2C_2$) the capacitance of the secondary was 95.5 pF. A RG 217-U coaxial cable with a capacitance of 101.05 pF/m was used as the secondary capacitor. The length of 0.945 m corresponded to the desired 95.5 pF capacitance, which also provided separation and isolation between the transformer and the antenna, which allowed us to perform electric field measurements in the antenna's near field.

The LIP was completed by incorporating the switch into the primary coil. The switch was an adjustable spark gap charged with nitrogen to 100 psi in order to withstand a ~15 kV charging voltage.

The connection from the coaxial cable to the antenna was made by a parallel plate transmission line immersed in insulating oil. The oil was a severely hydrotreated napthenic oil (Flu-tran Type II, Fluids Inc.). The line was constructed with stainless steel plates with a width of 13.77 mm, a length of 152 mm, and a separation of 3 mm. This represented a line impedance of 50 Ω and a capacitance of 16.7 pF. An acrylic holder (ε_r = 2.7) was manufactured to separate the two plates.

The picosecond transients were generated by a peaking switch. This was integrated into the parallel plate transmission line. Its geometry can be seen in Fig. 43. The gap between the electrodes was adjustable and was set to a distance of 0.3 mm.

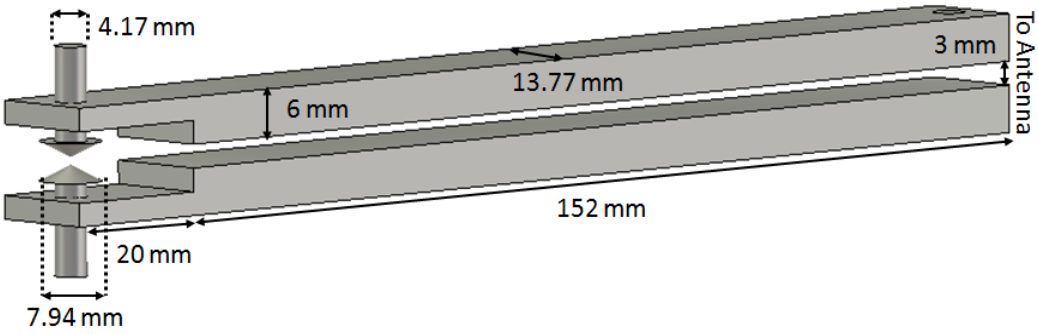

Fig. 43 The parallel plate transmission line with integrated peaking switch**.** [55]

The entire system that included the antenna and the pulsed power system was tested. The slower part of the system (prior to the coaxial line) was housed in a Faraday cage. The fast part of the faster system (strip line, peaking switch and antenna) was immersed in an oil vessel. The coaxial cable (95.5 pF) connected the slow system to the fast one. It should be noted that, upon closing the peaking switch, the picosecond transient that is fed to the antenna only had half of the of the breakdown voltage, which was equal to half of the transformer's secondary voltage.

The electric field was measured under the oil vessel on the axis using the Prodyn D-dot sensor (AD-80R). The biconical part, which is the sensing element of D-dot, was aligned with the center of the conical plates. The measurement was taken at a distance of 4 cm as measured from the conical part to the antenna tip. See Fig. 44 for the measurement setup.

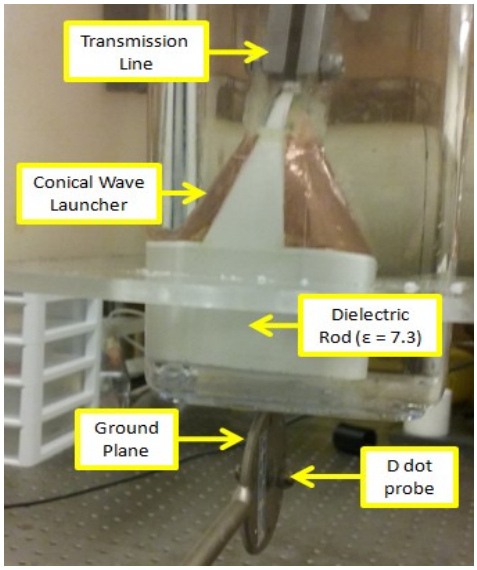

Fig. 44 Measurement setup of the combined antenna and transformer system in the near field. The antenna, including the conical wave launcher and the dielectric rod, was immersed in transformer oil. The transmission line was also immersed in the same oil container. Below the container, a dot probe was placed to measure the radiated field. [55]

Typical traces of the power supply voltage are shown in Fig. 45. The first trace shows the voltage across the spark gap in the primary winding. The second shows the voltage at the terminus of the secondary coaxial cable, just prior to the peaking switch. Both measurements were recorded using Tektronix P6015a high voltage probes. The last trace is a measure of dV/dt in free space from a D-dot sensor. All of the voltage measurements were recorded simultaneously on a Tektronix M505204 oscilloscope.

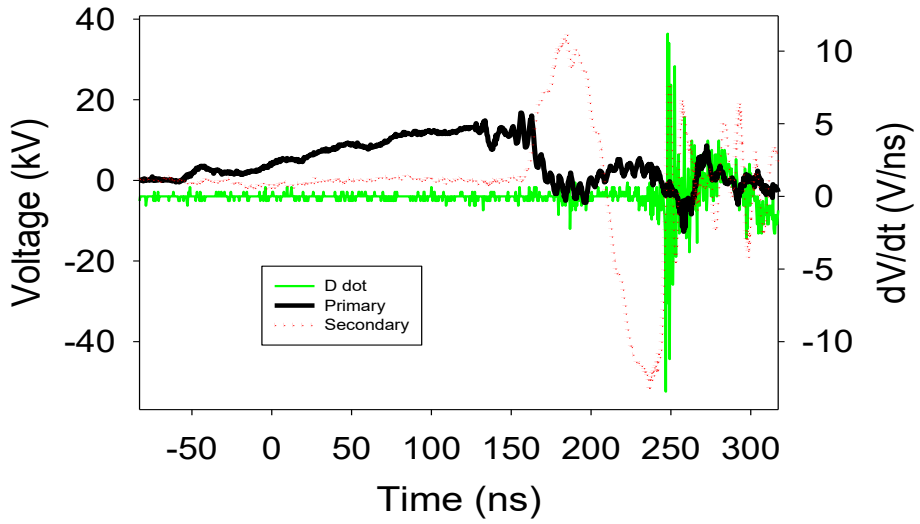

Fig. 45 Measured voltages of the combined system.After charging the primary capacitor (black), the first spark gap closes initiating the transformer response (red). The peaking switch closes near the maximum of the second voltage cycle, which is shown by the sudden drop in voltage in the secondary. This induces a fast transient in the D dot probe (green). [55]

The primary voltage trace shows a slow charging which culminates in a closing of the spark gap switch (SW2) at 165 ns. The peak charging voltage in the primary was 15.8 kV. The secondary exhibits the typical dual resonance pattern with the peak voltage on the second voltage swing. The peak voltage in the secondary is -52.4 kV. This indicates a voltage gain of 3.32 V/V. The peak-to-peak time in the secondary is 48 ns. The secondary peak voltage breaks down in the peaking switch and the transients are fed to the antenna for radiation.

Another view of the D dot signal is shown in Fig. 46, which was plotted on a shorter time scale. The recording shows a pulse waveform with a rise time of 510 ps and an amplitude of 617 V/cm. The full width at half maximum was 400 ps. It should be noted that the waveform is monopolar without a significant reversal in polarity. This is preferable for applications to biological samples, since bipolar picosecond pulses may cause cancellation of the bioelectric effects which have been shown for nanosecond pulses [67].

As previously stated, the voltage transient that drives the antenna was only half the voltage in Fig. 45, which is 26.2 kV. This results in an electric field of 617 V/cm. On the other hand, when we characterized the antenna with the existing FID pulser whose output amplitude was 4.4 kV, we obtained an electric field of 143 V/cm at the same position. Comparing the electric fields generated under these two conditions, it seems that they indicate a linear relationship between the applied voltage and the measured electric field, as was expected. This was found to be true despite the fact that the high voltage system had a slower rise time (510 instead of 200 ps) and thus had fewer high frequency components.

Increasing the driving voltage, therefore, is expected to generate higher electric fields. This can be achieved by increasing the charging voltage before the transformer. Proper measures to insulate the transformer need to be undertaken, for instance, by immersing it in oil. Accordingly, SW1, SW2, and the peaking switch all need to have higher hold-off voltages. One other possible means is to insert another switch (transfer switch) prior to the peaking switch. This switch allows for the isolation of the fast part from the slow part. The slow part of the system can still be based on dual resonant charging, but the speed requirements of the transformer can be slower. The transfer switch breaks down as soon as the load capacitor of the transformer reaches full charging voltage. The peaking switch in this case will close at a much faster speed at even relatively short gaps such as those seen in [56].

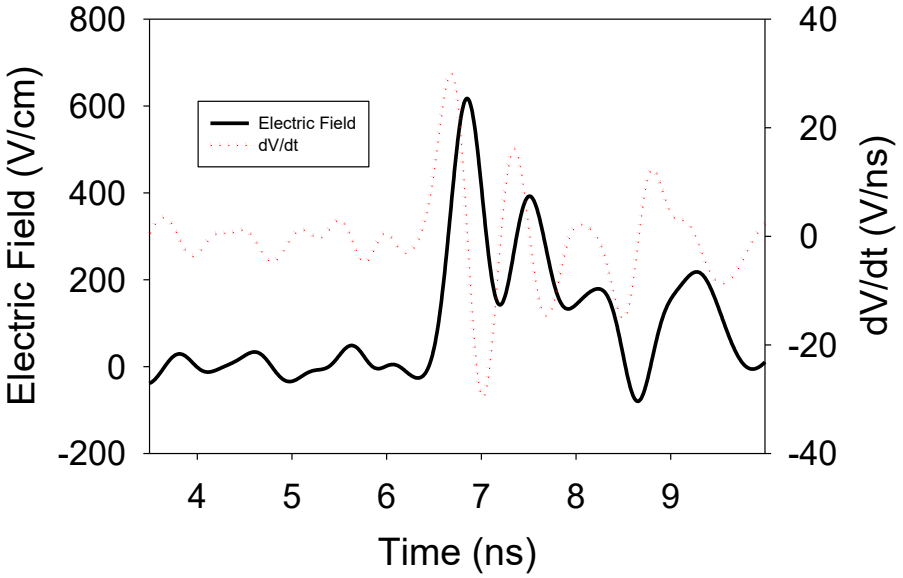

Fig. 46 The free space transient of the total antenna system. The D dot probe records the derivative of voltage (dV/dt). The electric field is the integrated signal. [55]

CHAPTER 4

4. STIMULATION OF NEURAL STEM CELLS

Before implementing the biconical dielectric rod antenna for in vivo applications, a key question , how the electric field can influence the neural cell outside of electrical stimulation, remains unanswered. Of particular concern is the possibility for psPEF to cause adverse effects (both short and long term) among the heterogeneous cell population in the brain. The only reported evidence of cellular damage (apoptosis) after picosecond pulse exposure has been reported for cancer cell lines. These experiments suggest that the electric field intensity required to affect cells is high (>100 kV/cm) [10] or that the number of pulses must be on the order of millions [19]. From this, it has previously been inferred that lower pulse parameters would be inert other than electrical stimulation; however, this has not been experimentally proven. To test this, an experiment was conducted to characterize changes in the viability, proliferation, metabolism, and gene expression of neural stem cells (NSCs) after psPEF exposure. NSCs were selected because they are present in adult brains and in dynamic cell types which are sensitive to stimuli [68].

In this chapter, the question of how neural stem cells are affected by psPEF will begin to be answered. Here, the pulses were delivered to NSCs by a pair of electrodes that were anchored on a custom 3-D printer. The electrodes were kept above the NSCs, and so the leakage electric field from a parallel transmission line affected the cells, which resembled the condition of an antenna. The major advantage of the 3-D printer exposure system is that it can deliver pulses to a large number of cells with a high yield, which is required for downstream analyses, including viability, proliferation, metabolic, and gene expression assays. Another advantage is that a stimulation pattern can be created by moving the electrodes in a precise trajectory programmed on the 3-D printer. With this powerful exposure system, we show that NSCs exposed to picosecond pulses exhibited metabolic reduction, change in proliferation, and up-regulation of glial fibrillary acidic protein (GFAP). As a comparison, we also tested mesenchymal stem cells (MSCs), which largely did not react to stimulation suggesting cell type specific effects. This also highlights the promising potential of psPEF to target NSCs alone. The findings of this study 1) shed light on how ultrashort electrical pulses affect electrically sensitive cells,

and 2) provide electric field parameters for designing an antenna for noninvasive neural stimulation.

4.1 A 3-D PRINTER SYSTEM FOR PULSE STIMULATION

There are currently two common configurations for a picosecond pulse exposure system. The first is a cuvette with two plate-electrodes in parallel [8]. This configuration has the ability to pulse a large number of cells, but the cells have to be in suspension. Such a setup is not advisable for stimulating adhered cells such as functional neurons. The second setup is a coaxial cable which transitions into a pair of wire electrodes [69]. This is the setup which was adopted by this study for delivering pulses to adhered cells. Thus, when selecting psPEF exposure systems, users had to choose between exposing large numbers of cells in suspension or very few cells adhered to a substrate.

This 3-D printer-based system extends the capability of previous psPEF exposure systems to have the function of exposing adhered cells in large enough quantities to perform most common biological assays.

The electrode setup was based on a design described by Xiao et al. [69] that consists of a coaxial cable and two tungsten wires with a diameter of 0.1 mm. The coaxial cable was a 50Ω, RG316 cable (Pasternack, Irvine, CA) that was cut to form two connection points: one with the inner conductor forming the anode and the other with the outer conductor forming the cathode. Epoxy was used to fix the electrodes at a distance of 1.0 mm. The picosecond pulses were generated by a 5 kV pulser (FID GmbH, Burbach, Germany) with a repetition rate of 1 kHz. The pulse had a rise time (defined by 10-90% of amplitude) of 460 ps and full width half maximum of 660 ps.

The strength, spatial distribution, and transient of the electric field were modeled using a finite difference time domain (FDTD) algorithm within CST Microwave Studio. The model for simulation consisted of a 10 cm segment of RG316 coaxial cable, 1 cm long parallel electrodes modeled as a perfect electrical conductor, epoxy glue to fix the electrodes ($\varepsilon_r = 2.10$), water (dielectric and dispersion properties were modeled as a Debye Model), and a polystyrene well plate ($\varepsilon_r = 2.50$). The normalized transient of the FID brand pulser was the input signal applied to the open-ended coaxial cable. The transient electric field was simulated at the center of the electrode. It had a rise time of

503 ps, amplitude of 1016 V/m, and full width half maximum of 717 ps. (Figure 1(a)). Since the electric field scaled linearly with the applied voltage, the electric field of 20 kV/cm and 40 kV/cm was achieved by setting the input pulse amplitudes to 2 kV and 4 kV, respectively.

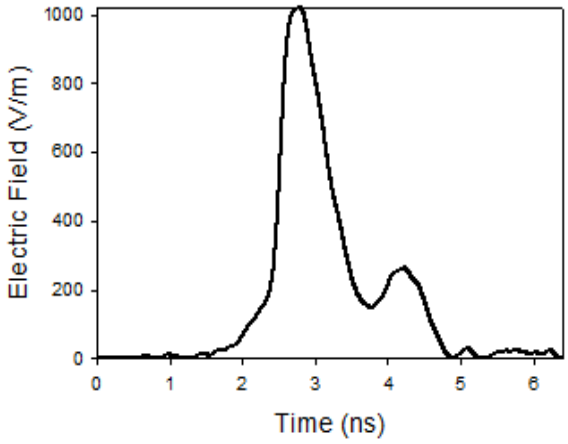

Fig. 47 Electric field transient at the center of the well plateIt has a rise time of 1300 ps, amplitude of 1016 V/m full width half maximum of 730 ps.

The simulation also gave insight into the spatial distribution of the electric field (Figure 1(b) 1(c)). The electric field was concentrated in the area between the electrodes and extends to the surface of the well plate. By definition, the electric field lines extended to infinity around the dipole. Therefore, we defined the half-power point or the -3 dB reduction area as having received one pulse.

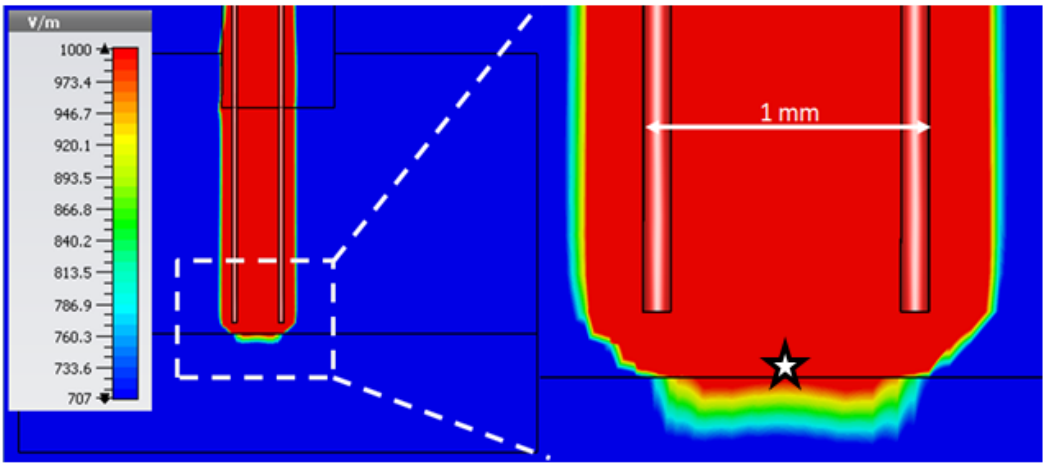

Fig. 48 FDTD simulation of the electode for a 1 V input. The electric field amplitude is shown with a color ramp which is clamped to -3 dB of the maximum at the peak time point (2.75 ns). It shows an electric field which is strongest in the area between the electrodes. Additionally, the field extends to the surface of the plate. This is clearly seen in the blown up image of the electrode and well plate. This parameter defined the feed rate and travel distance of the 3-D printer in the X-Y plane. The area receiving electrical stimulus is elliptical with a major axis of 0.96 mm and a minor axis of 0.59 mm. For cells to be exposed to 1.8k pulses at a pulse repetition rate of 1 kHz, the federate of the 3-D printer was set to 20 mm/min.

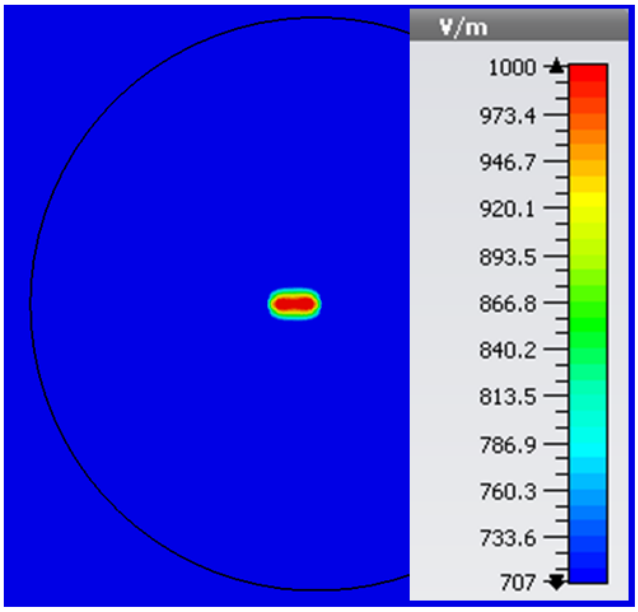

Fig. 49 Determining the pulsing parameters

The two-wire electrode configuration has been employed for numerous electrophysiological experiments; however, when fixed in position, it is not capable of stimulating sufficient cells necessary to perform downstream biological assays such as immunocytochemistry, nucleic acid extractions, proteomics, etc. Our approach used a 3-D printer as an automated micromanipulator for a continuous, long range psPEF exposure. By simultaneously stepping and pulsing, large numbers of adhered cells could be treated in a uniform manner. In essence, the use of a 3-D printer expands the exposure capability of the two-wire electrodes.

The printer used in this application was a Felix 3.0 (FELIXrobotics, Ijsselstein, Netherlands). It has 13.00 µm resolution in the horizontal plane and 0.39 µm resolution in the vertical direction. The off-the-shelf, plastic extruding print head was replaced with a modular mounting bracket. In previous experiments, this bracket was used to attach an extrusion head for bioprinting [70]. For psPEF exposure, a custom PLA electrode holder was attached to the mounting bracket. This functioned to fix the position of the electrode. It was important for the attachment to have a low profile (5.0 mm diameter) to allow for maximum maneuverability within the well plate and to ensure the greatest possible exposure area.

The travel path of the print head was controlled by custom G-code programmed with MATLAB and Statistics Toolbox Release R2017a (The MathWorks, Inc., Natick, Massachusetts, United States). The program library used functions based on natural language to construct the printer code. This allowed the user to design complex three-dimensional geometries using control flow or conditional statements. The MATLAB program is also capable of graphically displaying the 3-D travel path in a cell culture well. This display was used to debug and confirm the path of the print head.

The use of an electrode for psPEF exposure within the 3-D printer created several new design challenges. These included having to accurately determine the vertical position of the probe as it influenced the electric field strength as well as automatically triggering the pulser to turn on when it was above the cells and turn off when it was out of range. To accomplish these tasks required a combination of hardware, software, and calibration procedures.

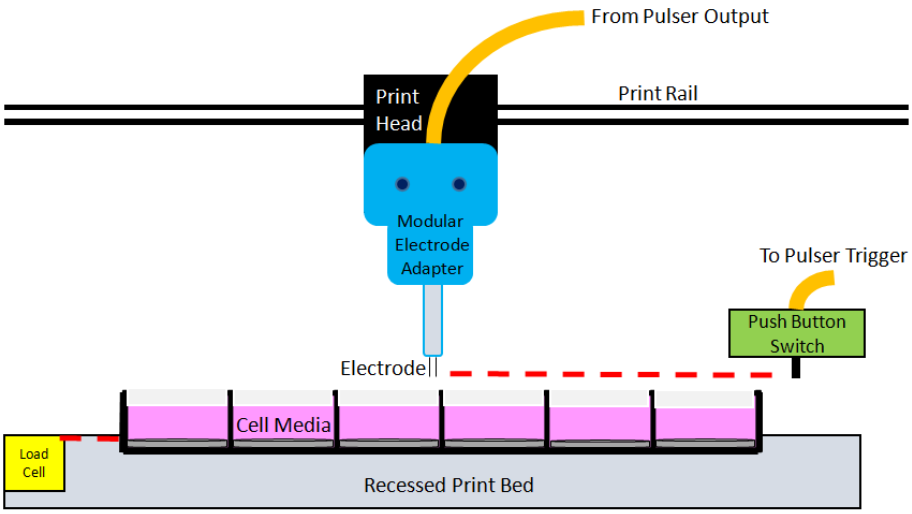

Fig. 50 A cross sectional view of the 3-D printer setup depicting the interaction of the electrode, print bed, load cell, and push button (pulse activation) switch. The load cell is in line with the surface of the print bed. The push button switch is in line with the electrode tips

The hardware consisted of a recessed print bed and load cell. First, a print bed was manufactured with a CNC to incorporate a standard cell plate (4, 6, 12, 24, 48, 96 well). Using a Santa Cruz forty-eight well plate (Santa Cruz Biotechnology, Huston, TX), there was a 200 µm distance from the surface of the well plate to the surface of the

print bed. Similarly, the print bed surface was milled to incorporate the 100 g load cell (Phidgets, Calgary, Canada). The load cell surface was aligned with the print bed surface. To calibrate the vertical height, the electrode was lowered until it came into contact with load cell. When the electrode tip applied the force of 0.0400 g (the lowest observable force), a microcontroller sent a digital signal to the printer software (Repetier, Willich, Germany) which registered the vertical location as Z = 0 within a relative coordinate system. In this way, the load cell acted as a highly sensitive, non-deformable switch. An image of the actual probe setup is shown in Fig. 51.

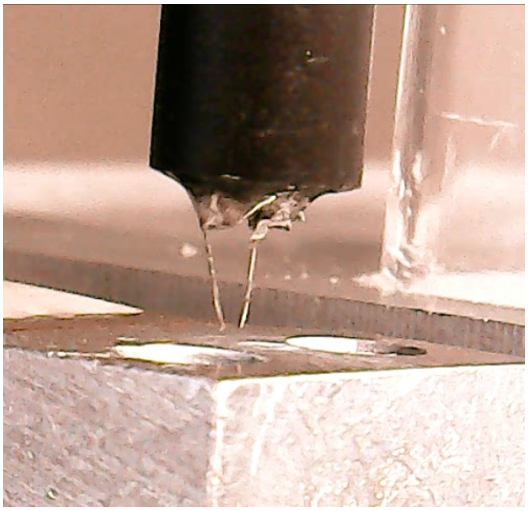

Fig. 51 Electrode and load cell interaction. The electrode is lowered on to the load cell in order to calibrate the Z-height of the printer.

Once the Z-height was set, a custom G-code was generated to sweep the electrode over the selected cell tissue-ware in the X-Y plane. The pattern was a parallel-track pattern set at 1.00 mm apart. The probe would transverse the length of the culture-ware, step to the side, and return along the length of the cover slip. Fig. 52 demonstrates the travel path of the electrode through two rows of a forty-eight well plate. In order to avoid electrical arcs in the air while the electrode was traveling between wells, a push button trigger switch was incorporated. When the print bed rose to meet the electrode, it would depress the push button and trigger the pulse power supply. An LED was added to indicate the presence of high voltage pulsing.

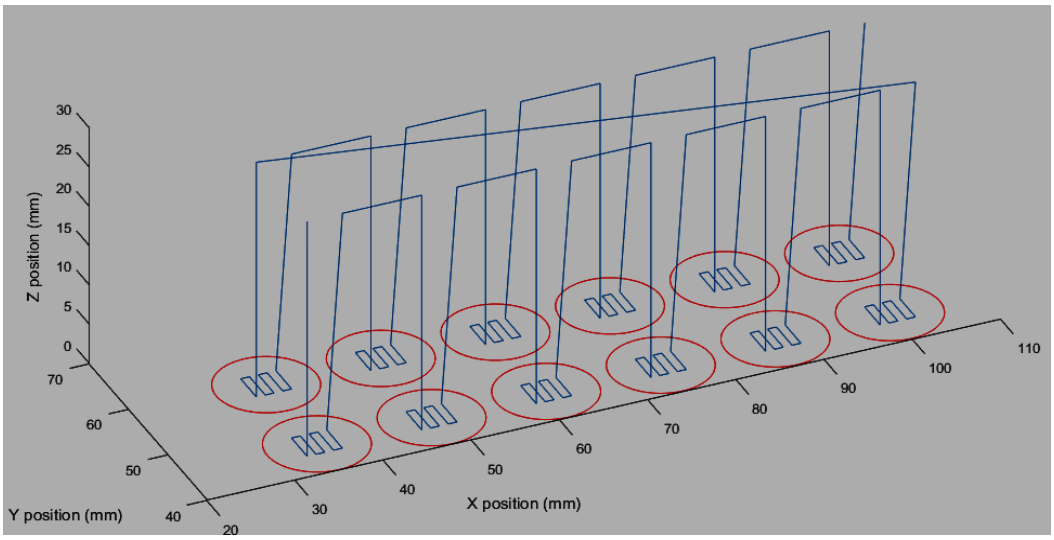

Fig. 52 Travel path of the electrode. The electrode travel is shown in blue though two columns of a forty-eight well cell culture plate. The red circles indicate the edges of each well.

In future designs, it should be possible to increase the pulsed area. Within the current setup, there is a group of unexposed cells along the periphery of the well plate, due to the inability of the electrode to reach the edge. This underexposure can be corrected by angling the electrode so that the electric field can penetrate into the edge. Additionally, in the current design iteration, there is a linear relationship between the velocity of the print head and the number of pulses received. Thus, increasing the number of pulses or the number of samples (lengthening the travel path) could lead to extended times out of the incubator. It can also create a time shift between the first and last cell being pulsed. One technique to correct this would be to increase the exposure area by replacing the wire electrodes with parallel plates. Importantly, however, the ability of the 3-D printer system to target the specific regions of a culture well could be advantageous in regenerative medicine and in experimental applications.

4.2 BIOLOGICAL ASSAYS

A human, wild-type breast-derived adipose stem cell (bASC3) line was previously isolated [71-72]. The multipotent potential of this mesenchymal stem cell (MSC) line had previously been verified [72]. MSCs were cultured in Dulbecco's

Modified Eagle's Medium (DMEM) containing Glutamax (Gibco, Gaithersburg, MD), supplemented with 10% premium fetal bovine serum (Life Technologies, Carlsbad, CA) and 1% Antibiotic-Antimycotic (100x) (ABAM; Life Technologies). The medium was replenished between 72 and 96 hours after seeding and throughout the culture. Neural stem cells (NSCs) were created using the bASC3 line that had been reprogrammed into induced-pluripotent stem cells. Briefly, iPSCs underwent neural induction using STEMdiff™ Neural Induction Medium (NIM) (Stemcell Technologies; Vancouver, Canada) according to the manufacturer's embryoid body protocol. Approximately 3.0-4.0 x 10^6 cells were put into single-cell suspension and were plated into a single well of the AggreWell™ 800 Plate (Stemcell™ Technologies) with NIM supplemented with 10 μM Y-27632. Cells were centrifuged for three minutes at 100 x g and then were placed into a humidified incubator. Half media changes occurred daily for 4 days. On day 5, embryoid bodies were dislodged with a micropipette and plated onto Geltrex® coated wells in NIM where daily media changes occurring until day 11. On day 12, neural rosettes were dislodged using STEMdiff™ Neural Rosette Selection Reagent (Stemcell Technologies) and were expanded. NIM was replaced on neural rosettes on day 19 with StemPro® NSC SFM medium supplemented with 10 ng/mL bFGF, 10 ng/mL EGF, and 1x ABAM. Media was replaced every 48 hours. NSCs were cultured on Geltrex-coated culture ware or glass slides diluted 1:100, dependent on the assay. Cells were passaged upon reaching 75-85% confluency using TrypLE Express (Gibco) following the manufactures protocol. Cell lines were maintained at 37˚C in a humidified incubator with 5.0% CO_2.

To determine the apoptotic effects of psPEF, Live/Dead® Viability/Cytotoxicity Kit (Molecular Probes, Eugene, OR) was used according to the manufacturer's protocol. Briefly, after psPEF treatments, cells were washed with PBS twice for 2 min. Next the PBS was supplemented with 2 μM calcein AM and 4 μM ethidium homodimer-1, and was added to the exposed wells. Cells were then allowed to incubate for 30 minutes at 37˚C. After incubation, cells were washed with PBS twice before the complete media was reapplied for analysis. Following Live/Dead staining, fluorescence microscopy images were acquired using a Zeiss Axio Observer.Z1 microscope (Carl Zeiss AG, Jena, Germany) with either 10X or 20X objectives. Images were taken at 10 min, 1 hr, and 24

hrs post-treatment. The results of this experiment for NSCs can be seen in Fig. 53. MSC data is located in Appendix B.

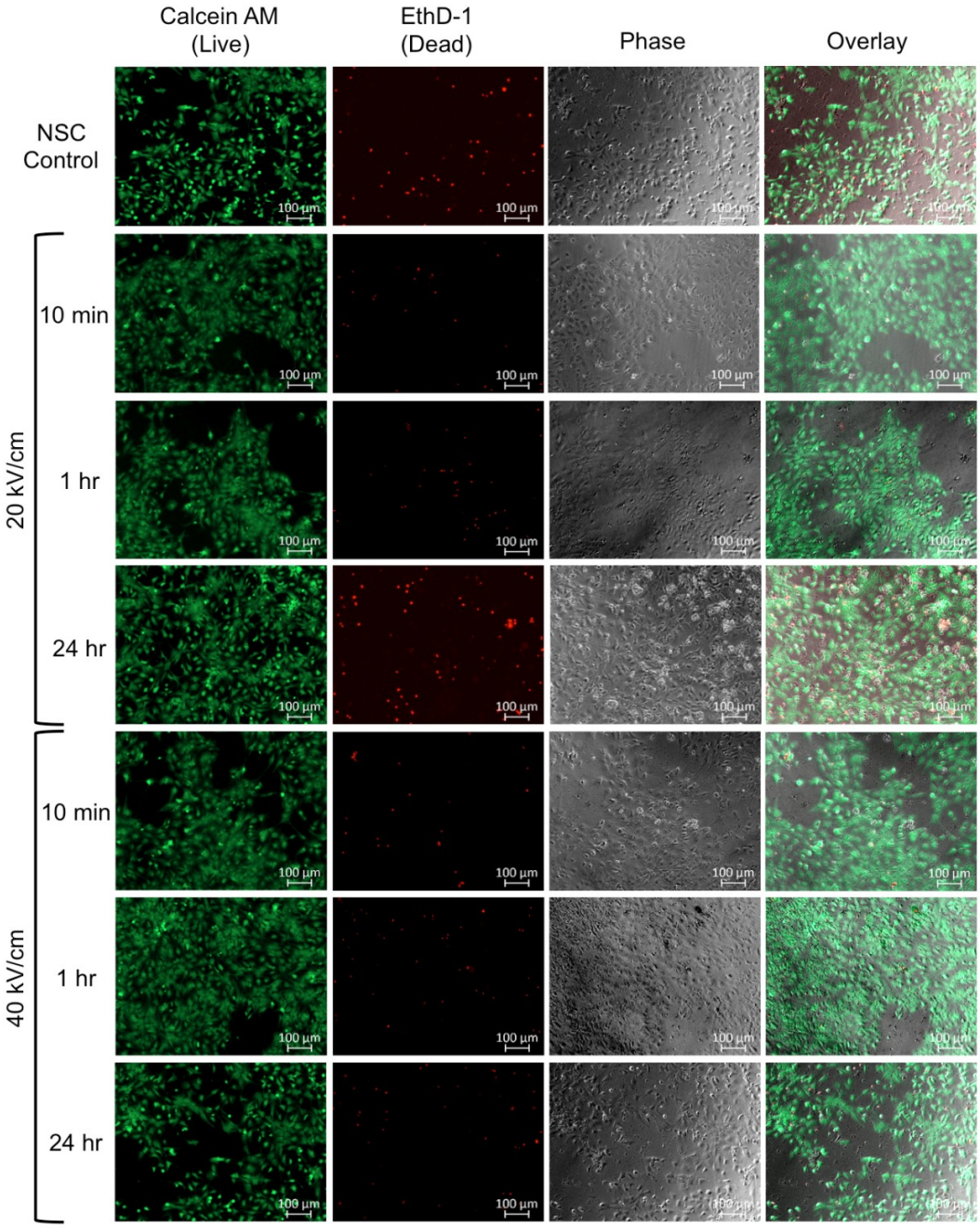

Fig. 53 Pulses do not induce cell death in NSCs. Neural stem cells exposed to 20 kV/cm and 40 kV/cm were treated with calcein AM and EthD-1 to determine potential cytotoxic effects. Relative to the control (non-pulsed) neural stem cells, no increase in cell death was detected at 10 min, 1 hr, or 24 hr post-pulse treatment in either pulsing parameter. All images were acquired with a 10x objective.

Previous experiments have shown that psPEF can cause cell death; however, in these studies, the electric field strength and pulse number were much greater than in the current application [8]. Here, cell death was measured after exposure to 1800 pulses at 20 kV/cm and 40 kV/cm using the live/dead stain EthD-1. We found no significant difference in induced-cell death relative to untreated controls in either NSCs or MSCs at either 20kV/cm or 40kV/cm, relative to untreated controls (Fig. 53). These data combined demonstrate that 20 kV/cm and 40 kV/cm do not induce cell death in two different cell types. Importantly, the experiment provided the electric field parameters that do not affect cell survival, allowing for further downstream experimentation.

We sought to determine the effects that psPEF treatments would have on the metabolic activity of cells by measuring the reduction of resazurin, via AlamarBlue assay. After psPEF treatment, the basal medium was replaced with a complete media supplemented with 10% AlamarBlue. The cells were allowed to incubate at 37˚C. The reduction of AlamarBlue was detected at one hour post-treatment by measuring fluorescence intensity, relative to untreated control wells of the same cell type. An AlamarBlue assay was conducted in quadruplicate. Fluorescence intensity was detected using a SpectraMax i3 Multi-Mode Detection System microplate reader (Molecular Devices, Sunnyvale, CA). Graphical representation of metabolic activity is shown as the mean reduction of experimental wells. Error bars represent the standard deviation. Statistical significance was determined by using a two-way ANOVA with a Dunnett's post hoc.

We next examined the metabolic effects that 1800 pulses of 20 kV/cm and 40 kV/cm would have on MSCs and NSCs. Four wells of each cell type were treated with our pulse-parameter. Immediately following treatment, basal media was changed to a complete media that had been supplemented with 10% AlamarBlue and was returned to the incubator. After one hour, metabolic activity was measured through the increased fluorescence of reduced resazurin. Relative to the normalized, untreated MSC control, MSCs that received 20 kV/cm showed a 3.76% increase in the metabolic reduction, while MSCs exposed to 40 kV/cm showed a 6.17% increase in the metabolic reduction (Fig. 54). Both exposure parameters on NSCs also revealed statistically significant increases

in the metabolic reduction of AlamarBlue. NSCs exposed to 20 kV/cm showed a 2.34% increase, and NSCs exposed to 40 kV/cm showed a 2.57% increase in resazurin reduction relative to the untreated NSCs shown in Fig. 54. These data reveal that psPEF affect cellular processes related to metabolism.

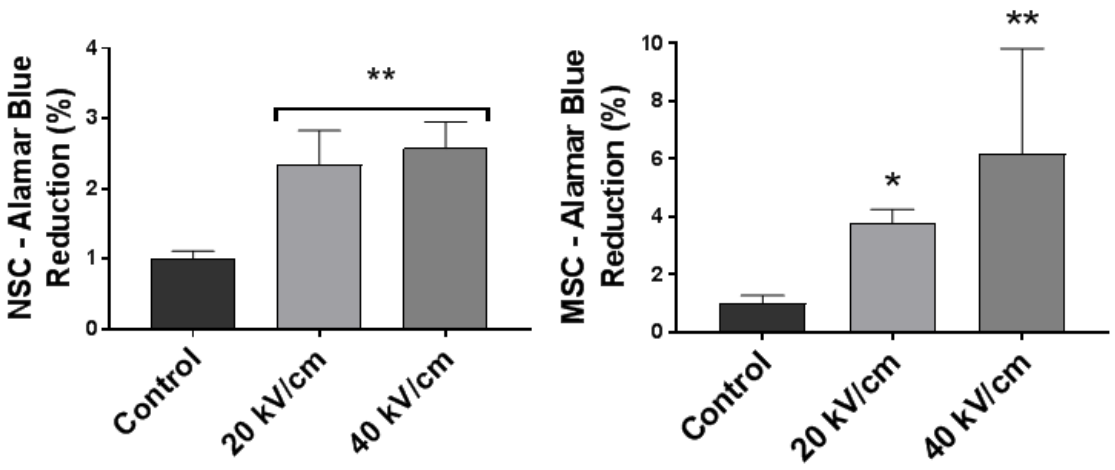

Fig. 54 Cell increase mitochondrial metabolic activity after pulse exposure NSCs showed a 2.34% increase at 20 kV and a 2.56% increase at 40 kV while MSCs showed a 3.76% increase in AlamarBlue reductions at 20 kV and a 6.17% increase at 40 kV. Statistical significance was determined using a two-way ANOVA with a Dunnett's multiple comparison. $*P < 0.01$, $**P < 0.001$ (n=8).

To measure the cell's ability to proliferate, we measured DNA synthesis using the Click-iT® EdU Imaging Kit (Molecular Probes), according to the manufacturer's protocol. Post-treatment, cell media was supplemented with 10 μM of EdU and was returned to incubation for 24 hours. Upon reaching the desired incubation time, cells were fixed with 10% neutral buffered formalin for 15 minutes, and were permeabilized with 0.5% Triton X-100 for 20 minutes, all at room temperature. After the addition of the recommended Click-iT reaction cocktail and a 30 minute incubation, the cells were counterstained for nuclei detection with DAPI (1:1000). Fluorescent microscopy images were acquired of entire wells using a Zeiss Axio Observer.Z1 microscope (Carl Zeiss AG) with a 20X objective. EdU incorporation was determined using ImageJ software, version 1.51p FIJI (National Institutes of Health, Bethesda, MD). Graphical representation of EdU incorporation percentages are shown as the total number of EdU

positive cells (green) divided by the total number of DAPI-stained cells (blue). See Fig. 55 for NSC data and Appendix C for MSC data.

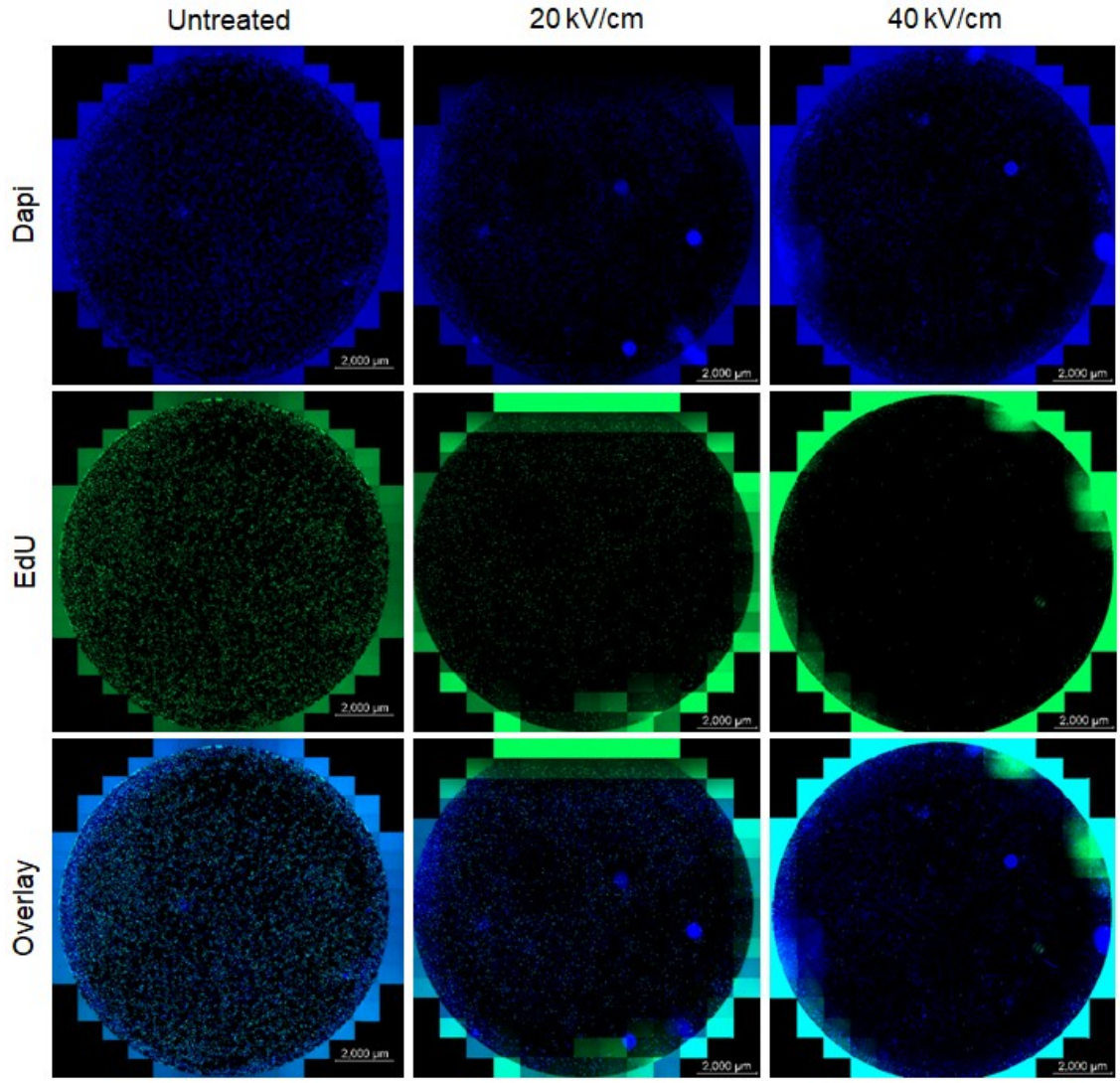

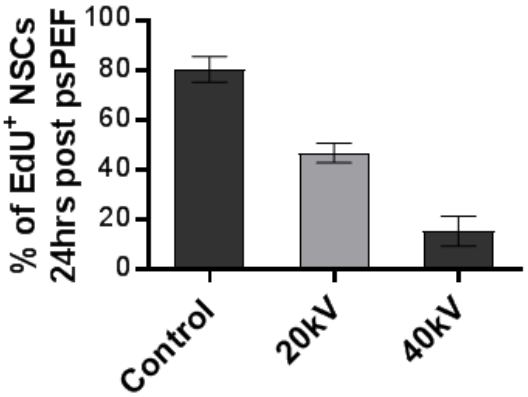

Fig. 55 Picosecond pulses inhibit proliferation in NSCs. Representative images of entire well of NSCs immediately following psPEF exposure, and EdU supplement/fixation following 24hr. Cell nuclei were counterstained with DAPI. NSCs exposed to 20 kV (center column) and 40 kV (right column) showed EdU incorporation percentage of 37.7% and 12.5 %, respectively. Untreated control NSCs (left column) showed EdU incorporation percentage of 80.5%. Untreated control (left column) showed EdU incorporation percentage of 83.6%. Tiled images of the entire well were acquired with a 10x objective.

One of the interesting possibilities of using the 3-D printer to expose cells is the potential to target pulses with the aim of only affecting select cells within a culture. To test this, we conducted a single pass of 40 kV/cm pulses over a 10 cm path on NSCs. After 24 hours of incubation, fluorescent images were taken of the path as well as of the 2 cm above and below the path. Visualization of the EdU assay revealed that proliferation for NSCs directly below the applied psPEF was reduced (Fig. 56). These data demonstrate the localization of the applied field when one single psPEF transit is applied to NSCs, since the effects do not radiate externally beyond the designated path.

The electric field was computationally modeled to provide a uniform electric field across the exposed area; however, in situ, it is currently not possible to measure electric fields in real time at the required sub-millimeter resolution. Insight into the electric field distribution can be achieved by comparing the computational model to the cellular response. In our linear test, we saw that there is no discernible gradient. Only the cells within the electrode path had reduced proliferation and the size of the non-uptake area was nearly identical to the simulation. Additionally, within the simulated area, there was a uniformity of cellular effects. More evidence of the system's stimulation precision exists in the images of the whole well. The electrode path was designed to simulate a maximal area across the well plate. However, because the electrode was not able to make it to the edge of the circular well, there was a ring of unexposed cells. The presence and invariability of the outer ring, both within a well and between wells, demonstrates a well-defined and repeatable psPEF exposure.

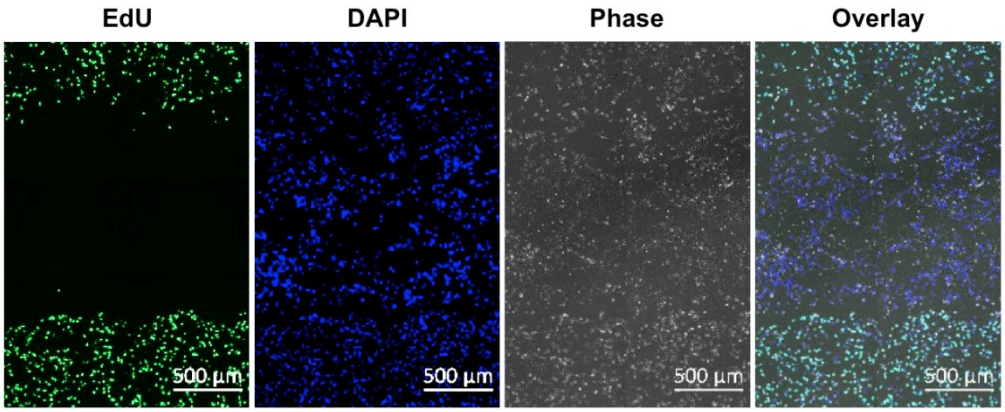

Fig. 56 Pulses exert an effect only under the travel path. NSCs were in a 4-well tissue culture dish and exposed to one single path of 40 kV/cm. Immediately following exposure, media was replaced and supplemented with EdU and fixed after 24hrs. Electrode travel path with ~1mm of non-proliferating cells can be seen (left panel). All images were acquired with a 10x objective.

To determine transcriptional effects of psPEF, gene expression was conducted on NSCs and MSCs exposed to 20 kV/cm and 40 kV/cm, as well as on untreated cell samples. Total nucleic acid was collected using TRIzol® Reagent and the phenol:chloroform protocol for adherent cells provided. Genomic DNA was eliminated using Deoxyribonuclease I, Amplification Grade (Invitrogen; Carlsbad, CA). After DNAse treatment, 1 µg of RNA was reverse transcribed using High Capacity cDNA Reverse Transcription Kit (Invitrogen), as per the provided protocol. All cDNA samples were diluted to 5 ng/µL with DNAse/RNAse free water. Gene expression analysis was conducted using TaqMan Fast Advanced Master Mix (Thermo Fisher) with TaqMan Probes for DCX (Hs00167057_m1), GFAP (Hs00909233_m1), GALC (Hs01012300_m1), RUNX2 (Hs0147973_m1), PPARG (Hs00234592_m1), SOX2 (Hs01053049_s1), and POU5F1 (Hs00742896_s1). The housekeeping gene used was ACTB (Hs99999903_m1). Each reaction contained 10 ng of cDNA. All gene expression assays were conducted on a StepOnePlus Real-Time PCR System (Applied Biosystems; Foster City, CA). All experiments were conducted in triplicate. Relative gene expression was determined using the fold regulation method ($2^{-\Delta\Delta Ct}$). Statistical significance was

determined using a one-way ANOVA. Error bars represent the standard deviation of the mean fold expression for each sample.

To describe the potential intracellular effects of psPEF on cells in vitro, we conducted gene expression analysis of each cell type to determine how selected pulse parameters would affect differentiation markers for potential lineages. To determine potential differential changes in NSCs that had undergone psPEF treatments, we chose to evaluate the markers doublecortin (DCX), galactosylceramidase (GALC), and glial fibrillary acidic protein (GFAP). DCX is a microtubule-associated protein that is expressed in immature neurons in developmental cortical structures, and it is a well-known early-developmental marker for neurogenesis [73]. GALC is a marker for oligodendrocytes, where is it highly enriched. It is a lysosomal protein that hydrolyzes galactosylceramide, a major lipid found in myelin [74]. To determine astrocyte lineage, we chose GFAP, an essential protein involved in astrocyte-neuron interactions [75]. Expression was analyzed 12 and 24 hrs after pulsing with 20kV/cm and 40kV/cm. We found that, after 24 hours, NSCs treated with 40 kV/cm showed significant up-regulation in GFAP, with a fold expression increase of 1.95, relative to the untreated NSC samples Fig. 57. All conditions repeated in triplicate. Error bars represent the standard deviation of the mean fold expression of each triplicate. $*P < 0.01$, $**P < 0.001$.

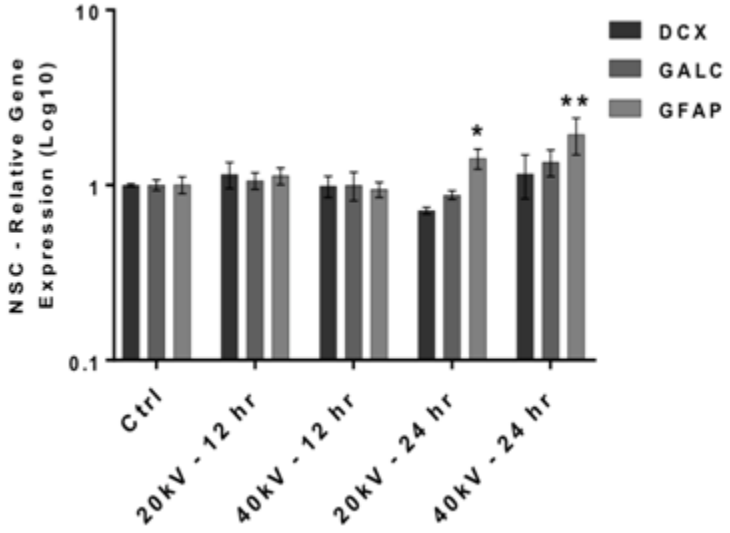

Fig. 57 Gene expression of NSCs is affected by psPEF NSC gene expression analysis at 12 hours and 24 hours post-treatment with 40 kV/cm and 20 kV/cm. The expression of GFAP is increased 24 hours after exposure.

Changes in MSC gene expression were determined using the same treatment parameters. The genes assessed were OCT3/4, PPARG, RUNX2, and SOX2. These genes are biomarkers for pluripotency, adipose cells, osteoblasts, and cell stemness, respectively. The relative gene expression was determined using the fold regulation method ($2^{-\Delta\Delta Ct}$). Statistical significance was tested using a one-way ANOVA with a Dunnett's post-hoc on the $2^{-\Delta\Delta Ct}$.

Unlike NSCs, MSCs did not demonstrate a significant increase in expression of either differentiation marker (Fig. 58). Rather, there was a significant and broad increase in SOX2. This occurred across both time points and stimulus parameters. These results demonstrate that psPEF can be used to differentially alter gene expression in MSCs. It is also a proof of the principle that psPEFs could potentially be used to target differentiation of NSCs, even in tissue with mixed MSC populations.

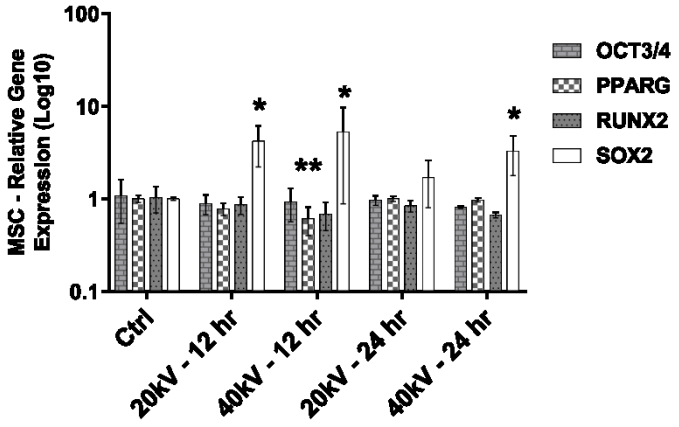

Fig. 58 Gene expression of MSCs is affected by psPEF. MSC gene expression analysis at 12 hours and 24 hours post-treatment with 40 kV/cm and 20 kV/cm. There is a significant increase in SOX2 expression.

4.3 DISCUSSION OF BIOLOGICAL RESULTS

Many of the previous studies in psPEF exposure have focused on cell death or cell membrane permeabilization. These studies found that very high electric fields and pulse numbers are necessary, in order to observe cell death. For example, apoptosis of B16 cells required 18,000 pulses at 150 kV/cm [8] or >1 million pulses at 25 kV/cm [76].

Additionally, the threshold for cell membrane permeabilization using picosecond pulses required an electric field of 550 kV/cm [8]. Our pulse exposure conditions were selected to minimize any cell death. The results of the Live/Dead experiment served to establish a baseline level for the exploration of electro-manipulation caused by psPEF.

The first evidence of electro-manipulation could be seen in metabolic reduction. Both MSCs and NSCs experienced an increase in metabolic reduction. It should be noted that the increase in signal could be due to psPEF interaction with voltage sensitive channels on the cell membrane. Opening channels with pulses could cause an efflux of lactate dehydrogenase (LDH); however, sustained channel openings are not currently known to occur at times long after pulse exposure.

Something that we noted as being extremely interesting was that the changes in proliferation after psPEF were cell type specific. Whereas NSCs were significantly affected, MSCs had no significant change. Whether there is a graded response between cell types (MSCs are more resilient than NSCs) or whether a different cellular mechanism is involved remains unclear. Here, we think that further experiments are warranted, in order to determine the difference between cell types.

Of the genes assessed, the only significant change in NSC gene expression was seen in GFAP. There was an up-regulation at both 20 and 40 kV/cm at 24 hours with the stronger electric field producing a greater and more statistically significance in gene expression. It should be noted that the increase in gene expression was not proportionate to the increase in electric field strength. Doubling the electric field did not double gene expression. This suggests some limiting factor. It is also possible that increasing the number of pulses at 20 kV/cm could also produce a significant up- regulation.

There is prior evidence which shows that GFAP expression in both NSCs and mature astrocytes (which already express GFAP) is up-regulated by electrical stimulation. When exposed to 3 kV/cm at 100 Hz, an up-regulation of GFAP in NSCs was recorded [77]. GFAP up-regulation was also seen when NCSs were exposed to 10 and 50 Hz AC signals at 1 V/cm (16). In mature astrocytes, GFAP was up-regulated in both astrocytes and microglia after exposure in an R-18 waveguide resonating at 1800 MHz [78].

This targeted up-regulation of GFAP presents a possible method for controlling the differentiation fate of NCSs. It could be used as a tool in vitro. With optimization or multiple treatments (to keep the GFAP expression elevated), psPEF could potentially be used as a tool steering the NSC's fate specifically towards astrocytes. Additionally, in vivo, as a potential stem cell therapy, this is potentially capable to stimulate NSCs to promote cortical astrogliosis.

A potential link between GFAP expression and electrical stimulation may come from studies in electroconvulsive seizures. When a seizure was induced in a rat using implanted electrodes (50 Hz) in the CA3 region of the rat hippocampus, there was a 10-fold increase in GFAP mRNA expression. It was also noted that GFAP mRNA returned to control levels several days after stimulation [75]. An additional study applied biphasic pulses at 20 Hz with amplitude sufficient to produce a seizure in rats and recorded a similarly significant increase in GFAP expression [79]. The up-regulation of GFAP was also not unique to electrically induced seizures. Magnetic pulse stimulation has previously been shown to up regulate GFAP. Using 10 Hz and 0.63 T magnetic stimulation on purified rat cortical astrocytes increased GFAP expression at 3 days post stimulation [80]. In an in vivo rat model there was a significant increase in GFAP mRNA expression [81]. Interestingly, an up-regulation of GFAP was also seen in chemically induced seizures, both in rats and in human patients [82].

As was previously suggested in seizure experiments [81-82], up-regulation of GFAP could be linked to STAT3. This is a logical mechanism, since STAT3 is involved in detecting neuronal injury and in initiating astrogliosis. STAT3 has also been shown to be up-regulated in microglial cells using electromagnetic fields radiated from an antenna at 2.45 GHz and 500 pulses per second [83]. Yet, mechanistically, STAT3 is triggered by kinase phosphorylation; thus, there must be a propagating event, which could react to electric fields. A potential signal transducer between psPEFs and STAT3 could be a voltage gated-calcium channels. An increase in calcium concentration activates Src family kinases which are required for the phosphorylation of STAT3 [84]. STAT3 phosphorylation is followed by a nuclear translocation, which, in turn, up-regulates GFAP.

There is prior evidence of voltage-gated calcium channels on the surface of the cell membrane opening after psPEF. Applying single 190 kV/cm 500 ps pulses was sufficient to increase cytosolic calcium in both GH3 and NG108 cells [85]. For a comparison, CHO cells (which lack any voltage gated channels) did not have an increase in calcium after psPEF. However, whether the electric field strengths present in this experiment (20 and 40 kV/cm) were sufficient to cause a conformational change in voltage dependent calcium channels is uncertain. This would suggest a much lower threshold than was previously reported. Further experiments are necessary to determine the potential role of STAT3 and calcium release as it relates to GFAP expression after psPEF.

Given the diversity of electrical transients (DC to picosecond pulses), which have been shown to up-regulate GFAP, this suggests that neural derived cells may have a targeted response mechanism towards non-human or disease state electrical stimulation. In this regard, calcium channels or a combination of voltage transducers may act like band stop filters. Normal electrical activity leaves the cell unperturbed, whereas chaotic electrical activity elicits a cell response in the form of increased GFAP expression. A full accounting of GFAP expression as a function of frequency is required in order to test this possibility.

In our analysis of MSCs, there was a concern that pulsed electric fields, if used to stimulate or direct neural stem cell fate, could potentially act in an undesired way on these somewhat ubiquitous cellular populations [72, 86-88]. Yet, our initial investigations revealed that the psPEF have little effect on their proliferation, and also on their differentiation. During the pulsed experiments we examined genes involved in both bone (Runx2) and fat (PPARG) formation, and both revealed that the stimulation had no appreciable effect.

Where the psPEF did have an effect was on the expression of SOX2. This up-regulation is indicative of a delay in differentiation and a preference for remaining a stem cell. The connection between psPEF and the up-regulation of SOX2 could potentially due to a protective effect. This is because SOX2 regulates survivin, which suppresses mitochondria mediated apoptosis [89]. Previously, mitochondria mediated apoptosis was found to be a mechanism for cell death after exposure to intense psPEF [10]. Further

experiments are necessary to confirm the potential role of survivin in SOX2 expression during psPEF exposure.

CHAPTER 5

5. ASSESMENT OF NON-CONTACT PICOSECOND PULSES

In the course of this investigation, there were two aspects of psPEF investigated. The delivery of psPEF was explored by designing a biconical dielectric rod antenna driven by a pulse power system. The effect of psPEF in two cell types was determined using an electrode anchored on a 3-D printer system. The purpose of this chapter is to reconcile these two disparate experiments and to determine the feasibility of the proposed antenna to be used as a non-invasive psPEF delivery technique.

The electric field readings taken from the antenna will be compared to the ability to stimulate tissue using the electrode. The first way of doing this will be a direct comparison of electric field amplitudes. The biological effects which are possible with the current techniques will be determined. The potential applications (ex. neural stimulation) will also be described.

5.1 COMPARISON OF EXPERIMENTS

There are several challenges in comparing psPEF experiments and pulsed electric field experiments in general. First is the importance of all of the stimulus parameters (amplitude, number, repetition rate) in the interpretation of the experimental results. It is unwise to make absolute statement about the biological response of picosecond pulses. Therefore, the results will be discussed in terms of trends. Additionally, one of the central challenges is that the application of the electromagnetic field is a graded stimulus, but the biological response is binary. In a two-wire electrode configuration, there is a high electric field near the wires with the field lines decreasing as a function of distance [90]. Conversely, the cellular response is binary. The cell either uptakes a given dye or it does not. To accurately determine the stimulus and response threshold requires an iterative process testing many field applications. A 3-D bioprinter system, which when operated in the continuous pulsing mode, could aid in the automated variation of stimulus parameters, but this was beyond the scope of these experiments.

Based on the electric field parameters, the biological results should be different. For the antenna system, the recording showed a pulse waveform with a rise time of 510 ps, an amplitude of 617 V/cm, full width at half maximum of 400 ps, and a repetition rate

of less than 10 Hz. Conversely, the electrode design had a rise time of 1300 ps, an amplitude of 20-40 kV/cm, full width half maximum of 730 ps, and a repetition rate of 1 kHz. All of the antenna parameters are less favorable to the electrode. Higher fields, longer pulses, and faster repetition rates, which are present in the electrode, are preferable for electrical stimulation for any kind of pulse.

Previously, the primary challenge of antenna-based psPEF delivery has been the low electric field. This was also the case for this antenna system. The electric field supplied by the antenna is most likely not sufficient to cause the firing of an action potential at a field of 20 kV/cm in the brain. It is smaller by a factor of approximately 30. While the antenna may be insufficient to cause an action potential, the same electric field could have impacts on other cell types in the brain. This requires additional experiments (such as those in Chapter 4) to determine the electric field threshold for biomedical applications. There is also the possiblity that the antenna could work in a neural application using heating. A higher repetition rate peaking switch could allow for hyperthermia applications.

Non-contact psPEFs were found to affect both NSCs and MSCs at sub-cytotoxic levels. This could lead to interesting applications in tissue engineering. For example, changes in metabolic activity could lead to treatments for obesity. Changes in proliferation were cell type specific. More research ought to be done to determine appropriate cell types to treat.

More interestingly, psPEF caused a targeted change in gene expression. In NSCs, a targeted up-regulation of GFAP presents a possible method for steering differentiation fate. With optimization of pulse parameters, multiple treatments, or combination of pulses and pharmacological agents, psPEF could potentially be used as a tool to steer the NSC's fate specifically toward astrocytes. This could have applications in responding to neural injury.

MSCs underwent a change in the regulation of two genes. The decrease in PPARG expression was shown to occur only at a 40 kV/cm and for a short period of time (12 hours) before it returned to pre-exposure levels. This suggests that higher field strengths are required to influence the regulation of this gene. Practically, down-regulation of PPARG could be used to deter MSCs from a fat cell differentiation fate.

The SOX2 gene expression was influenced by both electric field parameters. The targeted up-regulation of SOX2 could have potential applications in maintaining the pluripotency of stem cells.

A key missing step in these applications is to determine the lower limit of electric field application necessary to produce a biological result. What is evident from this study is that biological changes can occur at levels much lower than those previously suggested.

5.2 A PATH FOR THE BICONICAL DIELECTRIC ROD ANTENNA

The final step is to determine the efficacy of the biconical dielectric rod antenna and its potential applications. In the experiment, the constructed antenna was able to radiate a picosecond pulse with a rise time of 510 ps and an amplitude of 617 V/cm. This is the basis for describing the potential path and applications of the technology.

The current dielectric rod antenna was designed for neural applications. However, in its current form, the antenna does not seem to deliver a high enough electric field to induce an electrical response in the form of an action potential. As such, for neural applications, the primary goal is to increase the electric field radiated by the antenna. There could be several strategies to this end.

The first approach would be to improve the construction of the system with a focus on the antenna feed. In this design, the pulse power supply is coaxial in output of 50 Ω, which is inserted into a 50 Ω transmission line and then into a 50 Ω antenna. While there is a match of impedance value, the geometry changes are abrupt, meaning a loss at the transition. The true extent to which this affects the actual input voltage is unknown. An electro-optic sensor could potentially be inserted in the parallel plate transmission line to measure this. To resolve this issue requires the design of a singular machined part which can integrate the discrete components. The challenge of this is that the effort to integrate the components would in itself create a mismatch. For example, one technique would be to used a tapered balun which transitions the coaxial cable to a parallel plate. The problem with this approach is that the impedance across the transition increases from a 50 Ω cable to an approximately 200 Ω plate [91]. Because a lower impedance is preferable for creating a high field in the brain, this approach is not ideal.

The challenge of creating a high field may be thr problem of the antenna material itself. In the simulation, the dielectric was assumed to be lossless across the frequency spectrum of the input pulse, as well as across the voltage range. This may not be the case, in reality. In many materials, the loss tangent increases with frequency and voltage. The construction of this antenna relied on a commercially available composite material whose properties are proprietary. Using the currently available equipment, the dielectric properties of the material can be tested using an open end coaxial probe technique [92]. Ultimately, other materials should be investigated.

Lastly, if none of these strategies bear out, then a higher pulse power supply may become necessary. This is an option of last resort, because increasing the voltage puts additional strain on the materials, and thus on the design itself. It is also a possibility that, in order to withstand higher voltages, the antenna may need to become larger, thereby reducing the focusing and interface with the tissue.

The biological results from Chapter 4 show that psPEF have the ability to cause intracellular changes in a non-contact manner. This opens the door to many new potential applications outside of electrical stimulation. There are both potential in vivo applications and in vitro applications

For in vivo applications, the focus could shift from neural targets to superficial ones. This would further relax the requirements on the antenna design because the field would have less attenuation on the surface. In the antenna simulation, the electric field at the skin is 28 V/m, compared to 11.5 V/m in the brain for a 1 V input. The field value on the skin could increase considerably with optimization. If a sufficiently high dielectric is found (in order to reduce the effective diameter of the rod), it may also be possible to eliminate the emitting section of the antenna and to allow for the direct application of the field to the skin. This could further improve coupling and transmittance into the surface tissue. The biological results previously presented suggest some possible applications of superficial stimulation. For example, the increase in metabolism was not cell-type dependent. Pulses could potentially increase the metabolism of fat cells for the treatment of obesity. Additionally, changes in gene expression could be targeted toward wound healing and regeneration, for cosmetic purposes.

It is also possible that the antenna could be used as a laboratory tool and target in vitro applications. The antenna could be used to simulate changes in the cells, which would then be used for downstream processes. If the psPEF are able to induce a complete targeted differentiation in NSCs, the cells could be lifted from the substrate and used for in vivo applications. In the case of MSCs, the psPEF increased the SOX2 expression, which is noted for its ability to maintain the pluripotency of the cells. In this case, the antenna could be used as a tool to prevent MSCs from differentiating. One of the challenges of using the antenna in vitro is that a further reduction in size in necessary in order to be used with standard culture plates. To do so requires investigating high dielectric materials for the construction of the biconical dielectric rod antenna. Currently, ceramics, such as partially stabilized zarconia ($\varepsilon_r = 28$), are being investigated for the construction of such an antenna.

CHAPTER 6

6. CONCLUSIONS

The foundation of this work is in developing a system for picosecond pulse electric field stimulation. It seeks to answer the question "Are picosecond pulsed electric fields capable of non-invasively stimulating neurological tissue – and if so, what effects would they have on neural cells?" The pulse delivery aspect was addressed by modeling and simulation. In a biological model, it was show that psPEF can be delivered to the shallow brain region. To drive the antenna required a high voltage pulse power supply. This was constructed, and the antenna was tested in free space. The question of psPEF effect was determined using a non-contact electrode. At an electric field of 20 kV/cm, psPEF were shown to have effects on neural stem cell proliferation, metabolism, and gene expression.

6.1 FUTURE DIRECTIONS

Within this project, there are successes that can be built upon. Foremost is the area of intracellular changes caused by psPEF. If sufficient electric fields are applied to cells, it can cause conformational changes in proteins. If the disease is caused by protein aggregates, such as Alzheimer's disease or Huntington's disease, psPEF may be able to break the aggregates apart. There is a computational basis for this approach [93]. Moreover, there is preliminary data to suggest that this is possible.

The next goal would be to increase the transmittance of psPEF into tissue by investigating new antenna concepts. One such design is the forward impulse radiating antenna [94]. It is similar to the biconical dielectric rod concept, although the conducting elements on the emitting section are rotated and integrated into the dielectric material. This concept, when integrated into the dielectric rod antenna, is shown in Fig. 59. It is currently believed to be well suited for shallow or surface stimulation.

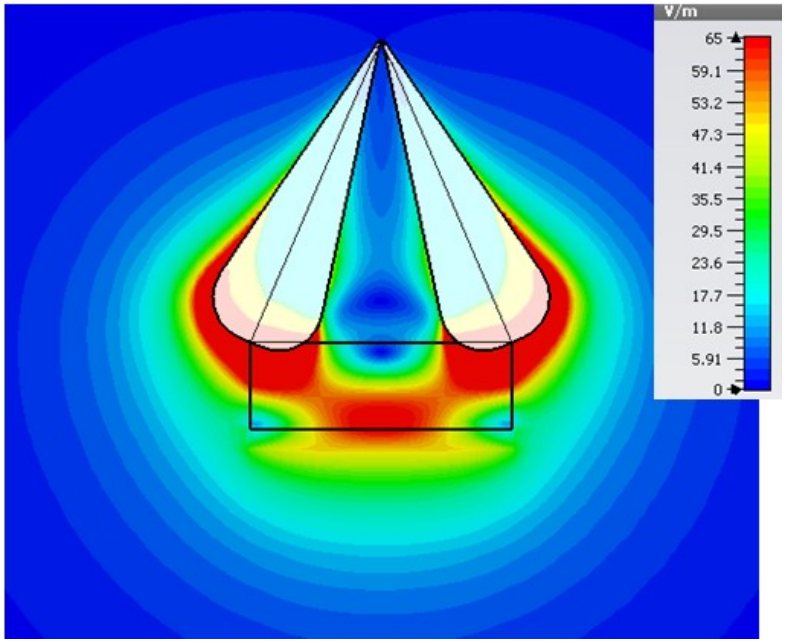

Fig. 59 A future dielectric rod concept. The feed elements are rotated and integrated into the dielectric rod. This could potentially increase the transmittance.

A final area to consider is electric field enhancement techniques. By including additional elements which magnify the electric field at the cell, the threshold for causing biological simulation and thus the antenna burden can be reduced. There are currently two possible methods for doing this. First is incorporating charged peptides with the cells. This technique has been shown to be effective for pulses in the microsecond range [14]. Alternatively, metallic nanoparticles can be adhered to the cell membrane to create an electric field stress [15]. An additional benefit of this technique is that it moves from treating the bulk tissue to cellular level resolution stimulation.

6.2 SUMMARY OF WORK

An ultra-wideband biconical dielectric rod antenna was designed to deliver picosecond-pulsed electric fields to the shallow brain for neural stimulation. Using a realistic human model, the antenna was shown to be capable of stimulating areas much smaller than current repetitive transcranial magnetic stimulation techniques. Key to this antenna approach is the use of dielectrics. By coupling the antenna directly to the tissue, a large reflection at the air-skin interface, due to the skin's high dielectric value, is avoided.

The antenna was fabricated and tested in order to determine the accuracy of the simulation at both a low voltage (5 kV) transient and the frequency domain via S11. These were found to agree with the model. To drive the antenna for its intended purpose required the construction of a pulsed power supply over 100 kV. A dual resonance pulse transformer with nanosecond charge times was designed and implemented. When connected to the antenna through a parallel plate transmission line with an integrated spark gap, the complete antenna system was tested in air. An electric field was measured as 600 V/cm, but the use of this antenna in exposing cells or tissues remain to be done.

A separate in vitro study was performed to determine the effects that picosecond pulses could have in the area of electrical stimulation. A 3-D printer system with a non-contact electrode was designed to stimulate neural stem cells. Pulses on the order of 20 – 40 kV/cm were found to have an effect on cellular proliferation, metabolism, and gene expression at sub-cytotoxic levels.

The current antenna system has shown interesting features such as improved coupling to the tissue, increased spatial resolution, and increased delivered field at the target, but the absolute field is still far from the effective value found in the in vitro experiments. Since in vivo experiments may have a different effective value than in vitro studies, a continued in vivo study is necessary to determine the accurate electric field range for certain bioelectric effects. In the meantime, there can be many aspects considered to improve the antenna efficiency and increase the radiated field, so that the gap between the antenna-delivered field and the effective field for inducing bioeffects can be reduced or bridged.

REFERENCES

[1] M. Casciola, S. Xiao, and A. G. Pakhomov, "Damage-free peripheral nerve stimulation by 12-ns pulsed electric field," *Scientific Reports,* vol. 7, no. p. 10453, 2017.

[2] J. A. White, U. Pliquett, P. F. Blackmore, R. P. Joshi, K. H. Schoenbach, and J. F. Kolb, "Plasma membrane charging of jurkat cells by nanosecond pulsed electric fields," *European Biophysics Journal,* vol. 40, no. 8, pp. 947-957, Aug. 2011.

[3] M. R. Prausnitz, V. G. Bose, R. Langer, and J. C. Weaver, "Electroporation of mammalian skin: A mechanism to enhance transdermal drug delivery," *Proceedings of the National Academy of Sciences of the United States of America,* vol. 90, no. 22, pp. 10504-10508, 1993.

[4] S. Guo, D. L. Jackson, N. I. Burcus, Y.-J. Chen, S. Xiao, and R. Heller, "Gene electrotransfer enhanced by nanosecond pulsed electric fields," *Molecular Therapy - Methods & Clinical Development,* vol. 1, no. p. 14043, Jan. 2014.

[5] R. C. G. Martin, "Use of irreversible electroporation in unresectable pancreatic cancer," *Hepatobiliary Surgery and Nutrition,* vol. 4, no. 3, pp. 211-215, 2015.

[6] S. Toepfl, V. Heinz, and D. Knorr, "High intensity pulsed electric fields applied for food preservation," *Chemical Engineering and Processing: Process Intensification,* vol. 46, no. 6, pp. 537-546, Jun. 2007.

[7] K. H. Schoenbach, S. Katsuki, H. Akiyama, T. Heeren, J. F. Kolb, S. Xiao, T. Camp, R. P. Joshi, C. Osgood, R. Nuccitelli, and S. J. Beebe, "Biological effects of intense subnanosecond electrical pulses," in *Conference Record of the 2006 Twenty-Seventh International Power Modulator Symposium*, 2006, pp. 573-576.

[8] K. H. Schoenbach, S. Xiao, R. P. Joshi, J. T. Camp, T. Heeren, J. F. Kolb, and S. J. Beebe, "The effect of intense subnanosecond electrical pulses on biological cells," *IEEE Transactions on Plasma Science,* vol. 36, no. 2, pp. 414-422, Apr. 2008.

[9] Y.-Y. Hua, X.-S. Wang, Y. U. Zhang, C.-G. Yao, X.-M. Zhang, and Z.-A. Xiong, "Intense picosecond pulsed electric fields induce apoptosis through a mitochondrial-mediated pathway in hela cells," *Molecular Medicine Reports,* vol. 5, no. 4, pp. 981-987, Apr. 2012.

[10] Y. Y. Hua, X. S. Wang, Y. U. Zhang, C. G. Yao, X. M. Zhang, and Z. A. Xiong, "Intense picosecond pulsed electric fields induce apoptosis through a mitochondrial-mediated pathway in hela cells," *Molecular Medicine Reports,* vol. 5, no. 4, pp. 981-987, Apr. 2012.

[11] K. H. Schoenbach, S. Xiao, J. T. Camp, M. Migliaccio, S. J. Beebe, and C. E. Baum, "Wideband, high-amplitude, pulsed antennas for medical therapies and medical imaging," in *2009 International Conference on Electromagnetics in Advanced Applications*, 2009, pp. 580-583.

[12] K. H. Schoenbach, R. P. Joshi, S. J. Beebe, and C. E. Baum, "A scaling law for membrane permeabilization with nanopulses," *IEEE Transactions on Dielectrics and Electrical Insulation,* vol. 16, no. 5, pp. 1224-1235, 2009.

[13] J. T. Camp, Y. Jing, J. Zhuang, J. F. Kolb, S. J. Beebe, J. Song, R. P. Joshi, S. Xiao, and K. H. Schoenbach, "Cell death induced by subnanosecond pulsed electric fields at elevated temperatures," *IEEE Transactions on Plasma Science,* vol. 40, no. 10, pp. 2334-2347, 2012.

[14] S. M. Kennedy, E. J. Aiken, K. A. Beres, A. R. Hahn, S. J. Kamin, S. C. Hagness, J. H. Booske, and W. L. Murphy, "Cationic peptide exposure enhances pulsed-electric-field-mediated membrane disruption," *PLOS ONE,* vol. 9, no. 3, p. e92528, 2014.

[15] S. Huang, Y. Zu, and S. Wang, "Gold nanoparticle-enhanced electroporation for leukemia cell transfection," in *Electroporation protocols: Preclinical and clinical gene medicine*, S. Li, J. Cutrera, R. Heller, and J. Teissie, Eds., ed New York, NY: Springer New York, 2014, pp. 69-77.

[16] A. L. Hodgkin and A. F. Huxley, "A quantitative description of membrane current and its application to conduction and excitation in nerve," *The Journal of Physiology,* vol. 117, no. 4, pp. 500-544, 1952.

[17] S. Xiao, A. Pakhomov, F. Guo, S. Polisetty, and K. H. Schoenbach, "Neurostimulation using subnanosecond electric pulses," in *SPIE BiOS: Terahertz and Ultrashort Electromagnetic Pulses for Biomedical Applications*, San Francisco, CA, 2013, p. 6.

[18] I. Semenov, S. Xiao, D. Kang, K. H. Schoenbach, and A. G. Pakhomov, "Cell stimulation and calcium mobilization by picosecond electric pulses," *Bioelectrochemistry,* vol. 105, no. 3, pp. 65-71, Oct. 2015.

[19] S. Xiao, S. Guo, V. Nesin, R. Heller, and K. H. Schoenbach, "Subnanosecond electric pulses cause membrane permeabilization and cell death," *IEEE Transactions on Biomedical Engineering,* vol. 58, no. 5, pp. 1239-1245, 2011.

[20] Y. He, J. Y. Chen, J. R. Knab, W. Zheng, and A. G. Markelz, "Evidence of protein collective motions on the picosecond timescale," *Biophysical Journal,* vol. 100, no. 4, pp. 1058-1065, Feb. 2011.

[21] R. A. Petrella, K. H. Schoenbach, and S. Xiao, "A dielectric rod antenna for picosecond pulse stimulation of neurological tissue," *IEEE Transactions on Plasma Science,* vol. 44, no. 4, pp. 708-714, Apr. 2016.

[22] J. E. Gruber and T. E. James, "Fast-pulse breakdown of nonuniform-field pressurised-air spark gaps," *Electrical Engineers, Proceedings of the Institution of,* vol. 115, no. 10, pp. 1530-1534, 1968.

[23] A. Petrishia and M. Sasikala, "Subnanosecond pulsed intense electromagnetic field radiators for non-invasive cancer treatment," in *2015 International Conference on BioSignal Analysis, Processing and Systems (ICBAPS)*, 2015, pp. 28-32.

[24] C. E. Baum, "Focal waveform of a prolate-spheroidal impulse-radiating antenna," *Radio Science,* vol. 42, no. 6, pp. 1-11, Nov. 2007.

[25] F. Guo, C. Yao, C. Bajracharya, S. Polisetty, K. H. Schoenbach, and S. Xiao, "Simulation study of delivery of subnanosecond pulses to biological tissues with an impulse radiating antenna," *Bioelectromagnetics,* vol. 35, no. 2, pp. 145-159, Feb. 2014.

[26] S. Xiao, F. Guo, J. Li, G. Hou, and K. H. Schoenbach, "Simulation of delivery of subnanosecond electric pulses into biological tissues," in *2012 IEEE International Power Modulator and High Voltage Conference (IPMHVC)*, 2012, pp. 532-535.

[27] G. Varotto and E. Staderini, *On the uwb medical radars working principle* vol. 2, 2011.

[28] L. Xu, S. C. Hagness, M. K. Choi, and D. W. v. d. Weide, "Numerical and experimental investigation of an ultrawideband ridged pyramidal horn antenna with curved launching plane for pulse radiation," *IEEE Antennas and Wireless Propagation Letters,* vol. 2, no. pp. 259-262, 2003.

[29] M. A. Aldhaeebi, M. A. Alzabidi, I. Elshafiey, and A. F. Sheta, "Development of uwb antenna array for hyperthermia treatment," in *2013 IEEE Symposium on Wireless Technology & Applications (ISWTA)*, 2013, pp. 355-358.

[30] M. A. Alzabidi, M. A. Aldhaeebi, and I. Elshafiey, "Development of uwb vivaldi antenna for microwave imaging," in *2013 Saudi International Electronics, Communications and Photonics Conference*, 2013, pp. 1-4.

[31] J. Stang, M. Haynes, P. Carson, and M. Moghaddam, "A preclinical system prototype for focused microwave thermal therapy of the breast," *IEEE Transactions on Biomedical Engineering,* vol. 59, no. 9, pp. 2431-2438, 2012.

[32] G. Varotto and E. M. Staderini, "A 2d simple attenuation model for em waves in human tissues: Comparison with a fdtd 3d simulator for uwb medical radar," in *2008 IEEE International Conference on Ultra-Wideband*, 2008, pp. 1-4.

[33] P. W. Smith, *Transient electronics: Pulsed circuit technology*: Wiley, 2011.

[34] M. Klemm, I. J. Craddock, J. A. Leendertz, A. Preece, D. R. Gibbins, M. Shere, and R. Benjamin, "Clinical trials of a uwb imaging radar for breast cancer," in *Proceedings of the Fourth European Conference on Antennas and Propagation*, 2010, pp. 1-4.

[35] M. Converse, E. J. Bond, B. D. Veen, and C. Hagness, "A computational study of ultra-wideband versus narrowband microwave hyperthermia for breast cancer treatment," *IEEE Transactions on Microwave Theory and Techniques,* vol. 54, no. 5, pp. 2169-2180, 2006.

[36] M. Ketata, M. Dhieb, G. B. Hmida, H. Ghariani, and M. Lahiani, "Uwb pulse propagation in human tissue: Comparison between gaussian and square waves shape," in *2015 16th International Conference on Sciences and Techniques of Automatic Control and Computer Engineering (STA)*, 2015, pp. 158-162.

[37] C. Polk, "Biological applications of large electric fields: Some history and fundamentals," *IEEE Transactions on Plasma Science,* vol. 28, no. 1, pp. 6-14, 2000.

[38] C. Gabriel, S. Gabriel, and E. Corthout, "The dielectric properties of biological tissues: I. Literature survey," *Physics in Medicine & Biology,* vol. 41, no. 11, p. 2231, 1996.

[39] S. Cruciani, V. D. Santis, M. Feliziani, and F. Maradei, "Cole-cole vs debye models for the assessment of electromagnetic fields inside biological tissues produced by wideband emf sources," in *2012 Asia-Pacific Symposium on Electromagnetic Compatibility*, 2012, pp. 685-688.

[40] G. E. Mueller and W. A. Tyrrell, "Polyrod antennas," *The Bell System Technical Journal,* vol. 26, no. 4, pp. 837-851, 1947.

[41] T. Milligan, "Design of polyrod and corrugated-rod antennas," *IEEE Antennas and Propagation Magazine,* vol. 42, no. 1, pp. 88-91, 2000.

[42] M. Sporer, R. Weigel, and A. Koelpin, "A 24 ghz dual-polarized and robust dielectric rod antenna," *IEEE Transactions on Antennas and Propagation,* vol. 65, no. 12, pp. 6952-6959, 2017.

[43] R. V. Satyanarayana and M. V. S. Prasad, "Experimental studies on tapered nylon rod antennas," *International Journal of Electronics and Communication Engineering,* vol. 4, no. 1, pp. 139-143, Feb. 2011.

[44] C. Chi-Chih, R. Kishore Rama, and R. Lee, "A new ultrawide-bandwidth dielectric-rod antenna for ground-penetrating radar applications," *IEEE Transactions on Antennas and Propagation,* vol. 51, no. 3, pp. 371-377, 2003.

[45] J. Y. Chung and C. C. Chen, "Two-layer dielectric rod antenna," *IEEE Transactions on Antennas and Propagation,* vol. 56, no. 6, pp. 1541-1547, 2008.

[46] M. D. Blech, M. M. Leibfritz, and T. F. Eibert, "Ultra-wideband dielectric rod antenna with biconical dipole and reflector," in *2007 IEEE Antennas and Propagation Society International Symposium*, 2007, pp. 2737-2740.

[47] H. T. Hui, Y. A. Ho, and E. K. N. Yung, "A cylindrical dielectric rod antenna fed by a short helix," in *IEEE Antennas and Propagation Society International Symposium. 1996 Digest*, 1996, pp. 1946-1949.

[48] L. Minz, N. Simonov, S. I. Jeon, and J. M. Lee, "Dual layer uwb dielectric probe for bistatic breast cancer detection system," in *2012 International Symposium on Antennas and Propagation (ISAP)*, 2012, pp. 475-478.

[49] S. Hao-Ming, R. W. P. King, and W. Tai Tsun, "V-conical antenna," *IEEE Transactions on Antennas and Propagation,* vol. 36, no. 11, pp. 1519-1525, 1988.

[50] C. A. Balanis, *Advanced engineering electromagnetics*, 2 ed. New York, NY, USA: Wiley, 2012.

[51] C. E. Baum, "Focused aperture antennas," in *Proc. Senson Simulation Notes*, 1987, pp. 40-61.

[52] R. B. Armenta and C. D. Sarris, "Introducing nonuniform grids into the fdtd solution of the transmission-line equations by renormalizing the per-unit-length parameters," *IEEE Transactions on Electromagnetic Compatibility,* vol. 51, no. 3, pp. 818-824, 2009.

[53] R. Schuhmann and T. Weiland, "A stable interpolation technique for fdtd on non-orthogonal grids," *International Journal of Numerical Modelling: Electronic Networks, Devices and Fields,* vol. 11, no. 6, pp. 299-306, 1998.

[54] Z.-D. Deng, S. H. Lisanby, and A. V. Peterchev, "Electric field depth–focality tradeoff in transcranial magnetic stimulation: Simulation comparison of 50 coil designs," *Brain stimulation,* vol. 6, no. 1, pp. 1-13, 2013.

[55] R. A. Petrella, K. H. Schoenbach, and S. Xiao, "A dielectric rod antenna driven by a pulsed power system," *IEEE Transactions on Dielectrics and Electrical Insulation,* vol. 24, no. 4, pp. 2157-2163, 2017.

[56] C. E. Baum, W. L. Baker, W. D. Prather, J. M. Lehr, J. P. O. Loughlin, D. V. Giri, I. D. Smith, R. Altes, J. Fockler, D. M. McLemore, M. D. Abdalla, and M. C. Skipper, "Jolt: A highly directive, very intensive, impulse-like radiator," *Proceedings of the IEEE,* vol. 92, no. 7, pp. 1096-1109, 2004.

[57] J. R. Mayes, W. J. Carey, W. C. Nunnally, and L. Altgilbers, "The marx generator as an ultra wideband source," in *PPPS-2001 Pulsed Power Plasma Science 2001. 28th IEEE International Conference on Plasma Science and 13th IEEE International Pulsed Power Conference. Digest of Papers (Cat. No.01CH37251)*, 2001, pp. 1665-1668 vol.2.

[58] Z. Roberts, Z. Shotts, R. Miller, M. Zorn, F. Rose, and S. Best, "Design and testing of a vector inversion generator operating as a rf oscillator," in *2007 IEEE 34th International Conference on Plasma Science (ICOPS)*, 2007, pp. 424-424.

[59] G. J. Rohwein, "A three megavolt transformer for pfl pulse charging," *IEEE Transactions on Nuclear Science,* vol. 26, no. 3, pp. 4211-4213, 1979.

[60] R. A. Petrella, S. Xiao, and S. Katsuki, "An air core pulse transformer with a linearly integrated primary capacitor bank to achieve ultrafast charging," *IEEE Transactions on Dielectrics and Electrical Insulation,* vol. 23, no. 4, pp. 2443-2449, 2016.

[61] J. L. Korioth, R. P. Copeland, and D. W. Scholfield, "A novel super low inductance primary ring utilized in a pulsed dual resonant tuned transformer," in *Digest of Technical Papers. 12th IEEE International Pulsed Power Conference. (Cat. No.99CH36358)*, 1999, pp. 811-814 vol.2.

[62] S. Lim, C. Chuhyun, R. Hong-Je, K. Jong-Soo, R. Geun-Hie, and J. Yun-Sik, *Fabrication and operation testing of a dual resonance pulse transformer for pfl pulse charging* vol. 59, 2011.

[63] P. Smith, "Pulse transformers," in *Transient electronics: Pulsed circuit technology*. vol. 1, ed West Suxxes, England: Wiley, 2002, pp. 159-161.

[64] Z. Shotts, F. Rose, S. Merryman, and R. Kirby, "Design methodology for dual resonance pulse transformers," in *2005 IEEE Pulsed Power Conference*, 2005, pp. 1117-1120.

[65] R. Lundin, "A handbook formula for the inductance of a single-layer circular coil," *Proceedings of the IEEE,* vol. 73, no. 9, pp. 1428-1429, 1985.

[66] J. L. Reed, "Greater voltage gain for tesla‐transformer accelerators," *Review of Scientific Instruments,* vol. 59, no. 10, pp. 2300-2301, Oct. 1988.

[67] A. G. Pakhomov, I. Semenov, S. Xiao, O. N. Pakhomova, B. Gregory, K. H. Schoenbach, J. C. Ullery, H. T. Beier, S. R. Rajulapati, and B. L. Ibey, "Cancellation of cellular responses to nanoelectroporation by reversing the stimulus polarity," *Cellular and molecular life sciences : CMLS,* vol. 71, no. 22, pp. 4431-4441, 2014.

[68] X. Duan, E. Kang, C. Y. Liu, G.-l. Ming, and H. Song, "Development of neural stem cell in the adult brain," *Current opinion in neurobiology,* vol. 18, no. 1, pp. 108-115, 2008.

[69] S. Xiao, I. Semenov, R. Petrella, A. G. Pakhomov, and K. H. Schoenbach, "A subnanosecond electric pulse exposure system for biological cells," *Medical & biological engineering & computing,* vol. 55, no. 7, pp. 1063-1072, Jul. 2017.

[70] J. A. Reid, P. A. Mollica, G. D. Johnson, R. C. Ogle, R. D. Bruno, and P. C. Sachs, "Accessible bioprinting: Adaptation of a low-cost 3d-printer for precise cell placement and stem cell differentiation," *Biofabrication,* vol. 8, no. 2, p. 025017, Jun. 2016.

[71] M. Zhao, P. C. Sachs, X. Wang, C. I. Dumur, M. O. Idowu, V. Robila, M. P. Francis, J. Ware, M. Beckman, A. Rizki, S. E. Holt, and L. W. Elmore, "Mesenchymal stem cells in mammary adipose tissue stimulate progression of breast cancer resembling the basal-type," *Cancer biology & therapy,* vol. 13, no. 9, pp. 782-92, Jul. 2012.

[72] P. C. Sachs, M. P. Francis, M. Zhao, J. Brumelle, R. R. Rao, L. W. Elmore, and S. E. Holt, "Defining essential stem cell characteristics in adipose-derived stromal cells extracted from distinct anatomical sites," *Cell and tissue research,* vol. 349, no. 2, pp. 505-15, Aug. 2012.

[73] J. P. Brown, S. Couillard-Despres, C. M. Cooper-Kuhn, J. Winkler, L. Aigner, and H. G. Kuhn, "Transient expression of doublecortin during adult neurogenesis," *The Journal of comparative neurology,* vol. 467, no. 1, pp. 1-10, Dec. 2003.

[74] M. C. Raff, R. Mirsky, K. L. Fields, R. P. Lisak, S. H. Dorfman, D. H. Silberberg, N. A. Gregson, S. Leibowitz, and M. C. Kennedy, "Galactocerebroside is a specific cell-surface antigenic marker for oligodendrocytes in culture," *Nature,* vol. 274, no. p. 813, Aug. 1978.

[75] O. Steward, E. R. Torre, R. Tomasulo, and E. Lothman, "Neuronal activity up-regulates astroglial gene expression," *Proceedings of the National Academy of Sciences of the United States of America,* vol. 88, no. 15, pp. 6819-6823, 1991.

[76] S. Xiao, S. Q. Guo, V. Nesin, R. Heller, and K. H. Schoenbach, "Subnanosecond electric pulses cause membrane permeabilization and cell death," *Ieee T Bio-Med Eng,* vol. 58, no. 5, pp. 1239-1245, May 2011.

[77] H.-F. Chang, Y.-S. Lee, T. K. Tang, and J.-Y. Cheng, "Pulsed dc electric field–induced differentiation of cortical neural precursor cells," *PloS one,* vol. 11, no. 6, p. e0158133, 2016.

[78] Y. Lu, M. He, Y. Zhang, S. Xu, L. Zhang, Y. He, C. Chen, C. Liu, H. Pi, Z. Yu, and Z. Zhou, "Differential pro-inflammatory responses of astrocytes and microglia involve stat3 activation in response to 1800 mhz radiofrequency fields," *PloS one,* vol. 9, no. 10, p. e108318, 2014.

[79] J. L. Stringer, "Repeated seizures increase gfap and vimentin in the hippocampus," *Brain research,* vol. 717, no. 1, pp. 147-153, Apr. 1996.

[80] P. Chan, L. F. Eng, Y. L. Lee, and V. W. H. Lin, "Effects of pulsed magnetic stimulation on gfap levels in cultured astrocytes," *Journal of neuroscience research,* vol. 55, no. 2, pp. 238-244, Jan. 1999.

[81] M. Fujiki and O. Steward, "High frequency transcranial magnetic stimulation mimics the effects of ecs in upregulating astroglial gene expression in the murine cns," *Molecular Brain Research,* vol. 44, no. 2, pp. 301-308, Mar. 1997.

[82] Z. Xu, T. Xue, Z. Zhang, X. Wang, P. Xu, J. Zhang, X. Lei, Y. Li, Y. Xie, L. Wang, M. Fang, and Y. Chen, "Role of signal transducer and activator of transcription-3 in up-regulation of gfap after epilepsy," *Neurochemical research,* vol. 36, no. 12, p. 2208, Aug. 2011.

[83] X. Yang, G. He, Y. Hao, C. Chen, M. Li, Y. Wang, G. Zhang, and Z. Yu, "The role of the jak2-stat3 pathway in pro-inflammatory responses of emf-stimulated n9 microglial cells," *Journal of Neuroinflammation,* vol. 7, no. pp. 54-54, Sep. 2010.

[84] S. Murase and R. D. McKay, "Neuronal activity-dependent stat3 localization to nucleus is dependent on tyr-705 and ser-727 phosphorylation in rat hippocampal neurons," *European Journal of Neuroscience,* vol. 39, no. 4, pp. 557-565, Feb 2014.

[85] I. Semenov, S. Xiao, D. Kang, K. H. Schoenbach, and A. G. Pakhomov, "Cell stimulation and calcium mobilization by picosecond electric pulses," *Bioelectrochemistry,* vol. 105, no. pp. 65-71, Oct 2015.

[86] F. Appaix, M. F. Nissou, B. van der Sanden, M. Dreyfus, F. Berger, J. P. Issartel, and D. Wion, "Brain mesenchymal stem cells: The other stem cells of the brain?," *World J Stem Cells,* vol. 6, no. 2, pp. 134-43, Apr 26 2014.

[87] K. Sellheyer and D. Krahl, "Skin mesenchymal stem cells: Prospects for clinical dermatology," *J Am Acad Dermatol,* vol. 63, no. 5, pp. 859-65, Nov 2010.

[88] C. Petrie, S. Tholpady, R. Ogle, and E. Botchwey, "Proliferative capacity and osteogenic potential of novel dura mater stem cells on poly-lactic-co-glycolic acid," *Journal of biomedical materials research. Part A,* vol. 85, no. 1, pp. 61-71, Apr 2008.

[89] R. Feng, S. Zhou, Y. Liu, D. Song, Z. Luan, X. Dai, Y. Li, N. Tang, J. Wen, and L. Li, "Sox2 protects neural stem cells from apoptosis via up-regulating survivin expression," *Biochemical Journal,* vol. 450, no. 3, pp. 459-468, Mar. 2013.

[90] S. Xiao, I. Semenov, R. Petrella, A. G. Pakhomov, and K. H. Schoenbach, "A subnanosecond electric pulse exposure system for biological cells," *Medical & Biological Engineering & Computing,* vol. 55, no. 7, pp. 1063-1072, Jul. 2017.

[91] J. W. Duncan and V. P. Minerva, "100:1 bandwidth balun transformer," *Proceedings of the IRE,* vol. 48, no. 2, pp. 156-164, 1960.

[92] J. de los Santos, D. Garcia, and J. A. Eiras, "Dielectric characterization of materials at microwave frequency range," *Materials Research,* vol. 6, no. pp. 97-101, 2003.

[93] A. Baumketner, "Electric field as a disaggregating agent for amyloid fibrils," *The Journal of Physical Chemistry B,* vol. 118, no. 50, pp. 14578-14589, Dec. 2014.

[94] A. Teggatz, A. Jostingmeier, T. Meyer, and A. S. Omar, "Detection of buried objects such as landmines using a forward impulse radiating antenna (ira)," in *2005 IEEE Antennas and Propagation Society International Symposium*, 2005, pp. 627-630 vol. 2A.

APPENDICES

APPENDIX A: DESCRIPTION OF EVANESCENT WAVES

According to the boundary conditions in Maxwell's equations, there must be a conservation of the D field across a dielectric boundary ($E_1\varepsilon_1 = E_2\varepsilon_2$). However, in the case of total internal reflection, the incident wave does not propagate into the second dielectric (ε_2). However, a non-propagating wave must be present. This phenomenon gives rise to evanescent waves. The key features of the evanescent wave are that 1) it does not propagate, and 2) its magnitude decays exponentially as a function of distance from the boundary. Understanding of the evanescent wave can be gained from considering a plane wave in a frequency domain incident on a dielectric boundary shown below:

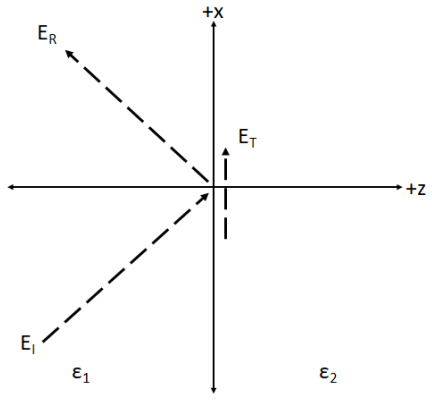

From the general transmittance equation: $\overrightarrow{E_T} = \overrightarrow{E_{0T}}\, e^{j(k\sin\theta_T)x} e^{j(k\cos\theta_T)x} e^{-j\omega t}$ [50]
For total internal reflection, the critical angle is defined by $\sin(\theta_T) > 1$. This means that $\cos(\theta_T)$ must be imaginary. This allows us to rewrite the equation $k\cos(\theta_T) = jB$.

$$\overrightarrow{E_T} = \left(\overrightarrow{E_{0T}}\, e^{j(k\sin\theta_T)x} e^{-j\omega t}\right) e^{-Bz}$$

The resulting equation describes the evanescent wave. The amplitude only in the x direction and is decaying exponentially in with z. For the dielectric of $\varepsilon_r = 7.3$, the critical angle is given by: $\theta_T = \sin^{-1}\sqrt{\frac{1}{\varepsilon_r}} = 21.7°$.

APPENDIX B: MSC VIABILITY RESULTS

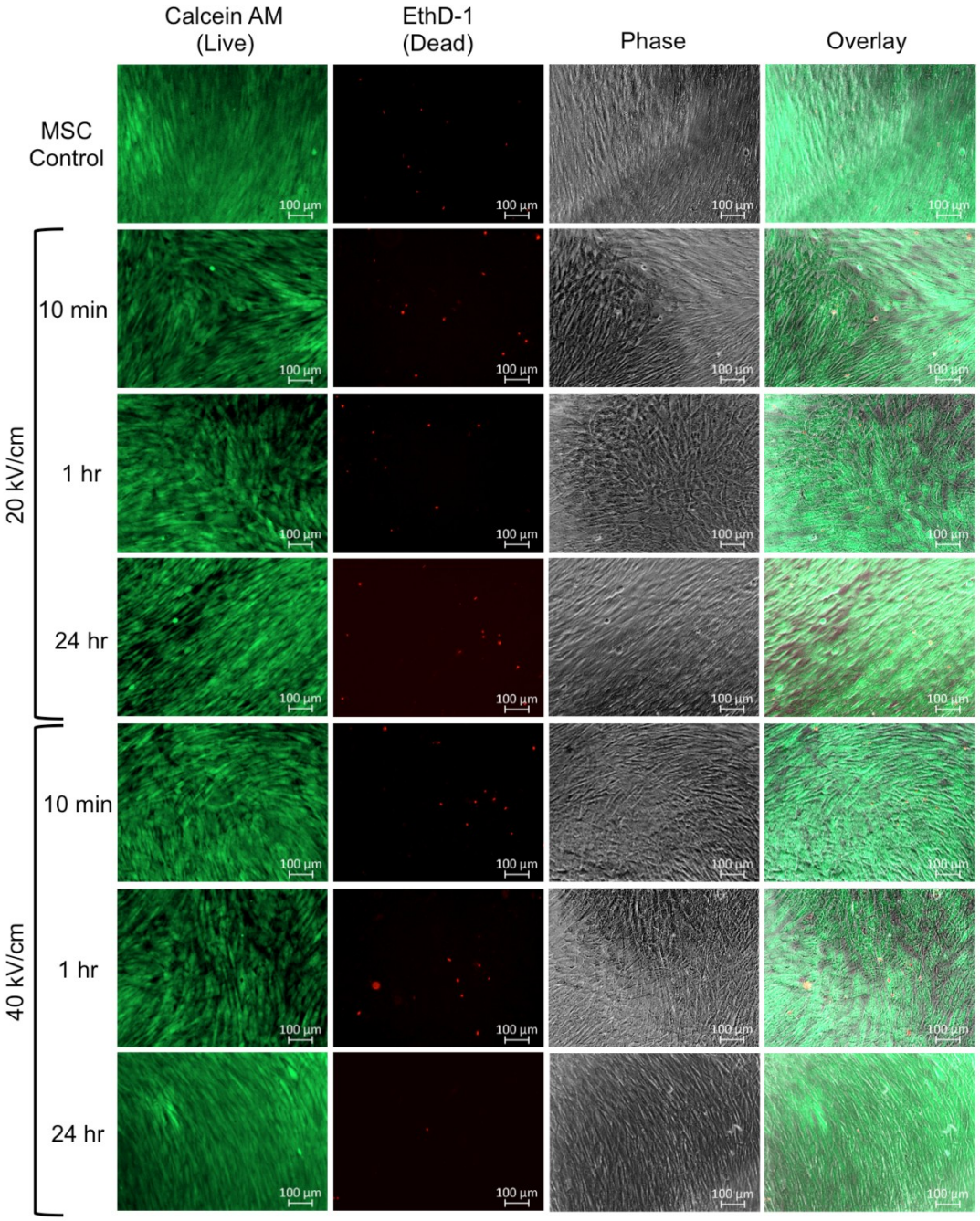

psPEF of 20 kV and 40 kV/cm do not induce cell death in mesenchymal stem cells. MSCs exposed to 20 kV/cm and 40 kV/cm were treated with calcein AM (green;live) and EthD-1 (red;dead). Relative to the control (non-pulsed) bASC3, no significant increase in cell death was detected at 10 min, 1 hr, or 24 hr post-pulse treatment in either pulsing parameter. All images were acquired with a 10x objective.

APPENDIX C: MSC PROLIFERATION RESULTS

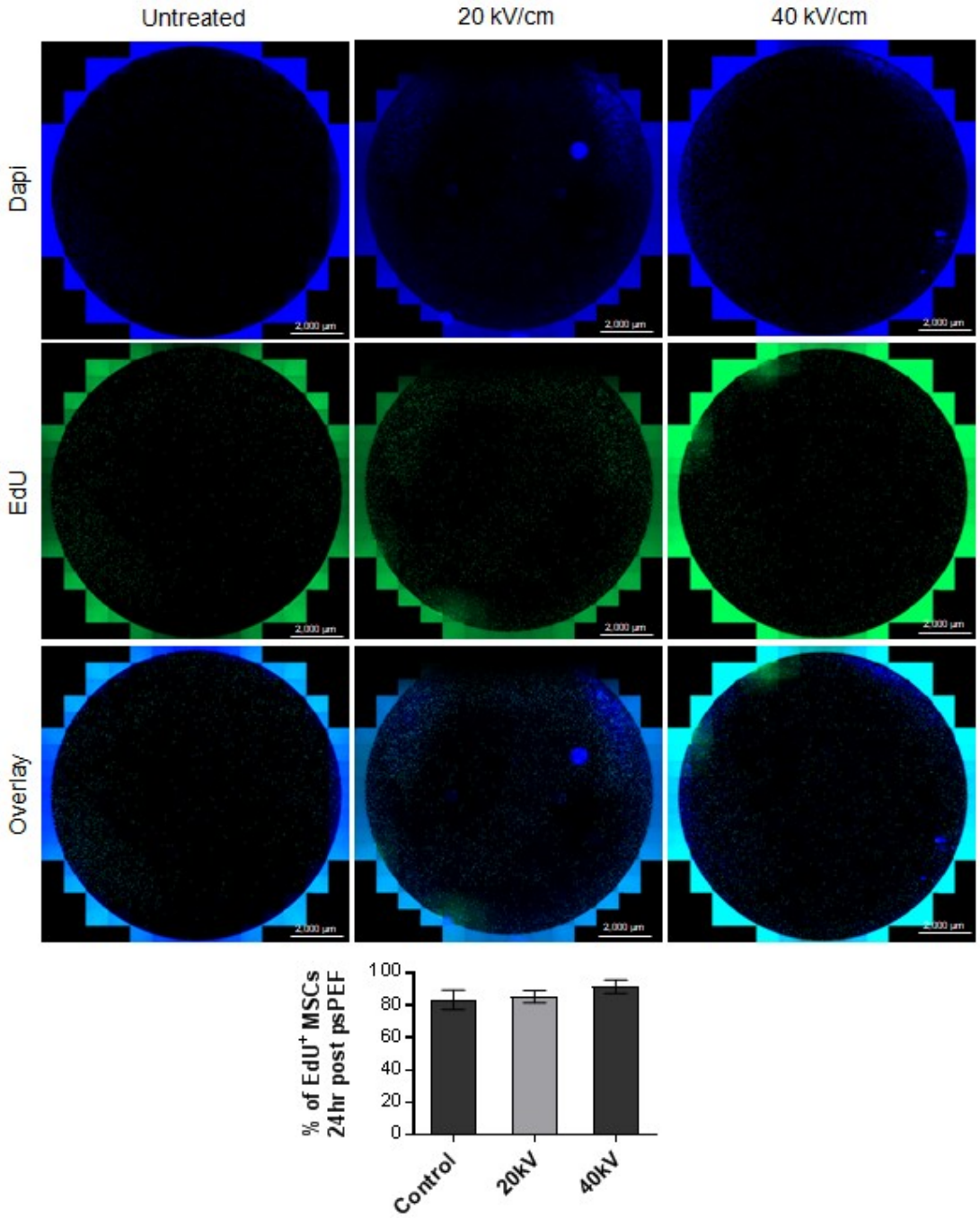

Picosecond pulses do not inhibit proliferation in MSCs. (a) Representative images of the entire well of MSCs immediately following psPEF exposure, and supplement/fixation with 10 µM EdU. Cell nuclei were counterstained with DAPI. (b) MSCs exposed to 20 kV (center column) and 40 kV (right column) showed EdU incorporation percentage of 71.5% and 76.7 %, respectively. Untreated control (left column) showed EdU incorporation percentage of 83.6%. Tiled images of the entire well were acquired with a 10x objective.

VITA

Ross Aaron Petrella

EDUCATION

Old Dominion University (ODU) Norfolk, Virginia 2014 - 2018
Ph.D. Biomedical Engineering

Virginia Commonwealth University (VCU) Richmond, Virginia 2010 - 2014
B.S Biomedical Engineering
Minors in Electrical Engineering and Mathematical Science

WORK EXPERIENCE

- Graduate Research Assistant: Frank Reidy Center for Bioelectrics, 4211 Monarch Way Norfolk, VA 23508
- Deutscher Akademischer Austauschdienst (DAAD) Intern: Institut für Bioprozess und Analysenmesstechnik, Rosenhof 1, 37308 Heilbad Heiligenstadt, Germany
- Undergraduate Research Assistant: School of Engineering 401 West Main Street PO Box 843067, Richmond, VA 23284-3067 (804) 828-9491

PUBLICATIONS

- R. A. Petrella, P. A. Mollica, M. Zamponi, J. A. Reid, S. Xiao, R. D. Bruno, P. C. Sachs, "3D Bioprinter Applied Picosecond Pulsed Electric Fields for Targeted Manipulation of Proliferation and Lineage Specific Gene Expression in Neural Stem Cells," *Journal of Neural Engineering* (submitted)
- R. A. Petrella, K. H. Schoenbach, and S. Xiao, "A Dielectric Rod Antenna Driven by a Pulsed Power System," *IEEE Transactions on Dielectrics and Electrical Insulation*, vol. 24, no. 4, pp. 2157-2163, Sep. 2017.
- S. Xiao, R. Petrella, and H. Akiyama "Delivery of Electric Pulses to Biological Tissues Using Antennas" *Bioelectrics*, Tokyo, Japan: Springer Japan, 2017, ch.2, sec. 6, pp. 41-107.
- R. A. Petrella, S. Katsuki, S. Xiao, "An Air Core Pulse Transformer with a Linearly Integrated Primary Capacitor Bank to Achieve Ultrafast Charging," *IEEE Transactions on Dielectrics and Electrical Insulation,* vol. 23, no. 4, pp. 2443 – 2449. Aug. 2016.
- S. Xiao, I. Semenov, R. Petrella, A. G. Pakhomov, K. H. Schoenbach, "A Subnanosecond Electric Pulse Exposure System for Biological Cells," *Medical & Biological Engineering & Computation*, pp.1-10, May 2016.
- R. A. Petrella, K. H. Schoenbach and S. Xiao, "A Dielectric Rod Antenna for Picosecond Pulse Stimulation of Neurological Tissue," *IEEE Transactions on Plasma Science*, vol. 44, no. 4, pp. 708-714, Apr. 2016.

Peer Reviewed Conference Papers

- R. A. Petrella and S. Xiao, "Characterization of a Dielectric Rod Antenna Used for Radiating Picosecond Pulses," *2016 IEEE International Power Modulator and High Voltage Conference (IPMHVC),* San Francisco, CA, 2016, pp. 426-429.
- R. A. Petrella and S. Xiao, "Simulation of a conical antenna for stimulating neurological tissue," *Applied Computational Electromagnetics (ACES), 2015 31st International Review of Progress in*, Williamsburg, VA, 2015, pp. 1-2.